NTNU

Norwegian University of
Science and Technology

Real-time Simulation of Offshore Light Lift Operations

Gjermund Tomasgard

Master of Science in Engineering Cybernetics
Submission date: December 2008
Supervisor: Tor Arne Johansen, ITK

Norwegian University of Science and Technology
Department of Engineering Cybernetics

Problem Description

The subject to be studied is the modeling of a crane simulator which can be interconnected with a separate vessel simulator with mutual communication of relevant states and data.

The assignment consists of the following parts:
- Develop, improve and join existing simulator modules into a crane simulator for a heave compensated knuckle boom crane, including winch/drive with control system, booms, and forces on the payload such as hydrodynamics.
- Prepare the crane simulator for interconnection with an existing vessel simulator.
- Simulation of scenarios from typical operations.
- Evaluation of simulator performance and accuracy.

Assignment given: 28. July 2008
Supervisor: Tor Arne Johansen, ITK

Preface

I would like to thank my supervisor Professor Tor Arne Johansen for general guidance during the work with the thesis. Also, his valuable feedback on the written material during the finishing stage is highly acknowledged.

I have had the privilege to work on my thesis at the office of Marine Cybernetics in Trondheim, and I would like to thank all my forthcoming colleagues there for a social and inspiring working environment.

In particular, I would like to express my gratitude to Jørgen Sverdrup-Thygeson, Jan-Egil Wagnild, Tom Arne Pedersen, Olve Mo, Roger Skjetne, and Olav Egeland. In my everyday work with the thesis they have always showed genuine interest in my questions and thoughts, and taken their time to guide me on the right way. Having their extensive experience in modelling and simulation, and use of the Matlab/Simulink environment to lean on, has been important for my achievements in this thesis, and for keeping up the progress of the work. Tom Arne and Roger are also acknowledged for their valuable feedback on the report content.

Gjermund Tomasgard
Trondheim, December 18, 2008

Abstract

Crane operations are an integral part of offshore operations. Simulators are a useful tool in conjunction with crane operations, and may be used for training of personnel, planning of operations, validation of mechanical designs, verification of crane control system integrity, etc. Simulators contain physical/mathematical models of the crane and its working environment. Models for the various parts of the crane exist in academic literature, but a complete crane simulator does not seem to have been documented. The focus of this thesis has been to extend and improve the existing models, and join them into a real-time simulator for a heave compensated knuckle boom crane. The simulator has also been prepared for interconnection to a vessel simulator.

The crane simulator is validated qualitatively by simulations; the various modules have been validated separately, and, successively, the modules have been jointly validated, and finally, the complete simulator is validated.

The simulator and its modules exhibited good performance during the validation.

Contents

Chapter 1

Introduction

1.1 Motivation

It is hard to imagine offshore operations without the use of cranes. They are involved in all kinds of operations ranging from simple manoeuvres like moving equipment from one place on the vessel deck to another, to large lifting operations comprising two crane rigs lifting in tandem.

Depending on the size of the lifted object and the vessel or vessels supporting the operation, crane operations may be divided into two categories; light lifts and heavy lifts. According to [20], heavy lifts comprise payloads weighing more than 1-2 % of the vessel displacement and typically more than 1000 t. Normally, heave compensation is not possible on heavy lifts. Also, the dynamics of the vessel and payload are mutually coupled.

Light lifts, on the other hand, comprise payloads less than 1-2 % of the vessel displacement and less than a few hundred tonnes. Then the vessel dynamics may be considered to be unaffected by the presence of the crane and payload, and heave compensation is possible.

This thesis focuses on light lifts. As mentioned, these lifting operations may be performed by the aid of heave compensation, which is a system that attenuate the wave induced vessel motion transferred to the payload via the hoisting cable; see [20] and [27]. By the use of heave compensation, operations can be carried out at more severe weather conditions than otherwise possible.

Typical tasks performed by heave compensated cranes are installation of subsea structures, maintenance, and dive support. Typical payloads are bathyspheres, ROVs, subsea equipment to be installed on the seabed such as wellheads, Christmas trees and other process equipment, [15].

Simulators are an important tool in order to enhance the safety and reduce the costs of crane operations. For example, simulators may be used for validation

of the mechanical design, planning and verification of operations, training of personnel, and testing of the control system integrity by Hardware-In-The-Loop simulation, [15]. Depending on the application, different requirements may be put on the simulators. For example, a simulator made to aid the mechanical design process, requires accurate computations of forces and loads on the equipment. There may be no specific requirement for the simulation speed, and just a few worst case scenarios may be sufficient to validate the designs.

For simulators tailored for training of personnel, on the other hand, a realistic user interface by the means of 3D visualisation and simulator controls is an obvious requirement. Also, the simulator must run in real-time in order to provide realistic user interaction. The computation of forces and loads on objects need not be accurate to a level beyond what is required to ensure a realistic user experience and user interaction.

HIL-testing simulators also require real-time simulation, but put less requirements on the user interface. On the other hand, these simulators require detailed simulation of all signals required by the control system subject to testing, and simulation of relevant adverse scenarios which the control system might be exposed to. HIL-testing is a qualitative validation of the control system integrity; As long as the signals provided to the control system by the simulator are consistent, the level of accuracy for the computation of forces etc. is only required to a level that ensures good HIL-testing.

This thesis presents a crane simulator for a heave compensated knuckle boom crane. The simulator shall be able to run in real-time, but it is not further specified which purpose the simulator is made for.

1.2 Litterature review

Presently, several companies supply simulators to the offshore industry. Most simulators are made for the purpose of personnel training. Some examples are the Ship Manoeuvring Simulator Centre [8], Offshore Simulator Centre [6], First Interactive [1], Kongsberg SIM [4], MPRI Ship Analytics [5] and GlobalSim [2]. Only two of these companies, the Ship Manoeuvring Simulator Centre and the MPRI Ship Analytics, provide marine crane simulators, and of these the Ship Manoeuvring Simulator Centre includes a knuckle boom crane simulator.

In the academic area some work has been conducted on this field, but, to the author's knowledge, a complete crane simulator has not yet been developed. In [30] a generic dynamic model for the crane structure with an arbitrary number of revolute and prismatic joints is derived using standard techniques from modelling theory of robotic structures. A valve controlled hydraulic cylinder model for luffing the crane booms is also provided. In [31] hydraulic winch systems for offshore cranes are studied and models provided with emphasis on real-time

simulation properties. In [27] a combined active/passive hydraulic heave compensation system based on the flying sheave principle is modelled, and in [28] a model of the payload and hoisting cable is derived, comprising scenarios such as water entry/exit, slack rope and landing the load onto a surface. Bumpless transitions between the various phases of the lifting operation are also included.

Other relevant work is [16], [25] and [3]. [16] presents models for slender mechanical systems, such as cables, for real-time applications; [25] presents a comparison of different control strategies for the control of loads through the wave zone; and [3] is a research programme which has tested alternative control strategies for lifting payloads through the wave zone.

1.3 Contribution

The contribution of this thesis is the interconnection, extension and improvement of existing simulator modules into a fully working knuckle boom crane simulator with heave compensation. Each module is provided with procedures for initialisation, and the model is prepared for interconnection with a vessel simulator providing the vessel motion.

The simulator is validated by qualitative verification of simulations. Each module is tested separately, and successively, the modules have been tested jointly, including the complete crane simulator. Finally, a vessel model is included in the simulator model in order to verify the interface between the crane and vessel simulators.

The validation shows that the simulator performs quite well. A flaw was discovered in the crane dynamics model for an extreme test case, but the flaw does not seem to influence the simulations when the crane dynamics model is run in more realistic scenarios. Also, the PI speed winch drive controller should be enhanced to a position controller in order to avoid payload creep during heave compensation in irregular waves.

A defined test case which spanned 60 s, took 30.15 s to simulate with 10 ms step size, and 27.54 s with 20 ms step size on a desktop computer with 2 GHz processor and 1 GB RAM running Windows XP with Service Pack 3. The test could not be simulated with a step size of 30 ms. The Bogacki-Shampine integration method was used in the simulations.

1.4 Objective

The objective of this thesis is to build a generic simulator for a heave compensated knuckle boom crane for real-time simulations. The simulator shall be made up by the following modules:

- a rigid body dynamics model of the crane structure

- hydraulics model for the boom luffing motions
- a model of the payload and hoisting cable with forces acting on the cable and load
- a winch and drive system model including heave compensation and constant tension functionality

The simulator and its modules shall be validated qualitatively by simulating realistic scenarios.

1.5 Outline

The various simulator modules are presented chapter wise. In **Chapter 2** the crane model is presented with a hydraulics model for luffing the booms presented in **Chapter 3**. Next, the model of the payload and hoisting cable is presented in **Chapter 4**, and finally, the winch and drive system model is presented in **Chapter 5**. Winch control strategies are presented in **Chapter 6**. Evaluation and discussion of the properties of the modules, and the performance of the connected systems is found in **Chapter 7**, and the final conclusions are given in **Chapter 8**.

Chapter 2

Crane model

2.1 Introduction

In this chapter a dynamic model for a knuckle boom crane structure is derived. An illustration of a typical knuckle boom crane is found in Figure 2.1. Such cranes consist of three rotational links; the rotary king, which is mounted onto the vessel deck or a pedestal; the knuckle boom, which is connected to the king; and the knuckle jib, which is the outermost boom link.

The crane model is derived by the Denavit-Hartenberg convention and the recursive Newton-Euler scheme; see [23]. This methodology assumes that the crane is influenced by the enforced motion of the crane base, torques in each joint, and the end-effector (i.e. the crane boom tip) force and torque. Also, the masses and inertia tensors for each link are assumed to be constant.

The mass of objects on top of the king, such as the operator cabin and winch, are assumed to be included in the king mass, and the inertia tensors of the links are assumed to be constant with reference to the centre of mass for the respective link.

The motion of the crane base is given by the vessel motion due to waves, and it is assumed that the motion input to the crane model is represented in the crane base frame. The crane base is assumed to be rigidly mounted onto the vessel, and a vessel simulator provides the linear and rotational motion of the origin of the vessel body frame with respect to an inertial frame.

The model derivation is to a great extent based on the general theory presented in [23], and on a similar crane model derivation presented in [30]. Theory from [10] is also used.

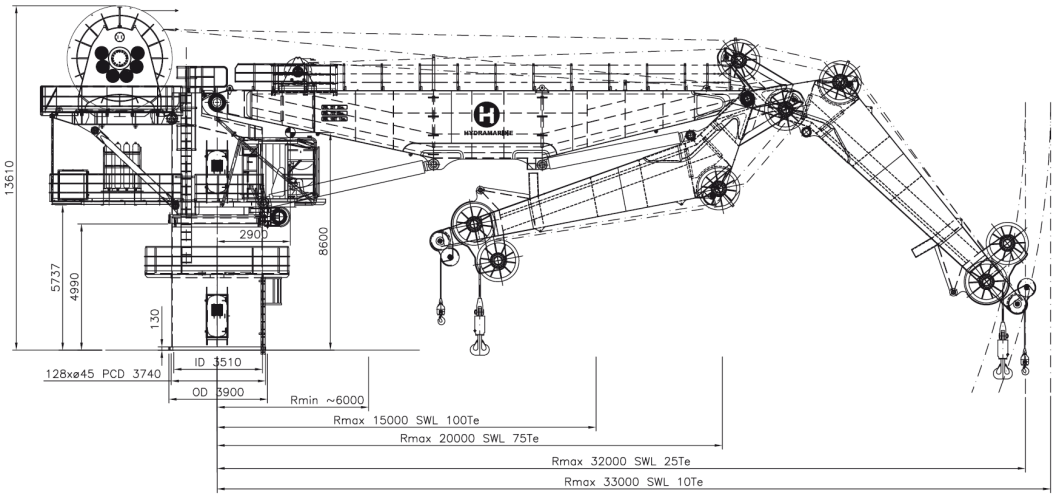

Figure 2.1: Typical knuckle boom crane. Illustration from [24].

Link	a_i	α_i	d_i	θ_i
1	0	$\frac{\pi}{2}$	d_1	q_1
2	a_2	0	0	q_2
3	a_3	0	0	q_3

Table 2.1: The Denavit-Hartenberg parameters for the knuckle boom crane.

2.2 Kinematics

The crane kinematics are derived by the Denavit-Hartenberg (DH) convention, which is a standard methodology to compute the kinematics for an open-chain manipulator. An introduction to the DH convention and manipulator kinematics may be found in [23]. For a knuckle boom crane, which consists of three revolute joints, the DH convention results in the parameters given in Table 2.1. Figure 2.2 relates the DH parameters to the crane structure.

In the figure four axes systems/frames are shown, and, with O_i denoting the origin of Frame i the DH parameters relates to the frames as follows:

- a_i distance from O_i to the intersection of the x_i and z_{i-1} axes along the x_i axis.
- d_i distance from O_{i-1} to the intersection of the x_i and z_{i-1} axes.
- α_i angle between z_{i-1} and z_i about x_i.
- θ_i angle between x_{i-1} and x_i about z_{i-1}.

From the illustration, we see that d_1 denotes the king height, a_2 the knuckle boom length, and a_3 the knuckle jib length.

Following the DH convention does not lead to a unique set of parameters; hence, other equivalent parametrisations exist.

From the DH table transformation matrices are constructed which relate Frame i to Frame $i-1$, see [23]. The transformation matrices consist of a rota-

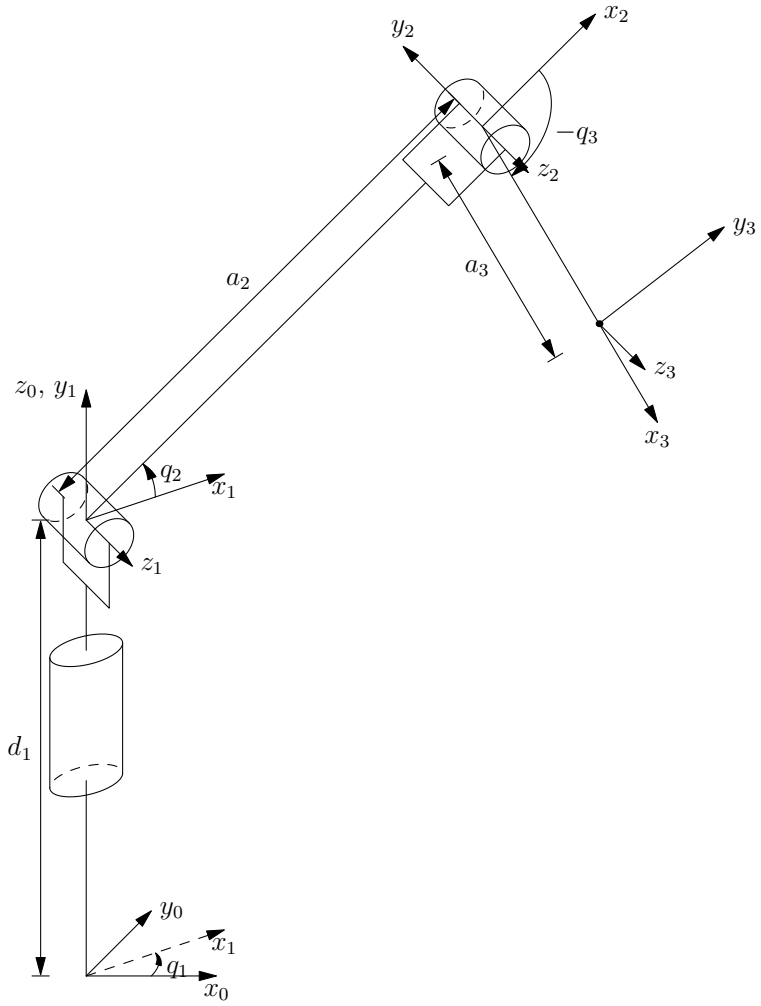

Figure 2.2: Definition of the Denavit-Hartenberg parameters.

tion matrix $\mathbf{R}_i^{i-1} \in \mathbb{R}^{3\times3}$, which denotes the orientation of Frame i in Frame $i-1$, and a position vector $\mathbf{p}_i^{i-1} \in \mathbb{R}^3$, which denotes the position of the origin of Frame i in Frame $i-1$. The generic transformation matrix from Frame i to Frame $i-1$ is

$$\mathbf{A}_i^{i-1} = \begin{bmatrix} \mathbf{R}_i^{i-1} & \mathbf{p}_i^{i-1} \\ \mathbf{0}^T & 1 \end{bmatrix} = \begin{bmatrix} c\theta_i & -s\theta_i c\alpha_i & s\theta_i s\alpha_i & a_i c\theta_i \\ s\theta_i & c\theta_i c\alpha_i & -c\theta_i s\alpha_i & a_i s\theta_i \\ 0 & s\alpha_i & c\alpha_i & d_i \\ 0 & 0 & 0 & 1 \end{bmatrix} \tag{2.1}$$

Here, and in all transformation matrices in this thesis, $c\cdot$ denotes $\cos(\cdot)$, and $s\cdot$ denotes $\sin(\cdot)$. From the DH table and the generic transformation matrix, the

link specific transformation matrices are obtained as follows:

$$\mathbf{A}_3^2 = \begin{bmatrix} \mathbf{R}_3^2 & \mathbf{p}_3^2 \\ \mathbf{0}^T & 1 \end{bmatrix} = \begin{bmatrix} cq_3 & -sq_3 & 0 & a_3cq_3 \\ sq_3 & cq_3 & 0 & a_3sq_3 \\ 0 & 0 & 1 & 0 \\ 0 & 0 & 0 & 1 \end{bmatrix} \tag{2.2}$$

$$\mathbf{A}_2^1 = \begin{bmatrix} \mathbf{R}_2^1 & \mathbf{p}_2^1 \\ \mathbf{0}^T & 1 \end{bmatrix} = \begin{bmatrix} cq_2 & -sq_2 & 0 & a_2cq_2 \\ sq_2 & cq_2 & 0 & a_2sq_2 \\ 0 & 0 & 1 & 0 \\ 0 & 0 & 0 & 1 \end{bmatrix} \tag{2.3}$$

$$\mathbf{A}_1^0 = \begin{bmatrix} \mathbf{R}_1^0 & \mathbf{p}_1^0 \\ \mathbf{0}^T & 1 \end{bmatrix} = \begin{bmatrix} cq_1 & 0 & sq_1 & 0 \\ sq_1 & 0 & -cq_1 & 0 \\ 0 & 1 & 0 & d_1 \\ 0 & 0 & 0 & 1 \end{bmatrix} \tag{2.4}$$

The transformation from the end effector frame/boom tip frame to the base frame is given by

$$\mathbf{T}_n^0(\mathbf{q}) = \mathbf{A}_1^0(\mathbf{q})\mathbf{A}_2^1(\mathbf{q})\mathbf{A}_3^2(\mathbf{q}), \tag{2.5}$$

where $\mathbf{q} = [q_1 \quad q_2 \quad q_3]^T$. The resulting form of the transformation matrix is

$$\mathbf{T}_n^0 = \begin{bmatrix} \mathbf{R}_3^0 & \mathbf{p}_3^0 \\ \mathbf{0}^T & 1 \end{bmatrix}, \tag{2.6}$$

where $\mathbf{R}_3^0$ is the orientation of Frame 3 given in Frame 0 and $\mathbf{p}_3^0$ is the position vector of the origin of Frame 3 given in Frame 0.

2.3 Differential kinematics

Differential kinematics relates the joint velocities to the corresponding end effector/boom tip linear and angular velocities. This mapping is obtained by the use of the geometric Jacobian $\mathbf{J}(\mathbf{q})$. See e.g. [23] for details. The mapping is given by

$$\mathbf{v} = \begin{bmatrix} \dot{\mathbf{p}} \\ \boldsymbol{\omega} \end{bmatrix} = \mathbf{J}(\mathbf{q})\dot{\mathbf{q}}, \tag{2.7}$$

where $\dot{\mathbf{p}}$ is the boom tip linear velocity relative to the crane base, and $\boldsymbol{\omega}$ is the angular velocity. The geometric Jacobian consists of two submatrices

$$\mathbf{J} = \begin{bmatrix} \mathbf{J}_P \\ \mathbf{J}_O \end{bmatrix}, \tag{2.8}$$

and $\mathbf{J}_P$ and $\mathbf{J}_O$ relate the joint velocities to the linear and angular velocities, respectively. Generally, the geometric Jacobian has dimension $\mathbf{J} \in \mathbb{R}^{6\times n}$. For

the three link knuckle boom crane structure, $n = 3$, and hence, $\mathbf{J}_P, \mathbf{J}_O \in \mathbb{R}^{3\times 3}$. These submatrices may in turn be divided into 3×1 vectors according to

$$\begin{bmatrix}\mathbf{J}_P \\ \mathbf{J}_O\end{bmatrix} = \begin{bmatrix}\jmath_{P1} & \jmath_{P2} & \jmath_{P3} \\ \jmath_{O1} & \jmath_{O2} & \jmath_{O3}\end{bmatrix} \tag{2.9}$$

The expressions for the vectors depend on whether the corresponding joint is prismatic or revolute. Since all the crane joints are revolute, they are expressed as

$$\begin{bmatrix}\jmath_{Pi} \\ \jmath_{Oi}\end{bmatrix} = \begin{bmatrix}\mathbf{z}_{i-1} \times (\mathbf{p} - \mathbf{p}_{i-1}) \\ \mathbf{z}_{i-1}\end{bmatrix}, \tag{2.10}$$

in accordance with [23]. The vectors in Equation (2.10) are defined as follows:

- $\mathbf{p}$ is the first three elements of the fourth column in the transformation matrix $\mathbf{T}_n^0$
- $\mathbf{p}_{i-1}$ is the first three elements of the fourth column in the matrix $\mathbf{T}_{i-1}^0$
- $\mathbf{z}_{i-1}$ is the third column in the rotation matrix $\mathbf{R}_{i-1}^0$

Obviously, for $i = 1$ the transformation and rotation matrices are

$$\mathbf{T}_0^0 = \begin{bmatrix}1 & 0 & 0 & 0 \\ 0 & 1 & 0 & 0 \\ 0 & 0 & 1 & 0 \\ 0 & 0 & 0 & 1\end{bmatrix} \tag{2.11}$$

and

$$\tag{2.12}$$

$$\mathbf{R}_0^0 = \begin{bmatrix}1 & 0 & 0 \\ 0 & 1 & 0 \\ 0 & 0 & 1\end{bmatrix} \tag{2.13}$$

From the definitions above, the vectors are expressed as

$$\mathbf{p} = \begin{bmatrix}cq_1(a_3(cq_2cq_3 - sq_2sq_3) + a_2cq_2) \\ sq_1(a_3(cq_2cq_3 - sq_2sq_3) + a_2cq_2) \\ a_3(sq_2cq_3 + cq_2sq_3) + a_2sq_2 + d_1\end{bmatrix} \tag{2.14}$$

$$\mathbf{p}_0 = \begin{bmatrix}0 \\ 0 \\ 0\end{bmatrix}, \mathbf{p}_1 = \begin{bmatrix}0 \\ 0 \\ d_1\end{bmatrix}, \mathbf{p}_2 = \begin{bmatrix}a_2cq_1cq_2 \\ a_2sq_1cq_2 \\ a_2sq_2 + d_1\end{bmatrix} \tag{2.15}$$

$$\mathbf{z}_0 = \begin{bmatrix}0 \\ 0 \\ 1\end{bmatrix}, \mathbf{z}_1 = \begin{bmatrix}sq_1 \\ -cq_1 \\ 0\end{bmatrix}, \mathbf{z}_2 = \begin{bmatrix}sq_1 \\ -cq_1 \\ 0\end{bmatrix} \tag{2.16}$$

The geometric Jacobian may now be expressed by the vectors in (2.14) – (2.16) as

$$\mathbf{J} = \begin{bmatrix} \mathbf{z}_0 \times (\mathbf{p} - \mathbf{p}_0) & \mathbf{z}_1 \times (\mathbf{p} - \mathbf{p}_1) & \mathbf{z}_2 \times (\mathbf{p} - \mathbf{p}_2) \\ \mathbf{z}_0 & \mathbf{z}_1 & \mathbf{z}_2 \end{bmatrix} \tag{2.17}$$

When the crane model is connected to the payload and cable model, and/or the winch model, the acceleration of the boom tip must be provided, see Section 4.7. Differentiating Equation (2.7) gives the expression

$$\dot{\mathbf{v}} = \begin{bmatrix} \ddot{\mathbf{p}} \\ \dot{\boldsymbol{\omega}} \end{bmatrix} = \dot{\mathbf{J}}(\mathbf{q}, \dot{\mathbf{q}})\dot{\mathbf{q}} + \mathbf{J}(\mathbf{q})\ddot{\mathbf{q}} \tag{2.18}$$

for the acceleration of the boom tip relative to the base frame, where

$$\begin{bmatrix} \jmath\dot{P}i \\ \jmath\dot{O}i \end{bmatrix} = \begin{bmatrix} \dot{\mathbf{z}}_{i-1} \times (\mathbf{p} - \mathbf{p}_{i-1}) + \mathbf{z}_{i-1} \times (\dot{\mathbf{p}} - \dot{\mathbf{p}}_{i-1}) \\ \dot{\mathbf{z}}_{i-1} \end{bmatrix}, \tag{2.19}$$

and

$$\dot{\mathbf{J}}(\mathbf{q}, \dot{\mathbf{q}}) = \begin{bmatrix} \jmath\dot{P}1 & \jmath\dot{P}2 & \jmath\dot{P}3 \\ \jmath\dot{O}1 & \jmath\dot{O}2 & \jmath\dot{O}3 \end{bmatrix} \tag{2.20}$$

2.4 Dynamics

The joint space dynamic model for a manipulator derived from the Lagrange formulation of the system may be stated as

$$\mathbf{B}(\mathbf{q})\ddot{\mathbf{q}} + \mathbf{C}(\mathbf{q}, \dot{\mathbf{q}})\dot{\mathbf{q}} + \mathbf{F}_v\dot{\mathbf{q}} + \mathbf{F}_s\mathbf{sgn}(\dot{\mathbf{q}}) + \mathbf{g}(\mathbf{q}) = \boldsymbol{\tau} - \mathbf{J}^T(\mathbf{q})\mathbf{h}, \tag{2.21}$$

see e.g. [23]. The first term on the left hand side represents the acceleration terms, the second term contains the Coriolis and centripetal forces, the third and fourth terms represent viscous and Coulomb joint friction, respectively, and the last term represents the geometrically dependent forces, which in this context are due to the presence of gravity. The first term on the right hand side is the generalized forces $\tau = [\tau_1 \quad \tau_2 \quad \tau_3]^T$ acting in the respective joints. Hydraulic cylinder models for generating the torques τ_2 and τ_3 are provided in Chapter 3. The second term includes the end effector force and moment $\mathbf{h} = [\mathbf{f} \quad \boldsymbol{\mu}]^T \in \mathbb{R}^6$ through the geometric Jacobian $\mathbf{J}(\mathbf{q})$ defined in Section 2.3. According to [23], $\mathbf{h}$ *"denotes the vector of force and moment exerted by the end effector on the environment"*. This force will be equal in magnitude but with opposite direction to the force exerted on the boom tip by the hoisting cable. Also, the cable will not exert any moment on the boom tip; hence, the end effector force may be expressed as

$$\mathbf{h} = [\mathbf{f}_{boom} \quad \mathbf{0}]^T, \tag{2.22}$$

where $\mathbf{f}_{boom}$ denotes the force applied by the crane boom tip on the cable. An expression for the force is derived in Section 4.7.

2.4.1 Solving the direct dynamics

Solving the direct dynamics implies solving the initial value problem for the system, i.e. given the initial states $\mathbf{q}(t_0)$, $\dot{\mathbf{q}}(t_0)$, determine $\ddot{\mathbf{q}}(t)$, $\dot{\mathbf{q}}(t)$ and $\mathbf{q}(t)$ resulting from the joint torques $\boldsymbol{\tau}(t)$ and boom tip forces $\mathbf{h}(t)$ for $t > t_0$. By reformulating Equation (2.21) to

$$\ddot{\mathbf{q}} = \mathbf{B}^{-1}(\mathbf{q})(\boldsymbol{\tau} - \boldsymbol{\tau}') \tag{2.23}$$

where

$$\boldsymbol{\tau}'(\mathbf{q}, \dot{\mathbf{q}}) = \mathbf{C}(\mathbf{q}, \dot{\mathbf{q}})\dot{\mathbf{q}} + \mathbf{F}_v\dot{\mathbf{q}} + \mathbf{F}_s\mathbf{sgn}(\dot{\mathbf{q}}) + \mathbf{g}(\mathbf{q}) + \mathbf{J}^T(\mathbf{q})\mathbf{h}, \tag{2.24}$$

the joint accelerations may by found directly, and the velocities and angles by integration of the acceleration. However, according to [23], a computationally more efficient method is to solve Equation (2.23) by the recursive Newton-Euler (RNE) scheme.

Mathematically, the scheme may be represented by the function

$$\boldsymbol{\tau} = RNE(\mathbf{q}, \dot{\mathbf{q}}, \ddot{\mathbf{q}}, \boldsymbol{\omega}_0^0, \boldsymbol{\alpha}_0^0, \ddot{\mathbf{p}}_0^0 - \mathbf{g}^0, \mathbf{h}^0), \tag{2.25}$$

with the input parameters joint angles, velocities and accelerations, and angular velocity $\boldsymbol{\omega}_0^0$ and acceleration $\boldsymbol{\alpha}_0^0$, and the linear acceleration $\ddot{\mathbf{p}}_0^0$ of the base frame, acceleration of gravity $\mathbf{g}^0$ and end effector force $\mathbf{h}^0$, all given in Frame 0.

In principle, the RNE scheme solves the inverse dynamics problem, i.e. given the inputs, it computes the joint torques $\boldsymbol{\tau}$ of Equation (2.21) required to yield the motion $\mathbf{q}$, $\dot{\mathbf{q}}$ and $\ddot{\mathbf{q}}$.

However, when using the RNE scheme to solve the direct dynamics problem, it is used to find the inertia matrix $\mathbf{B}(\mathbf{q})$ and the joint position and velocity dependent torque contributions $\boldsymbol{\tau}'$ by altering the inputs as follows:

$$\boldsymbol{\tau}' = RNE(\mathbf{q}, \dot{\mathbf{q}}, \mathbf{0}, \boldsymbol{\omega}_0^0, \boldsymbol{\alpha}_0^0, \ddot{\mathbf{p}}_0^0 - \mathbf{g}^0, \mathbf{h}^0) \tag{2.26}$$

$$\mathbf{b}_i = RNE(\mathbf{q}, \mathbf{0}, \mathbf{e}_i, \boldsymbol{\omega}_0^0, \boldsymbol{\alpha}_0^0, \ddot{\mathbf{p}}_0^0, \mathbf{h}^0),\ i \in \{1, 2, 3\} \tag{2.27}$$

where

$$\mathbf{e}_1 = [1 \quad 0 \quad 0]^T,\ \mathbf{e}_2 = [0 \quad 1 \quad 0]^T,\ \mathbf{e}_3 = [0 \quad 0 \quad 1]^T \tag{2.28}$$

and

$$\mathbf{B}(\mathbf{q}) = [\mathbf{b}_1 \quad \mathbf{b}_2 \quad \mathbf{b}_3], \tag{2.29}$$

see [23]. Now the joint acceleration vector is found by substituting Equation (2.26) and Equation (2.27) via (2.29) into Equation (2.23).

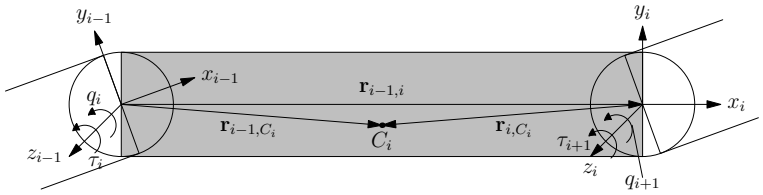

Figure 2.3: Definition of the RNE vectors. The illustration is reproduced from [10].

2.4.2 The RNE scheme

The RNE scheme is made up by a forward recursion and a backwards recursion. During the forward recursion, link velocities and accelerations are computed recursively for each link. Given the joint velocities and accelerations, and the velocities and accelerations of the base frame, $\boldsymbol{\omega}_0^0$, $\boldsymbol{\alpha}_0^0$ and $\ddot{\mathbf{p}}_0^0 - \mathbf{g}^0$, this is carried out as follows:
For $i = 1...3$:

$$\boldsymbol{\omega}_i^i = \mathbf{R}_i^{i-1^T}\left(\boldsymbol{\omega}_{i-1}^{i-1} + \dot{q}_i \mathbf{z}_0\right) \tag{2.30}$$

$$\dot{\boldsymbol{\omega}}_i^i = \mathbf{R}_i^{i-1^T}\left(\dot{\boldsymbol{\omega}}_{i-1}^{i-1} + \ddot{q}_i \mathbf{z}_0 + \dot{q}_i \boldsymbol{\omega}_{i-1}^{i-1} \times \mathbf{z}_0\right) \tag{2.31}$$

$$\ddot{\mathbf{p}}_i^i = \mathbf{R}_i^{i-1^T}\ddot{\mathbf{p}}_{i-1}^{i-1} + \dot{\boldsymbol{\omega}}_i^i \times \mathbf{r}_{i-1,i}^i + \boldsymbol{\omega}_i^i \times \left(\boldsymbol{\omega}_i^i \times \mathbf{r}_{i-1,i}^i\right) \tag{2.32}$$

$$\ddot{\mathbf{p}}_{C_i}^i = \ddot{\mathbf{p}}_i^i + \dot{\boldsymbol{\omega}}_i^i \times \mathbf{r}_{i,C_i}^i + \boldsymbol{\omega}_i^i \times \left(\boldsymbol{\omega}_i^i \times \mathbf{r}_{i,C_i}^i\right) \tag{2.33}$$

Equation (2.30) represents the angular velocity of Frame i, Equation (2.31) the angular acceleration, and Equation (2.32) the linear acceleration. Equation (2.33) yields the acceleration of the centre of mass of Link i.

Once the velocities and accelerations are determined, the forces and moments are computed in a backwards recursion for each link, starting with the outermost link and propagating inwards ($i = 3...1$):

$$\mathbf{f}_i^i = \mathbf{R}_{i+1}^i \mathbf{f}_{i+1}^{i+1} + m_i \ddot{\mathbf{p}}_{C_i}^i \tag{2.34}$$

$$\begin{aligned}\boldsymbol{\mu}_i^i = &-\mathbf{f}_i^i \times (\mathbf{r}_{i-1,i}^i + \mathbf{r}_{i,C_i}^i) + \mathbf{R}_{i+1}^i \boldsymbol{\mu}_{i+1}^{i+1} + \mathbf{R}_{i+1}^i \mathbf{f}_{i+1}^{i+1} \times \mathbf{r}_{i,C_i}^i \\ &+ \bar{\mathbf{I}}_i^i \dot{\boldsymbol{\omega}}_i^i + \boldsymbol{\omega}_i^i \times \left(\bar{\mathbf{I}}_i^i \boldsymbol{\omega}_i^i\right),\end{aligned} \tag{2.35}$$

where $\mathbf{f}_i^i$ is the force exerted by Link $i-i$ on Link i and $\boldsymbol{\mu}_i^i$ is the moment exerted by Link $i-1$ on link i with respect to origin of Frame $i-1$.

Finally, the joint torques are found by

$$\tau_i = \boldsymbol{\mu}_i^{i^T} \mathbf{R}_i^{i-1^T} \mathbf{z}_0 + F_{vi}\dot{q}_i + F_{si} sgn(\dot{q}_i) \tag{2.36}$$

In order to utilise the RNE scheme, the following parameters must be defined for each link:

m_i mass of Link i,
$\bar{\mathbf{I}}_i^i$ inertia tensor of Link i given in Frame i,
$\mathbf{r}_{i-1,C_i}$ vector from origin of Frame $(i-1)$ to the centre of mass C_i of Link i,
$\mathbf{r}_{i,C_i}$ vector from origin of Frame i to the centre of mass C_i of Link i,
$\mathbf{r}_{i-1,i}$ vector from origin of Frame $(i-1)$ to the origin of Frame i,
F_{vi} viscous friction coefficient for Joint i,
F_{si} Coulomb friction coefficient for Joint i,
$\mathbf{R}_i^{i-1}$ rotation matrix from Frame i to Frame $i-1$,
$\mathbf{z}_0$ axis of rotation in current frame, $\mathbf{z}_0 = [0 \quad 0 \quad 1]^T$.

The vectors $\mathbf{r}_{i-1,C_i}$, $\mathbf{r}_{i,C_i}$ and $\mathbf{r}_{i-1,i}$ are illustrated in Figure 2.3. A similar figure is also found in [10]. The Frames $i-1$ and i in the figure illustrate Denavit-Hartenberg frames for Links $i-1$ and i, respectively. The inertia tensor of Link i is assumed to be constant when given in Frame i. All rotation matrices are defined in Section 2.2 except $\mathbf{R}_4^3$, which represents the rotation from the frame in which the boom tip force $\mathbf{f}_4^4$ is given to the boom tip frame.

From Equation (2.25) it is seen that the end effector force is assumed to be provided given in the crane base frame. In this regard, it is seen by the transformation

$$\mathbf{R}_4^3\mathbf{f}_4^4 = \mathbf{R}_0^3\mathbf{R}_4^0\mathbf{f}_4^4 = \mathbf{R}_0^3\mathbf{f}_4^0 \tag{2.37}$$

that $\mathbf{R}_4^3$ must be replaced by $\mathbf{R}_0^3$. The rotation matrix $\mathbf{R}_4^0$ will be derived in Section 2.5.2. The rationale for making this partition, is that all model inputs (except the joint torques $\boldsymbol{\tau}$) and outputs will be represented in the crane base frame, which provides a convenient interface to the other modules of the model. To sum up, the crane model may be denoted as the function

$$(\mathbf{p}_{boom}^0, \dot{\mathbf{p}}_{boom}^0, \ddot{\mathbf{p}}_{boom}^0) = CRANE(\boldsymbol{\omega}_0^0, \boldsymbol{\alpha}_0^0, \ddot{\mathbf{p}}_0^0 - \mathbf{g}^0, \mathbf{h}^0, \boldsymbol{\tau}) \tag{2.38}$$

which outputs the linear position, velocity and acceleration of the boom tip decomposed in the crane base frame. The position is given by $\mathbf{p}_3^0$ in Equation (2.6), the velocity by (2.7) and acceleration by (2.18).

As implicitly stated by Equation (2.22), the second term in Equation (2.35) will be zero for $i = 3$.

2.5 Interfacing the crane model

During a crane operation the vessel will be kept at a near fixed position by a dynamic positioning system. When this is the case, *"an Earth-fixed tangent plane on the [earth] surface is used for navigation. This is usually referred to as flat Earth navigation, and it will for simplicity be denoted as the n-frame."*; see [12]. The n-frame is also called the North-East-Down frame, and for flat Earth navigation it is considered to be inertial, i.e. that Newton's laws apply, see [12]. A review of reference frames may also be found in [12].

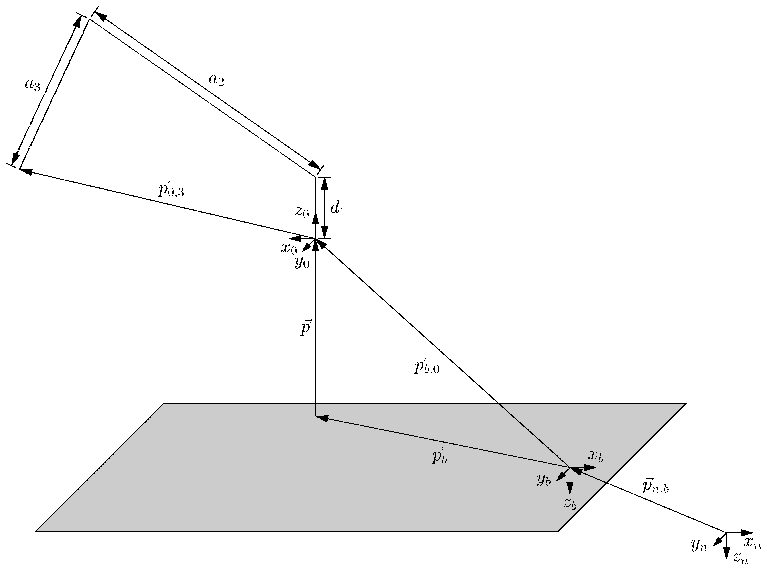

Figure 2.4: Definition of reference frames.

The n-frame has an x-axis pointing towards true North, a y-axis pointing towards East, and a z-axis pointing downwards normal to the Earth's surface. The origin of the n-frame is assumed to be positioned at the mean-free water surface.

Figure 2.4 gives an overview of the reference frames required to provide the vessel motion to the crane model. The already described n-frame is denoted with subscript n. The vessel body frame denoted with subscript b, is fixed in the vessel body and is assumed to be positioned midships in both the longitudinal and lateral direction, and in the mean free-water surface. The x-axis points in the longitudinal direction from aft to fore, the y-axis towards the starboard side, and the z-axis is normal to the x- and y-axes and pointing downwards.

The crane base frame denoted with subscript 0 is placed in the crane structure's first joint at a fixed position $\vec{p}_{b,0}$ relative to the b-frame. Often, the crane is mounted onto a pedestal with height $|\vec{p}_{p,0}|$ placed at $\vec{p}_{b,p}$ relative to the b-frame, i.e. $\vec{p}_{b,0} = \vec{p}_{b,p} + \vec{p}_{p,0}$. The x_0-axis points in the longitudinal direction from fore to aft, the y_0-axis toward the starboard side, and the z_0-axis is normal to the x_0- and y_0-axis pointing upwards.

The constant rotation matrices between the b and 0-frames may be found by inspection of Figure 2.4 and noting that the respective x, y and z-axes are parallel and that the x and z-axes have opposite directions. Hence, the rotation matrices are given by

$$\mathbf{R}_b^0 = \mathbf{R}_0^b = \begin{bmatrix} -1 & 0 & 0 \\ 0 & 1 & 0 \\ 0 & 0 & -1 \end{bmatrix} \tag{2.39}$$

In order to provide the vessel motion to the crane model, and the boom tip motion to the hoisting cable and payload model, the following vectors must be provided from the vessel:

- $\boldsymbol{\Theta}$ Euler angles
- $\boldsymbol{\omega}_{nb}^{b}$ angular velocity of frame b with respect to frame n decomposed in frame b,
- $\dot{\boldsymbol{\omega}}_{nb}^{b}$ angular acceleration of frame b with respect to frame n decomposed in frame b,
- $\mathbf{p}^{n}$ vessel position decomposed in the n-frame,
- $\mathbf{v}_{0}^{b}$ body-fixed linear velocity,
- $\dot{\mathbf{v}}_{0}^{b}$ body-fixed linear acceleration.

The vector notation is taken from [12].

The Euler angles

$$\boldsymbol{\Theta} = \begin{bmatrix} \phi \\ \theta \\ \psi \end{bmatrix} \tag{2.40}$$

denote the orientation of the b-frame relative to the n-frame, where ϕ, θ and ψ denote the roll, pitch and yaw angles, respectively.

The elements of the body-fixed angular velocity vector

$$\boldsymbol{\omega}_{nb}^{b} = \begin{bmatrix} p \\ q \\ r \end{bmatrix} \tag{2.41}$$

denote the roll, pitch and yaw angle velocities, respectively, and the roll, pitch and yaw accelerations are given by

$$\dot{\boldsymbol{\omega}}_{nb}^{b} = \begin{bmatrix} \dot{p} \\ \dot{q} \\ \dot{r} \end{bmatrix} \tag{2.42}$$

The position of the vessel relative to the n-frame, is given in the n-frame by

$$\mathbf{p}^{n} = \begin{bmatrix} n \\ e \\ d \end{bmatrix}, \tag{2.43}$$

and the vessel velocity and acceleration is given in the b-frame by

$$\mathbf{v}_{0}^{b} = \begin{bmatrix} u \\ v \\ w \end{bmatrix} \tag{2.44}$$

and

$$\dot{\mathbf{v}}_{0}^{b} = \begin{bmatrix} \dot{u} \\ \dot{v} \\ \dot{w} \end{bmatrix}, \tag{2.45}$$

respectively. For a thorough review of the above listed quantities, refer to [12].

The rotation matrix from the b-frame to the n-frame is stated in [12] as

$$\mathbf{R}_b^n(\mathbf{\Theta}) = \begin{bmatrix} c\psi c\theta & -s\psi c\phi + c\psi s\theta s\phi & s\psi s\phi + c\psi c\phi s\theta \\ s\psi c\theta & c\psi c\phi + s\phi s\theta s\psi & -c\psi s\phi + s\theta s\psi c\phi \\ -s\theta & c\theta s\phi & c\theta c\phi \end{bmatrix} \tag{2.46}$$

Since rotation matrices possess the property

$$\mathbf{R}\mathbf{R}^T = \mathbf{I} \quad \Rightarrow \quad \mathbf{R}^T = \mathbf{R}^{-1}, \tag{2.47}$$

the rotation matrix $\mathbf{R}_n^b$ is given by

$$\mathbf{R}_n^b(\mathbf{\Theta}) = \mathbf{R}_b^n(\mathbf{\Theta})^T \tag{2.48}$$

The time derivative of $\mathbf{R}_b^n(\mathbf{\Theta})$ is given by

$$\dot{\mathbf{R}}_n^b(\mathbf{\Theta}) = \mathbf{R}_n^b(\mathbf{\Theta})\mathbf{S}(\boldsymbol{\omega}_{nb}^b), \tag{2.49}$$

where $\mathbf{S}(\boldsymbol{\omega}_{nb}^b)$ is the skew-symmetric matrix

$$\mathbf{S}(\boldsymbol{\omega}_{nb}^b) = \begin{bmatrix} 0 & -r & q \\ r & 0 & -p \\ -q & p & 0 \end{bmatrix}, \tag{2.50}$$

see [12].

The time derivative of $\mathbf{S}(\boldsymbol{\omega}_{nb}^b)$ is

$$\dot{\mathbf{S}}(\boldsymbol{\omega}_{nb}^b) = \mathbf{S}(\dot{\boldsymbol{\omega}}_{nb}^b) = \begin{bmatrix} 0 & -\dot{r} & \dot{q} \\ \dot{r} & 0 & -\dot{p} \\ -\dot{q} & \dot{p} & 0 \end{bmatrix} \tag{2.51}$$

$$\dot{\mathbf{p}}^n = \mathbf{R}_b^n(\mathbf{\Theta})\mathbf{v}_o^b \tag{2.52}$$

2.5.1 Including the vessel motion

The crane model requires ω_0^0, α_0^0, $\mathbf{a}_0^0$ as inputs. These are assumed to be supplied from a vessel model and represented in the crane base frame. The rotation of the vectors is as follows:

$$\boldsymbol{\omega}_0^0 = \mathbf{R}_b^0\boldsymbol{\omega}_{nb}^b \tag{2.53}$$
$$\dot{\boldsymbol{\omega}}_0^0 = \mathbf{R}_b^0\dot{\boldsymbol{\omega}}_{nb}^b \tag{2.54}$$
$$\ddot{\mathbf{p}}_0^0 = \mathbf{R}_b^0\dot{\mathbf{v}}_o^b \tag{2.55}$$
$$\mathbf{g}_0 = \mathbf{R}_b^0\mathbf{R}_n^b(\mathbf{\Theta})\mathbf{g}^n \tag{2.56}$$

The acceleration of gravity vector decomposed in the n-frame is given by

$$\mathbf{g}^n = \begin{bmatrix} 0 & 0 & 9.81 \end{bmatrix}^T \ \mathrm{m/s^2} \tag{2.57}$$

2.5.2 Including the boom tip force

Given the boom tip force from Equation (2.22) represented in the n-frame, $\mathbf{f}^n_{boom}$, the force represented in the crane base frame is given by

$$\mathbf{h}^0 = \mathbf{R}^0_n \mathbf{f}^n_{boom} = \mathbf{R}^0_b \mathbf{R}^b_n(\boldsymbol{\Theta}) \mathbf{f}^n_{boom} \tag{2.58}$$

The matrix $\mathbf{R}^0_4$ in Equation (2.37) may no be expressed as

$$\mathbf{R}^0_4 = \mathbf{R}^0_b \mathbf{R}^b_n(\boldsymbol{\Theta}) \tag{2.59}$$

2.5.3 Transforming the boom tip motion to the n-frame

The payload and hoisting cable model in Chapter 4 will be derived assuming an inertial frame. Hence, this model requires the boom tip motion given in the inertial frame. As stated in Section 2.5, the n-frame is assumed to be inertial, and the coordinate transformation of the boom tip motion from the crane base frame to the n-frame is thus provided here.

With reference to Figure 2.4, the boom tip position relative to the n-frame is given in coordinate free form as

$$\vec{p}_{n,3} = \vec{p}_{n,b} + \vec{p}_{b,0} + \vec{p}_{0,3} \tag{2.60}$$

Expressed by coordinate vectors, the boom tip position represented in the n-frame is given by

$$\mathbf{p}^n_3 = \mathbf{p}^n + \mathbf{R}^n_b(\boldsymbol{\Theta}) \mathbf{p}^b_{b,0} + \mathbf{R}^n_b(\boldsymbol{\Theta}) \mathbf{R}^b_0 \mathbf{p}^0_3 \tag{2.61}$$

$$\mathbf{p}^n_3 = \mathbf{p}^n + \mathbf{R}^n_b(\boldsymbol{\Theta}) \left(\mathbf{p}^b_{b,0} + \mathbf{R}^b_0 \mathbf{p}^0_3 \right) \tag{2.62}$$

The boom tip velocity represented in the n-frame is given by differentiating Equation (2.61)

$$\dot{\mathbf{p}}^n_3 = \dot{\mathbf{p}}^n + \dot{\mathbf{R}}^n_b(\boldsymbol{\Theta}) \left(\mathbf{p}^b_{b,0} + \mathbf{R}^b_0 \mathbf{p}^0_3 \right) + \mathbf{R}^n_b(\boldsymbol{\Theta}) \left(\dot{\mathbf{p}}^b_{b,0} + \mathbf{R}^b_0 \dot{\mathbf{p}}^0_3 \right) \tag{2.63}$$

$$\dot{\mathbf{p}}^n_3 = \mathbf{R}^n_b(\boldsymbol{\Theta}) \mathbf{v}^b_o + \mathbf{R}^n_b(\boldsymbol{\Theta}) \mathbf{S}(\boldsymbol{\omega}^n_{nb}) \left(\mathbf{p}^b_{b,0} + \mathbf{R}^b_0 \mathbf{p}^0_3 \right) + \mathbf{R}^n_b(\boldsymbol{\Theta}) \mathbf{R}^b_0 \dot{\mathbf{p}}^0_3 \tag{2.64}$$

$$\dot{\mathbf{p}}^n_3 = \mathbf{R}^n_b(\boldsymbol{\Theta}) \left(\mathbf{v}^b_o + \mathbf{S}(\boldsymbol{\omega}^n_{nb}) \left(\mathbf{p}^b_{b,0} + \mathbf{R}^b_0 \mathbf{p}^0_3 \right) + \mathbf{R}^b_0 \dot{\mathbf{p}}^0_3 \right) \tag{2.65}$$

Finally, the boom tip acceleration represented in the n-frame is given by

$$\begin{aligned} \ddot{\mathbf{p}}^n_3 = {} & \dot{\mathbf{R}}^n_b(\boldsymbol{\Theta}) \left(\mathbf{v}^b_o + \mathbf{S}(\boldsymbol{\omega}^n_{nb}) \left(\mathbf{p}^b_{b,0} + \mathbf{R}^b_0 \mathbf{p}^0_3 \right) + \mathbf{R}^b_0 \dot{\mathbf{p}}^0_3 \right) \\ & + \mathbf{R}^n_b(\boldsymbol{\Theta}) \left(\dot{\mathbf{v}}^b_o + \mathbf{S}(\dot{\boldsymbol{\omega}}^n_{nb}) \left(\mathbf{p}^b_{b,0} + \mathbf{R}^b_0 \mathbf{p}^0_3 \right) + \mathbf{S}(\boldsymbol{\omega}^n_{nb}) \left(\dot{\mathbf{p}}^b_{b,0} + \mathbf{R}^b_0 \dot{\mathbf{p}}^0_3 \right) + \mathbf{R}^b_0 \ddot{\mathbf{p}}^0_3 \right) \end{aligned} \tag{2.66}$$

$$\begin{aligned} \ddot{\mathbf{p}}^n_3 = {} & \mathbf{R}^n_b(\boldsymbol{\Theta}) \mathbf{S}(\boldsymbol{\omega}^n_{nb}) \left(\mathbf{v}^b_o + \mathbf{S}(\boldsymbol{\omega}^n_{nb}) \left(\mathbf{p}^b_{b,0} + \mathbf{R}^b_0 \mathbf{p}^0_3 \right) + \mathbf{R}^b_0 \dot{\mathbf{p}}^0_3 \right) \\ & + \mathbf{R}^n_b(\boldsymbol{\Theta}) \left(\dot{\mathbf{v}}^b_o + \mathbf{S}(\dot{\boldsymbol{\omega}}^n_{nb}) \left(\mathbf{p}^b_{b,0} + \mathbf{R}^b_0 \mathbf{p}^0_3 \right) + \mathbf{S}(\boldsymbol{\omega}^n_{nb}) \mathbf{R}^b_0 \dot{\mathbf{p}}^0_3 + \mathbf{R}^b_0 \ddot{\mathbf{p}}^0_3 \right) \end{aligned} \tag{2.67}$$

$$\begin{aligned} \ddot{\mathbf{p}}^n_3 = {} & \mathbf{R}^n_b(\boldsymbol{\Theta}) \left(\mathbf{S}(\boldsymbol{\omega}^n_{nb}) \mathbf{v}^b_o + \left(\mathbf{S}(\boldsymbol{\omega}^n_{nb})^2 + \mathbf{S}(\dot{\boldsymbol{\omega}}^n_{nb}) \right) \left(\mathbf{p}^b_{b,0} + \mathbf{R}^b_0 \mathbf{p}^0_3 \right) \right) \\ & + \mathbf{R}^n_b(\boldsymbol{\Theta}) \left(2\mathbf{S}(\boldsymbol{\omega}^n_{nb}) \mathbf{R}^b_0 \dot{\mathbf{p}}^0_3 + \mathbf{R}^b_0 \ddot{\mathbf{p}}^0_3 \right) \end{aligned} \tag{2.68}$$

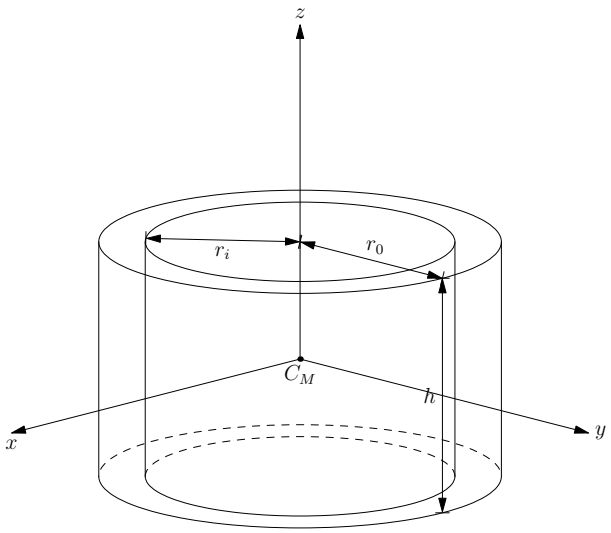

Figure 2.5: Cylinder inertia.

2.6 Model parameters

Configuring the crane model requires the DH parameters d_1, a_2 and a_3, the parameters listed in Section 2.4.2, and the position of the crane base in the b-frame, $\mathbf{p}^b_{b,0}$. This is a total of 28 parameters.

As a starting point for the configuration, it is assumed that the maximum lifting capacity should be around 100 t safe working load (SWL). A typical subsea crane in this range, is the Hydramarine cranes installed on the vessels MV SIEM TBN 323 and 326, [24], shown in Figure 2.1. Since the author does not hold actual data for the crane, the required parameters are estimated based on the illustration in Figure 2.1. By studying the schematic drawing, the following DH parameters are obtained:

$$d_1 = 3.9 \text{ m} \tag{2.69}$$
$$a_2 = 21.1 \text{ m} \tag{2.70}$$
$$a_3 = 12.7 \text{ m} \tag{2.71}$$

The mass of the crane king is estimated by assuming that the king has the shape of a cylindrical annulus as shown in Figure 2.5. By assuming the king is made in steel with density 7800 kg/m^3 with an outer radius $r_o = 1.8$ m and an inner radius $r_i = 1.65$ m, and the cylinder height is $h = d_1$, the mass is

$$m_1 \approx 49 \text{ t}, \tag{2.72}$$

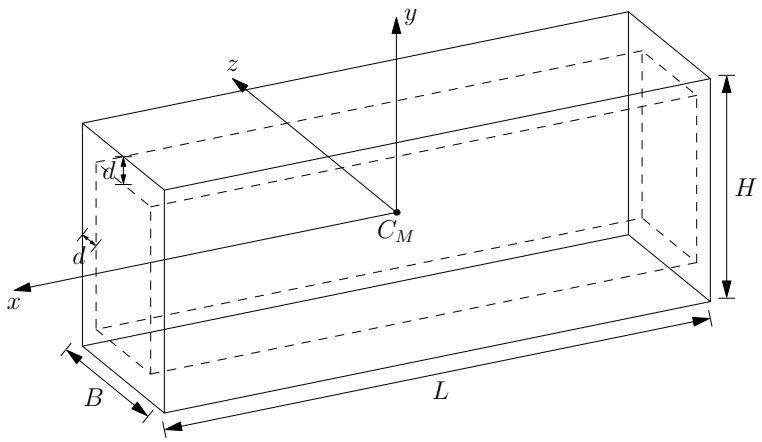

Figure 2.6: Box boom inertia.

and the inertia tensor is

$$\mathbf{I}_1 \approx \begin{bmatrix} 8.7 \cdot 10^4 & 0 & 0 \\ 0 & 8.7 \cdot 10^4 & 0 \\ 0 & 0 & 1.5 \cdot 10^5 \end{bmatrix} \text{ kg m}^2 \tag{2.73}$$

by the procedure in Appendix A.1. Since the slewing motion is not regarded in the model, these values do not have any impact on the crane response.

The knuckle boom and knuckle jib are assumed to be hollow, rectangular box-shaped made with $d = 0.03$ m thick steel plates as shown in Figure 2.6.

From Figure 2.1 the average knuckle boom breadth is found to be approximately $B = 0.75$ m, and the average height is approximately $H = 2$ m. Together with the boom length $L = a_2$, the knuckle boom mass

$$m_2 \approx 27 \text{ t}, \tag{2.74}$$

and the inertia tensor

$$\mathbf{I}_2 \approx \begin{bmatrix} 1.6 \cdot 10^4 & 0 & 0 \\ 0 & 1.2 \cdot 10^4 & 0 \\ 0 & 0 & 1.0 \cdot 10^6 \end{bmatrix} \text{ kg m}^2 \tag{2.75}$$

are found by the procedure in Appendix A.2.

Correspondingly, the mass and inertia for Link 3 are found by assuming

$$B = 0.50 \text{ m} \tag{2.76}$$

$$H = 1.4 \text{ m} \tag{2.77}$$

$$L = a_3, \tag{2.78}$$

which yields

$$m_3 \approx 11 \text{ t} \tag{2.79}$$

and

$$\mathbf{I}_3 \approx \begin{bmatrix} 3.1 \cdot 10^3 & 0 & 0 \\ 0 & 2.3 \cdot 10^3 & 0 \\ 0 & 0 & 1.5 \cdot 10^5 \end{bmatrix} \text{ kg m}^2 \tag{2.80}$$

The coordinate vectors required for the RNE scheme are defined as follows: The general vector from the origin of Frame $i-1$ to the origin of Frame i is given by

$$\mathbf{r}^i_{i-1,i} = [a_i \quad d_i \sin\alpha_i \quad d_i \cos\alpha_i]^T, \tag{2.81}$$

which by the DH table yields the specific vectors

$$\mathbf{r}^1_{0,1} = [0 \quad d_1 \quad 0]^T, \tag{2.82}$$

$$\mathbf{r}^2_{1,2} = [a_2 \quad 0 \quad 0]^T, \tag{2.83}$$

and

$$\mathbf{r}^3_{2,3} = [a_3 \quad 0 \quad 0t]^T \tag{2.84}$$

By the assumption that the links have homogenous mass distributions, the vector from Frame $i-1$ to the centre of mass of Link i is

$$\mathbf{r}^i_{i-1,C_i} = \frac{1}{2}\mathbf{r}^i_{i-1,i}, \tag{2.85}$$

and the vector from Frame i to the centre of mass of Link i is

$$\mathbf{r}^i_{i,C_i} = \mathbf{r}^i_{i-1,C_i} - \mathbf{r}^i_{i-1,i} = \frac{1}{2}\mathbf{r}^i_{i-1,i} - \mathbf{r}^i_{i-1,i} = -\frac{1}{2}\mathbf{r}^i_{i-1,i} \tag{2.86}$$

Estimating the viscous friction coefficients is carried out as follows: Assuming that the considered link is given an initial rotational velocity $\omega(0)$ about the joint's axis of rotation, and that no other forces act on the link, the system's dynamic equation is given by

$$J_i\dot{\omega} = -F_{vi}\omega, \tag{2.87}$$

where J_i is element (3,3) in the link's moment of inertia about the axis of rotation. The time domain solution of Equation (2.87) is

$$\omega(t) = \omega(0)e^{-\frac{F_{vi}}{J_i}t} \tag{2.88}$$

By assuming that the rotational velocity has been reduced by a factor $\alpha \in (0,1)$ after $t = t_1$ seconds, the viscous damping coefficient is given by

$$F_{vi} = -\frac{J_i \ln(\alpha)}{t_1} \tag{2.89}$$

For all joints $\alpha = 0.3$ and $t_1 = 5$ s are chosen. The moment of inertia for the king link is given directly by element (3,3) in the inertia tensor $\mathbf{I}_1$, i.e.

$$J_1 = 1.1 \cdot 10^6 \text{ kg m}^2 \tag{2.90}$$

For the knuckle boom and knuckle jib boom the moment of inertia is found by the parallel axes theorem according to

$$J_2 = I_{2_{(3,3)}} + m_2 \left(\frac{a_2}{2}\right)^2 \approx 4.0 \cdot 10^6 \text{ kg m}^2, \tag{2.91}$$

and

$$J_3 = I_{3_{(3,3)}} + m_3 \left(\frac{a_3}{2}\right)^2 \approx 5.9 \cdot 10^5 \text{ kg m}^2, \tag{2.92}$$

This gives the following values for the viscous friction coefficients:

$$F_{v1} \approx 3.6 \cdot 10^4 \text{ kg m}^2/\text{s} \tag{2.93}$$

$$F_{v2} \approx 9.5 \cdot 10^5 \text{ kg m}^2/\text{s} \tag{2.94}$$

$$F_{v3} \approx 1.4 \cdot 10^5 \text{ kg m}^2/\text{s} \tag{2.95}$$

The Coulomb joint friction coefficients F_{si} are set to zero because the author does not possess the values and does not have any procedure to determine these coefficients.

The chosen vector for the position of the crane base in the b-frame is

$$\mathbf{p}_{b,0}^b = [0 \quad 0 \quad -12]^T \tag{2.96}$$

2.7 Initialisation

The initial values required for the crane model are $\mathbf{q}(0)$ and $\dot{\mathbf{q}}(0)$. There is no immediate reason to have a non-zero initial joint velocity for any of the joints; hence, the initial joint velocity is

$$\dot{\mathbf{q}}(0) = \mathbf{0} \tag{2.97}$$

The initial joint angles may be taken as any reasonable values, and will be stated for each simulation case in Chapter 7.

Chapter 3

Luffing the crane booms – Hydraulics

3.1 Introduction

As can be seen in Figure 2.1, the crane's luffing angles (Joint 2 and 3) are actuated by hydraulic cylinders. According to [31], two common schemes for hydraulic actuator control are available in the literature. These are pump control and valve control. In pump controlled systems, the rate and direction of flow supplied to the motor is controlled by adjusting the displacement of the pump; In valve controlled systems, a hydraulic power unit (HPU) provides the supply pressure, and the rate and direction of flow to the motor is controlled by the control valve. There are two types of hydraulic motors: Rotary and linear (i.e. a cylinder).

Both schemes may be used for the same applications. However, the two schemes have different properties which may deem one scheme more appropriate than the other with regard to specific applications.

The most important differences are that the valve controlled scheme usually has higher bandwidth, and the pump controlled scheme is more power efficient. The valve controlled scheme usually is below 67 %, whereas the pump controlled scheme may be as high as 90 %. For a thorough review of hydraulic systems, refer to [31] and its enclosed references [18], [17] and [9].

Which scheme is used on the crane in Figure 2.1 is unknown to the author. In [30] the valve controlled scheme is used for luffing crane booms, and this will thus be done here.

The hydraulic system is assumed to consist of a constant pressure pump with balance valve, a spool-controlled four-way valve and a single-rod cylinder for each joint as shown in Figure 3.1. The constant pressure pump is assumed to be

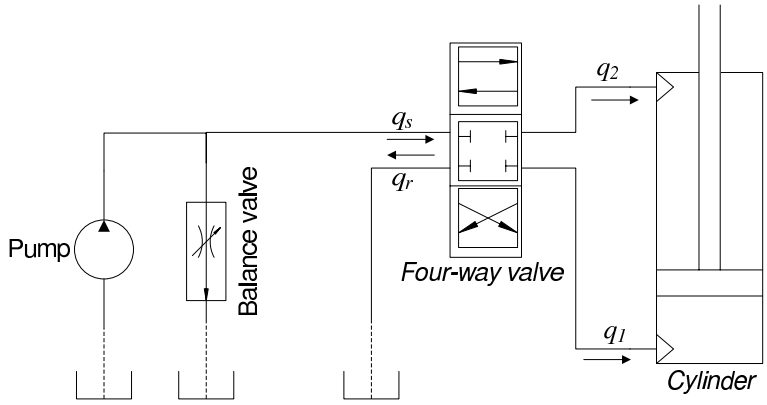

Figure 3.1: Schematics of the hydraulic system for the knuckle and knuckle jib booms.

able to provide any volumetric flow at the given constant supply pressure. The four-way valve is assumed to be matched and symmetric with a critical spool and rectangular orifices, and the orifice flow is regularised. Hydraulic fluid in the valve is considered to be incompressible. Because of the assumption of a critical spool, there is neither leakage nor dead band in the valve. Practical valves, however, are usually designed to be overlapped such that there is leakage in the valve; see [18].

The cylinder is modelled by the mass balance for the two cylinder volumes, and the hydraulic fluid in the cylinder is assumed to be compressible. Normally, the equation of motion for the piston would be part of the model; however, since the cylinder is connected to the crane structure, the piston motion is expressed by the respective joint angle motion, and the mass of the cylinder and rod is included in the crane links.

Normally, arrangements are provided on the cylinders in order to avoid over and under pressure, see [17]. This is not included in the model.

Transmission lines between the components are not regarded. This implies the assumption that the hydraulic fluid is incompressible in the transmission lines. The force applied by the cylinder must be input to the crane's equation (2.21) of motion as a joint torque. This mapping is found by geometric considerations in Section 3.6.

Restrictions on the piston travel are included in order to ensure the validity of the hydraulic cylinder model. This is implemented by setting the valve position to zero when the cylinder piston reaches a limit and stopping the piston motion.

A model for actuation of the king/slewing motion is not considered in this thesis since the payload and hoisting cable model only comprises vertical forces.

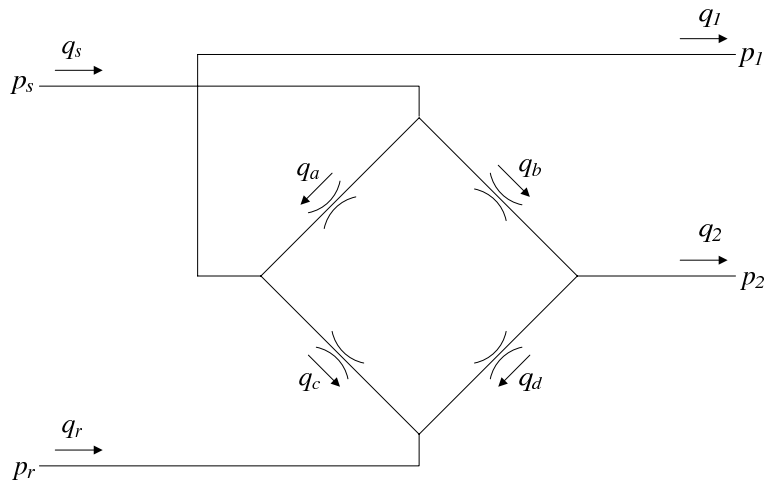

Figure 3.2: Four-way valve schematics. The illustration is adapted from [10].

3.2 Constant pressure pump

The constant pressure pump and balance valve are assumed to provide a constant pressure p_s to the hydraulic system regardless of power consumption $P_p = p_s q_s$, where q_s is the volumetric flow from the pump to the four-way valve as shown in Figure 3.1.

3.3 Four-way valve

The four-way valve model used in [30] is of the type spool-controlled, matched and symmetric with critical spool derived in [10]. By varying the spool position the flow areas of the valve's orifices are varied. A matched and symmetric valve has the properties given by Equation (3.5), and a critical spool means that there is no dead band from spool position to port area, and there is no leakage in the valve. Refer to [18] for a thorough review of four-way valves.

The valve consists of four restrictions/orifices connected as shown in Figure 3.2 with the flows q_a, q_b, q_c and q_d. From the illustration and the assumption that the hydraulic fluid in the valve is incompressible, we see that the flows into and out of the four-way valve are given by the four restrictions a, b, c and d as

$$q_s = q_a + q_b, \qquad q_r = q_c + q_d \tag{3.1}$$

$$q_1 = q_a - q_c, \qquad q_2 = q_b - q_d \tag{3.2}$$

The flow through a restriction can be described by the regularised flow characteristic

$$q(A, \Delta p) = \begin{cases} \frac{3\nu Re_{tr}}{4} \frac{\sqrt{\pi}}{2} \sqrt{A} \frac{A\Delta p}{F_{tr}} \left(3 - \frac{A\Delta p}{F_{tr}}\right), & A\Delta p \leq F_{tr} \\ C_d A \sqrt{\frac{2}{\rho} \Delta p}, & F_{tr} \leq A\Delta p \end{cases} \tag{3.3}$$

where

$$F_{tr} = \frac{9Re_{tr}^2 \rho \nu^2}{8C_d^2} \frac{\pi}{4} \tag{3.4}$$

The parameters used in Equations (3.3) and (3.4) are the threshold Reynolds number $Re_{tr} = 1000$, hydraulic fluid density $\rho = 900\,\mathrm{kg/m^3}$, kinematic viscosity $\nu = 30 \cdot 10^{-6}\,\mathrm{m^2/s}$ and discharge coefficient $C_d = 0.6$. The values and the regularised flow characteristic are taken from [10].

The regularised flow in Equation (3.3) describes the flow as laminar for low Reynolds numbers, and turbulent for high numbers, and the threshold for switching between laminar and turbulent flow is given by Equation (3.4).

The argument A in Equation (3.3) is the port opening. For a matched and symmetric four-way valve, the port areas are designed such that

$$A_a(x_v) = A_d(x_v) = A_b(-x_v) = A_c(-x_v), \tag{3.5}$$

and with a critical spool and rectangular orifices, the areas may be expressed as a function of the spool position x_v according to

$$A_a(x_v) = A_d(x_v) = \begin{cases} 0, x_v \leq 0 \\ bx_v, x_v \geq 0 \end{cases} \tag{3.6}$$

$$A_b(x_v) = A_c(x_v) = \begin{cases} -bx_v, x_v \leq 0 \\ 0, x_v \geq 0 \end{cases} \tag{3.7}$$

The flow through the restrictions are thus given by

$$q_a = q_a(A_a, p_s - p_1) \tag{3.8}$$

$$q_b = q_b(A_b, p_s - p_2) \tag{3.9}$$

$$q_c = q_b(A_c, p_1 - p_r) \tag{3.10}$$

$$q_d = q_b(A_d, p_2 - p_r) \tag{3.11}$$

with port areas given by Equations (3.6) and (3.7), and the pressure drop is given by Figure 3.2.

Only the port areas, i.e. the area constant b and spool position limits $|x_v| \leq x_{v_{max}}$, must be determined for the valve model. – The pressure drop over the restrictions are given by the supply and return pressures p_s, p_r, and the pressures in the cylinder volumes, p_1, p_2, are given by the dynamic equations for the hydraulic cylinder derived in Section 3.4.

In [30] the area constant is expressed as

$$b = \frac{q_{max}}{C_d x_{v_{max}}} \sqrt{\frac{3\rho}{p_s}}, \tag{3.12}$$

where q_{max} is the maximum flow through the orifice, and $x_{v_{max}}$ is the maximum opening of the orifices of the valve. Since the valve is symmetric, q_{max} and $x_{v_{max}}$

will be the same for all four orifices. The maximal flow must be chosen so as to allow for a certain maximum piston speed, $v_{p_{max}}$. This is accomplished by choosing

$$q_{max} = A_p v_{p_{max}}, \tag{3.13}$$

where A_p is the piston area defined in Section 3.4. This gives the area coefficient

$$b = \frac{A_p v_{p_{max}}}{C_d x_{v_{max}}} \sqrt{\frac{3\rho}{p_s}}, \tag{3.14}$$

By noting that the port area is given by

$$A = x_v b = \frac{x_v}{x_{v_{max}}} \frac{A_p v_{p_{max}}}{C_d} \sqrt{\frac{3\rho}{p_s}}, \tag{3.15}$$

the port area may be expressed by the spool position in relative terms by

$$A = x_v b = \tilde{x}_v \tilde{b}, \tag{3.16}$$

where

$$\tilde{b} = \frac{A_p v_{p_{max}}}{C_d} \sqrt{\frac{3\rho}{p_s}}, \tag{3.17}$$

and

$$\tilde{x}_v = \frac{x_v}{x_{v_{max}}} \in [-1, 1], \tag{3.18}$$

In this way, the maximum spool position need not be defined, only the area coefficient $\tilde{b}$.

Spool dynamics are incorporated by a second order transfer function according to

$$\frac{x_v}{x_{v_d}}(s) = \frac{1}{\frac{s^2}{\omega_h^2} + 2\zeta_h \frac{s}{\omega_h} s + 1} \tag{3.19}$$

and taking the natural frequency to be $\omega_h = 100$ rad/s and relative damping to be $\zeta_h = 1$, i.e. critically damped system. This approach is also used in [30].

3.4 Single-rod hydraulic cylinder

The dynamic model for the single-rod hydraulic cylinder illustrated in Figure 3.3 is described in [10] as

$$\frac{V_{10} + A_1 x_p}{\beta} \dot{p}_1 = -C_{im}(p_1 - p_2) - C_{em} p_1 - A_1 \dot{x}_p + q_1 \tag{3.20}$$

$$\frac{V_{20} - A_2 x_p}{\beta} \dot{p}_2 = -C_{im}(p_2 - p_1) - C_{em} p_2 + A_2 \dot{x}_p + q_2 \tag{3.21}$$

$$m_t \ddot{x}_p = -B_p \dot{x}_p + A_1 p_1 - A_2 p_2 - F_L, \tag{3.22}$$

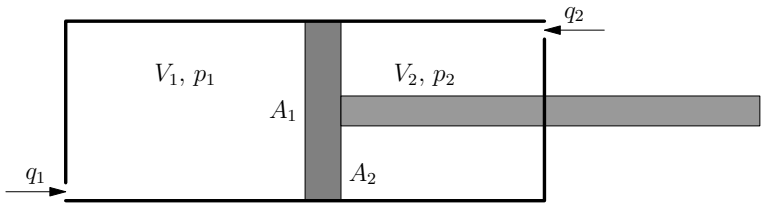

Figure 3.3: Schematics of a single-rod cylinder. The illustration is adapted from citeModSim.

where p_1 and p_2 are the pressures, A_1 and A_2 are the cross sectional areas, V_{10} and V_{20} are the chamber volumes when the piston position x_p is zero, and q_1 and q_2 are the flow into the chamber for the respective chambers, β is the bulk modulus, C_{im} and C_{em} are the internal and external leakage coefficients, B_p is the cylinder viscous friction coefficient, m_t is the mass of the piston and load, and F_L is the external load force. The bulk modulus is taken from [10] to be $\beta = 7 \cdot 10^8$ Pa, which, according to [10], may change by a factor of 10.

By assuming that the piston has cross sectional area A_p, and the rod has cross sectional area A_r, the cross sectional areas for the volumes are given by

$$A_1 = A_p, \quad A_2 = A_p - A_r, \tag{3.23}$$

Given the force the cylinder must be able to generate, F_0, and the supply pressure p_s, the piston area is found as

$$A_p = \frac{F_0}{p_s}, \tag{3.24}$$

and the volumes at $x_p = 0$ are

$$V_{10} = 0 \tag{3.25}$$

$$V_{20} = A_1 x_s, \tag{3.26}$$

where x_s is the piston stroke defined in Section 3.7.

The mass of the piston and load is found by assuming that it is given by the mass of the cylinder rod. Assuming that the rod is hollow such that it has a mass density of one fourth to that of steel density, the mass is given by

$$m_t = \frac{1}{4}\rho_{steel} A_r L_{rod}, \tag{3.27}$$

where L_{rod} is the length of the rod defined in Section 3.7.

The coefficient for viscous friction B_p is given in [30] as

$$B_p = 4\zeta A \sqrt{\frac{\beta m_t}{V_t}}, \tag{3.28}$$

where $\zeta \in (0.1, 0.5)$ is relative damping, $A = A_2$ and $V_t = \frac{1}{2}(A_1 + A_2)x_s$. The leakage coefficients C_{im} and C_{em} are given by the equations

$$C_{tm} = B_p(1-\alpha)\frac{V_t}{4m_t\beta} \tag{3.29}$$

$$C_{tm} = C_{im} + \frac{1}{2}C_{em} \tag{3.30}$$

$$C_{em} = 0.1C_{im} \tag{3.31}$$

where α is a scaling factor. The derivation of B_p, C_{im} and C_{em} is reproduced in Appendix B.

For simplicity, the leakage is zero in most simulations. If leakage is present, the booms will creep, and extra controller functionality should be included in the model in order to keep the booms at constant luffing angles.

3.5 Change of coordinates for the piston motion

As stated in Section 3.1, the piston motion may be expressed by the joint angle motion for the respective joint. Simulations in [30] show that not doing so, but including the piston equation of motion (Equation (3.22)) in the model, leads to inconsistencies between the joint and piston motions.

This problem is circumvented by expressing the piston motion by the joint angle motion and geometric considerations as shown below. The piston mass for Link i, m_{t_i}, is included in the model by adding it to the mass of Link $i-1$, e.g. the total mass of the king is the mass of the king itself plus the mass of the cylinder of Joint 2. This will also increase the moment of inertia for the respective link.

The force applied from the cylinder rod F is

$$F = -B_p\dot{x}_p + A_1p_1 - A_2p_2 \tag{3.32}$$

Figure 3.4 illustrates the geometry of the cylinder – and its attachment points P_1 and P_2 on the crane structure – and the joint – at the intersection of lines K and L. K and L denote the constant distance from the joint to the attachment points, and the cylinder goes along P. The principle works for all joints, but during the explanation of the principle, Joint 2 is considered. K_1 goes along the centre line of the king, and K_2 is the distance from the king centre line to the cylinder attachment point P_1 on the king. L_1 is the distance along the x_2-axis to the attachment point P_2 on Link 2, and L_2 is the distance from the x_2-axis to the cylinder attachment point on the knuckle boom. The angle between the lines K_1 and K is denoted by k, and l is the angle between the lines L_1 and L.

The distance P between the cylinder attachment points P_1, P_2, is found by the cosine rule

$$P = \sqrt{K^2 + L^2 - 2KL\cos(c)} \tag{3.33}$$

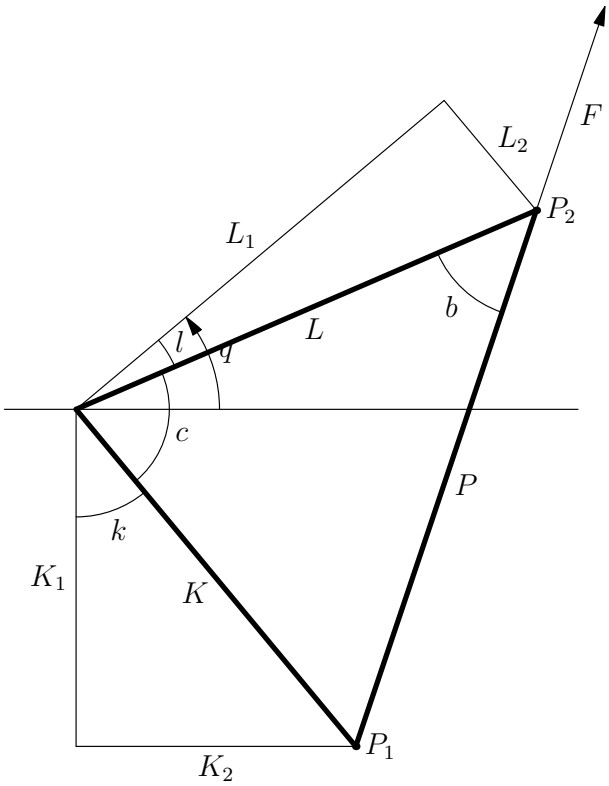

Figure 3.4: Link-cylinder geometry.

For Joints 2 and 3 c is given by

$$c_2 = q_2 + \frac{\pi}{2} - k - l \tag{3.34}$$

$$c_3 = q_3 + \pi - k - l, \tag{3.35}$$

respectively. The piston position is given by

$$x_p = P - L_{rod}, \tag{3.36}$$

where L_{rod} is the length of the cylinder rod, and the piston velocity by

$$\dot{x}_p = \dot{P} = \frac{\dot{q}LK\sin(c)}{P} \tag{3.37}$$

The rod length is defined in Section 3.7.

3.6 Mapping the cylinder force to joint torque

The force F applied by the hydraulic cylinder must be mapped into the resulting joint torque. With reference to Figure 3.4, the mapping is given by

$$\tau = FL\sin(b) \tag{3.38}$$

By the sine rule

$$\frac{\sin(b)}{K} = \frac{\sin(c)}{P}, \tag{3.39}$$

and the resulting expression for the mapping is

$$\tau = \frac{LK\sin(c)}{P}F \tag{3.40}$$

A simpler approach would be to assume that the cylinder was attached on the link's centre lines, i.e. $K_2 = L_2 = 0$. However, this will result in an applied torque which is considerably lower than the torque given by the more elaborate approach.

3.7 Limited piston travel

For Equations (3.20) and (3.21) to be valid, the piston position must be limited to the range $x_p \in [0, x_s]$. Otherwise, either of the cylinder volumes will be negative. Also, on the limits $x_p = 0$ and $x_p = x_s$ the volume of Chamber 1 and Chamber 2, respectively, will be zero, which results in division by zero in the respective equation. Hence, in order to ensure numerical stability, the piston travel must be in the range $x_p \in (0, x_s)$.

In physical cylinders there usually is some arrangement to reduce the piston velocity gradually as the piston is approaching one of the cylinder ends. This arrangement is incorporated in order to avoid pressure peaks when the piston runs into the cylinder wall, and may for instance be a mechanical solution or programmed control of the valve spool position depending on the piston position, see [17].

This functionality is integrated into the hydraulics model by the latter principle, and is chosen to the author's convenience.

By studying Figure 2.1, limits for the joint angles of Joints 2 and 3 may be found denoted by $q_{2_{upper}}$, $q_{2_{lower}}$, $q_{3_{upper}}$ and $q_{3_{lower}}$. The joint limits put restrictions on the length of P, such that $P \in [P_{min}, P_{max}]$, where the limits are given by

$$P_{max} = \sqrt{K^2 + L^2 - 2KL\cos(c_{upper})}, \tag{3.41}$$

where

$$c_{upper} = \begin{cases} q_{2_{upper}} + \frac{\pi}{2} - k - l & \text{for Joint 2} \\ q_{3_{upper}} + \pi - k - l & \text{for Joint 3} \end{cases} \tag{3.42}$$

and

$$P_{min} = \sqrt{K^2 + L^2 - 2KL\cos(c_{lower})}, \tag{3.43}$$

where

$$c_{lower} = \begin{cases} q_{2_{lower}} + \frac{\pi}{2} - k - l & \text{for Joint 2} \\ q_{3_{lower}} + \pi - k - l & \text{for Joint 3} \end{cases} \tag{3.44}$$

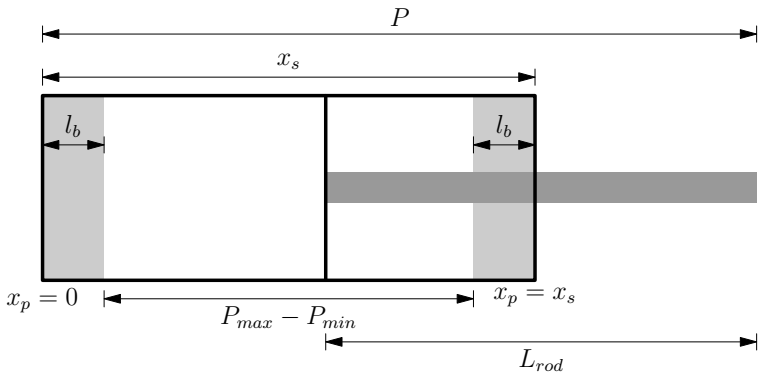

Figure 3.5: Cylinder with buffer zones in both ends.

Consider Figure 3.5. By defining a buffer length l_b in both ends of the cylinder, it is seen that the length of the rod is given by

$$L_{rod} = P_{min} - l_b, \tag{3.45}$$

and that the cylinder stroke (or, equivalently, the length of the cylinder) is given by

$$x_s = P_{max} - P_{min} + 2l_b \tag{3.46}$$

The cylinder model is valid as long as $x_p \in (0, x_s)$. However, when the piston reaches either of the buffer zones, the valve spool position will be set to zero stopping the piston motion. The spool position will now be zero until a command to move the spool in the opposite direction is given. The block diagram for the function is found in Figure C.3.

3.8 Model parameters

The hydraulics model requires 30 parameters, and since it will be used to actuate both the knuckle boom and knuckle jib, a total of 60 parameters are required. Some general parameters are stated in Section 3.3 for the four-way valve, and by the assumptions presented during the model derivation, the parameters required for both models are the ones listed in Table 3.1. This gives a total of 28 parameters.

The supply pressure p_s from the constant pressure pump and the return pressure p_r are chosen in accordance with [30]. The maximum piston velocity $v_{p_{max}}$ and the force F_0 that the cylinder is designed to hold are chosen by simulations in order to ensure reasonable and stable simulations. The only justification for the choice of the cross sectional area A_r of the rod is that it should be smaller than the piston cross sectional area and give a reasonable value for the mass of the piston and load m_t. The relative damping ζ in the expression for the viscous

Table 3.1: Configuration parameters for the hydraulics models.

Parameter	Joint 2	Joint 3
p_s	30 MPa	30 MPa
p_r	0 Pa	0 Pa
$v_{p_{max}}$	0.1 m/s	0.1 m/s
F_0	9.81 MN	3.92 MN
A_r	$0.2 \cdot A_p$	$0.2 \cdot A_p$
ζ	0.5	0.5
α	1	1
q_{lower}	$0°$	$-150°$
q_{upper}	$70°$	$-20°$
K_1	3.9 m	8.1 m
K_2	1.8 m	2.3 m
L_1	8.7 m	2.7 m
L_2	2.3 m	0 m
l_b	0.3 m	0.2 m

piston friction B_p is chosen as high as [30] allows in order to ensure as good simulations as possible. The scaling factor α is chosen in order to simulate without leakage in the cylinder. The parameters q_{lower}, q_{upper}, K_1, K_2, L_1 and L_2 are found by studying Figure 2.1. The buffer length l_b is chosen by tuning in order to obtain stable simulations. However, if reaching a limit with too high joint velocity, e.g. if lowering the knuckle boom too fast, it is still possible to force the piston position beyond the limit $x_p \in (0, x_s)$.

The remaining model parameters may now be defined by the parameters in Table 3.1.

$$K = \sqrt{K_1^2 + K_2^2} \approx \begin{cases} 4.3 \text{ m for Joint 2} \\ 8.4 \text{ m for Joint 3} \end{cases} \tag{3.47}$$

$$L = \sqrt{L_1^2 + L_2^2} \approx \begin{cases} 9.0 \text{ m for Joint 2} \\ 2.7 \text{ m for Joint 3} \end{cases} \tag{3.48}$$

$$c_2 = q_2 + \frac{\pi}{2} - \tan\left(\frac{K_2}{K_1}\right) - \tan\left(\frac{L_2}{L_1}\right) \approx q_2 + 0.81 \text{ rad} \tag{3.49}$$

$$c_3 = q_3 + \pi - \tan\left(\frac{K_2}{K_1}\right) - \tan\left(\frac{L_2}{L_1}\right) \approx q_3 + 2.9 \text{ rad} \tag{3.50}$$

$$P_{min} = \sqrt{K^2 + L^2 - 2KL\cos(c_{lower})} \approx \begin{cases} 6.8 \text{ m for Joint 2} \\ 5.8 \text{ m for Joint 3} \end{cases} \tag{3.51}$$

$$P_{max} = \sqrt{K^2 + L^2 - 2KL\cos(c_{upper})} \approx \begin{cases} 11.5 \text{ m for Joint 2} \\ 10.7 \text{ m for Joint 3} \end{cases} \tag{3.52}$$

$$L_{rod} = P_{min} - l_b \approx \begin{cases} 6.5 \text{ m for Joint 2} \\ 5.6 \text{ m for Joint 3} \end{cases} \tag{3.53}$$

$$x_s = P_{max} - P_{min} + 2l_b \approx \begin{cases} 5.4 \text{ m for Joint 2} \\ 5.3 \text{ m for Joint 3} \end{cases} \tag{3.54}$$

$$A_p = A_1 = \frac{F_0}{p_s} \approx \begin{cases} 0.39 \text{ m}^2 \text{ for the cylinder of Joint 2} \\ 0.16 \text{ m}^2 \text{ for the cylinder of Joint 3} \end{cases} \tag{3.55}$$

$$A_r = 0.2A_p \approx \begin{cases} 0.079 \text{ m}^2 \text{ for the cylinder of Joint 2} \\ 0.031 \text{ m}^2 \text{ for the cylinder of Joint 3} \end{cases} \tag{3.56}$$

$$A_2 = A_p - A_r = 0.8A_p \approx \begin{cases} 0.31 \text{ m}^2 \text{ for the cylinder of Joint 2} \\ 0.13 \text{ m}^2 \text{ for the cylinder of Joint 3} \end{cases} \tag{3.57}$$

The area coefficients are *

$$\tilde{b} = \frac{A_p v_{p_{max}}}{C_d}\sqrt{\frac{3\rho}{p_s}} \approx \begin{cases} 0.46 \text{ m}^2 \text{ for the valve of Joint 2} \\ 0.18 \text{ m}^2 \text{ for the valve of Joint 3} \end{cases} \tag{3.58}$$

The mass of the piston and load is given by

$$m_t = \frac{1}{4}\rho_{steel} A_r L_{rod} \approx \begin{cases} 1000 \text{ kg for the cylinder of Joint 2} \\ 344 \text{ kg for the cylinder of Joint 3} \end{cases}, \tag{3.59}$$

where $\rho_{steel} = 7800 \text{ kg/m}^3$ has been used.

The values for the masses and inertia tensors of the crane links are now

$$m_1 = 50 \text{ t} \tag{3.60}$$

$$m_2 = 27 \text{ t} \tag{3.61}$$

$$m_3 = 11 \text{ t} \tag{3.62}$$

$$\mathbf{I}_1 \approx \begin{bmatrix} 8.9 \cdot 10^4 & 0 & 0 \\ 0 & 8.9 \cdot 10^4 & 0 \\ 0 & 0 & 1.5 \cdot 10^5 \end{bmatrix} \text{ kg m}^2 \tag{3.63}$$

$$\mathbf{I}_2 \approx \begin{bmatrix} 1.6 \cdot 10^4 & 0 & 0 \\ 0 & 1.2 \cdot 10^4 & 0 \\ 0 & 0 & 1.0 \cdot 10^6 \end{bmatrix} \text{ kg m}^2 \tag{3.64}$$

$$\mathbf{I}_3 \approx \begin{bmatrix} 3.1 \cdot 10^3 & 0 & 0 \\ 0 & 2.3 \cdot 10^3 & 0 \\ 0 & 0 & 1.5 \cdot 10^5 \end{bmatrix} \text{ kg m}^2, \tag{3.65}$$

*The area coefficients given by the equation are quite large, but they are still chosen to be used in the simulations. The simulator has also been tested with smaller, more reasonable values, and the simulations are still realistic.

and the viscous joint friction coefficients are

$$F_{v1} \approx 3.6 \cdot 10^4 \text{ kg m}^2/\text{s} \tag{3.66}$$
$$F_{v2} \approx 9.8 \cdot 10^5 \text{ kg m}^2/\text{s} \tag{3.67}$$
$$F_{v3} \approx 1.4 \cdot 10^5 \text{ kg m}^2/\text{s} \tag{3.68}$$

3.9 Initialisation

The hydraulics model requires initial values for the pressure of the two cylinder volumes in Equations (3.20) and (3.21). These are found by simulating one step of the crane model in order to find the resultant torques τ_i acting in each joint. In steady state the force from the cylinder on the boom counteracts this torque. The required force from the cylinder is found by rearranging Equation (3.40) to

$$F = \frac{P}{LK \sin(c)}\tau, \tag{3.69}$$

where c is given by the initial joint angles and offsets for each joint as described in Section 3.5.

Equation (3.32) gives the expression

$$F = A_1 p_1 - A_2 p_2 \tag{3.70}$$

for the force in steady state. By assuming the relation

$$p_1 + p_2 = p_s + p_r, \tag{3.71}$$

the initial pressures are given by

$$p_2 = \frac{A_1(p_s + p_r) - F}{A_1 + A_2} \tag{3.72}$$

and

$$p_1 = p_s + p_r - p_2 \tag{3.73}$$

The assumption given in Equation (3.71) is justified as follows: It is assumed that the valve model for turbulent flow

$$q(A, \Delta p) = C_d A \sqrt{\frac{2}{\rho}\Delta p} \tag{3.74}$$

applies and that the load is symmetric, i.e.

$$q_1 = -q_2 \tag{3.75}$$

Inserting the relations from Equation (3.2) gives

$$q_a - q_c = q_d - q_b \tag{3.76}$$

By assuming a positive spool position the port areas $A_c = A_b = 0$, and Equation (3.76) is reduced to

$$q_a = q_d \tag{3.77}$$

Next, the turbulent flow model is substituted into Equation (3.77)

$$C_d A_a \sqrt{\frac{2}{\rho}(p_s - p_1)} = C_d A_d \sqrt{\frac{2}{\rho}(p_2 - p_r)} \tag{3.78}$$

From Equation (3.6) we have that $A_a = A_d$, and the flow equation is reduced to

$$\sqrt{\frac{2}{\rho}(p_s - p_1)} = \sqrt{\frac{2}{\rho}(p_2 - p_r)} \tag{3.79}$$

Squaring both sides gives

$$\frac{2}{\rho}(p_s - p_1) = \frac{2}{\rho}(p_2 - p_r), \tag{3.80}$$

and finally, the pressure relation

$$p_s + p_r = p_1 + p_2 \tag{3.81}$$

Chapter 4

Payload and hoisting cable

4.1 Introduction

This chapter describes the dynamic model of the payload and hoisting cable. The model comprises a load attached to the lower end of a hoisting cable modelled as a linear spring-damper, and forces acting on the load, that is hoisting cable force, hydrodynamics and normal force from a supporting deck. The model handles the transitions between the lifting phases from the load is resting on a deck to lifting it through the air, into the water and back to the deck.

When landing a load on the seabed the added mass will increase exponentially with decreasing distance to the seabed. Also, the load may sink into the seabed. Such effects are not included in the model, and, hence, the model cannot simulate this scenario realistically.

The model is to a great extent based on a similar model derived in [28]. However, a different approach has been used for the normal force.

The derivation of the hydrodynamics is based on [11], and the derivation is based on potential theory and momentum considerations.

4.2 Assumptions

The model is limited to only considering vertical forces on the load and the hoisting cable. The top end of the cable is assumed to be at the boom tip. Exogenous variables are the boom tip motion, the nominal cable length, wave motions and the motions of the deck which the load is lifted from or landed onto. The force acting on the crane boom tip and the winch from the hoisting cable is derived in Section 4.8.

In the modelling it is assumed that the mass of the load M_l is a point mass positioned at the lower end of the hoisting rope. Then the sum of forces exerting

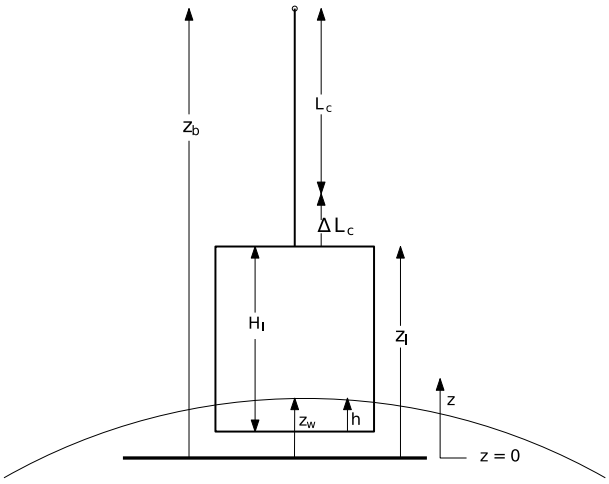

Figure 4.1: Definition of variables

the rope end/load can be written according to Newton's second law as

$$M_l \ddot{z}_l = \sum F, \tag{4.1}$$

where $\ddot{z}_l$ is the load's acceleration. The modelled forces are gravity G, the cable force F_c, normal force N, and the hydrodynamic force F_h. Hence, the sum of forces acting on the load can be written

$$\sum F = G + F_c + N + F_h \tag{4.2}$$

The derivation of the respective forces is summarised in the succeeding sections.

The one-dimensional axes system used in [28] is assumed to be inertial with positive axis upwards and origin at the mean free-surface water level, see Figure 4.1. As discussed in Section 2.5, the n-frame is also considered inertial. Since the payload and hoisting cable axes system has a positive vertical z-axis, and both the n-frame and the payload and hoisting cable axes system have their origins at the mean free-surface water level, representing the forces and motions of the payload and hoisting cable model in the n-frame is equivalent to multiplying the values by -1.

The positional variables defined in the figure denote the crane boom tip position z_b, the lower end of the hoisting rope (or, equivalently, the upper point of the load), z_l, and the wave elevation z_w. The nominal cable length L_c and the load height H_l are also denoted in the figure. The boom tip position (and its derivatives $\dot{z}_b$ and $\ddot{z}_b$) are provided by the crane model in Chapter 2, and the nominal cable length (and its derivatives $\dot{L}_c$ and $\ddot{L}_c$) are provided by the winch model in Chapter 5.

From the figure the elastic elongation of the cable ΔL_c is defined as

$$\Delta L_c = z_b - z_l - L_c \tag{4.3}$$

the submergence of the load h as

$$h = \begin{cases} 0 & z_w - z_l + H_l < 0 \\ z_w - z_l + H_l & z_w - z_l + H_l \geq 0, \end{cases} \tag{4.4}$$

and the relative submergence

$$\tilde{h} = \frac{h}{H_l} \tag{4.5}$$

The load submergence is assumed to be constant in space at any arbitrary time instant.

4.3 Force of gravity

The force of gravity applied to the load is

$$G = -M_l g, \tag{4.6}$$

where g is the acceleration of gravity.

4.4 Hydrodynamic forces

Expressions for the hydrodynamic force may be formulated depending on the load's position in the water. The positions/cases treated in [28] are water entry, water exit and fully submerged load. Also, the transitions between these cases are treated.

The general hydrodynamic force in [28] is given by

$$F_h = \underbrace{\frac{dA_{33}}{dh} f_{slam}(w, \dot{z}_l)}_{\text{Slamming}} + \underbrace{A_{33}(\dot{w} - \ddot{z}_l)}_{\text{Added mass}} + \underbrace{\rho_w \Omega(h) f_{FK}(\dot{w}, \dot{z}_l)}_{\text{Froude-Kriloff}} + \underbrace{\rho_w g \Omega(h)}_{\text{Buoyancy}} + \underbrace{F_{h_d}}_{\text{Damping}} \tag{4.7}$$

The slamming and added mass coefficients, and the expression for the submerged volume of the load, $\frac{dA_{33}}{dh}$, A_{33} and $\Omega(h)$, respectively, depend on the geometry of the load, and must be defined for a specific load geometry. Two load geometries where considered in [28], see Sections 4.4.1 and 4.4.2. The variable w is given by

$$w = \dot{z}_w e^{-\frac{\alpha_w}{H_s} z_s} \tag{4.8}$$

$$z_s = \max(0, z_w - z_l), \tag{4.9}$$

and describes the vertical wave velocity as a function of submergence z_s, and is used instead of the usual water surface elevation velocity, $\dot{z}_w$, in order to account for the decreasing wave affection on the load as it is being submerged. This

allows for the transitions between water entry to fully submerged load, and back to water exit. The parameter α_w is found to be

$$\alpha_w = 0.45 \tag{4.10}$$

by assuming that there is five percent effective wave affection at a submergence of $z_s = 20$ metres and significant wave height $H_s = 3$ metres.

The factors f_{slam} and f_{FK} are defined by

$$f_{slam}(w, \dot{z}_l) = \begin{cases} (w - \dot{z}_l)^2 & \text{if} \quad \dot{z}_l \leq 0 \\ 0 & \text{if} \quad \dot{z}_l > 0, \end{cases} \tag{4.11}$$

$$f_{FK}(\dot{w}, \dot{z}_l) = \begin{cases} \dot{w} & \text{if} \quad \dot{z}_l \leq 0 \\ 0 & \text{if} \quad \dot{z}_l > 0, \end{cases} \tag{4.12}$$

which make slamming and Froude-Kriloff forces active during water entry, but not during water exit.

The two alternative damping models presented in [28] are

$$F_{h_d} = \frac{1}{2}\rho_w C_D A_p \left|w - \dot{z}_l\right| (w - \dot{z}_l) \qquad \text{and} \tag{4.13}$$

$$F_{h_d} = B_1 (w - \dot{z}_l) + B_2 \left|w - \dot{z}_l\right| (w - \dot{z}_l) \tag{4.14}$$

The second alternative is the preferred model since it also incorporates linear damping, which is both physical and attractive with regard to numerical stability of the simulator.

The remaining constants introduced in the above equations are water density $\rho_w = 1025\ \text{kg/m}^3$, nondimensional quadratic drag coefficient C_D, projected area of the load A_p, linear damping coefficient B_1, and quadratic drag coefficient $B_2 = \frac{1}{2}\rho_w C_D A_p$.

By the above definitions, and the following definitions of the geometry specific factors, the transitions between the considered cases will be sensible.

4.4.1 Load geometry: Sphere

For a sphere with radius $H_l/2$ and submergence h the submerged volume of the load is

$$\Omega(h) = \frac{\pi}{3}\left(3\frac{H_l}{2} - h\right)h^2,\ 0 \leq h \leq H_l \tag{4.15}$$

The derivation of the added mass and slamming terms follows the derivation given in [25]. The added mass and slamming terms used for the sphere are shown in Figure 4.2. These have been reconstructed by inspection of Figure 5.2 in [25].

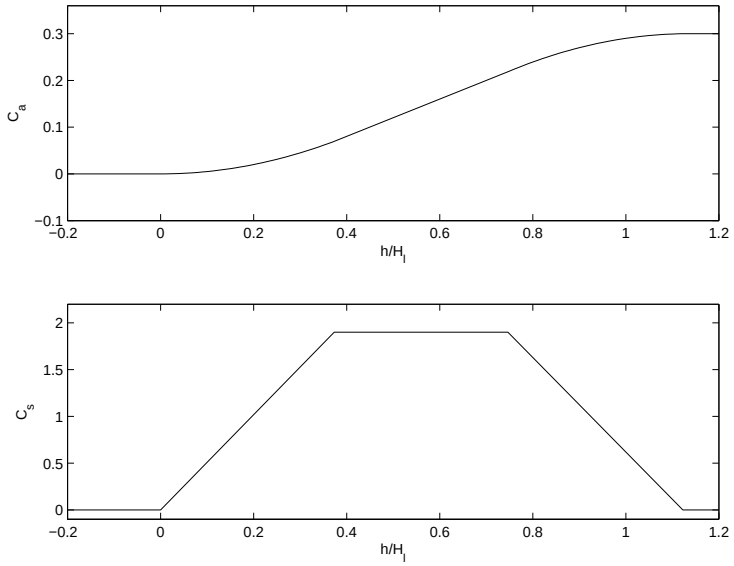

Figure 4.2: Nondimensional added mass term C_a (top) and slamming term C_s for a sphere as function of relative submergence.

The nondimensional added mass is formulated by

$$C_a = \begin{cases} \frac{1}{2}\tilde{h}^2, & 0 \leq \tilde{h} \leq 0.3733 \\ -0.5362\tilde{h}^2 + 1.2187\tilde{h} - 0.3924, & 0.75 \leq \tilde{h} \leq 1.123 \end{cases} \tag{4.16}$$

Linear interpolation is used in the range $0.3733 < \tilde{h} < 1.123$. The nondimensional slamming term is defined by linear interpolation between the points

$$(C_s, h) = \{(0,0), (1.9, 0.3733), (1.9, 0.7467), (0, 1.123)\} \tag{4.17}$$

The dimensional added mass term is given as

$$A_{33} = C_a \rho_w V_l, \tag{4.18}$$

where $V_l = \pi H_l^3/6$ is the volume of the sphere, and the dimensional slamming term is

$$\frac{dA_{33}}{dh} = \frac{1}{2} C_s \rho_w A_l, \tag{4.19}$$

where $A_l = \pi H_l^2/4$ is the projected area of the sphere.

Only nonlinear viscous drag with the value

$$C_D = 0.47 \tag{4.20}$$

is used in [25], and this will thus be done here.

4.4.2 Load geometry: Rectangular box

The derivation of the submerged volume, added mass and slamming terms follows the derivation in [13].

For a rectangular box with length L_l, breadth B_l and height H_l the submerged volume is

$$\Omega(h) = \begin{cases} L_l B_l h, & 0 \leq h < H_l \\ L_l B_l H_l, & h \geq H_l \end{cases} \tag{4.21}$$

and the added mass and slamming terms are

$$A_{33} = \rho_w \Omega(h) = \rho_w L_l B_l h \tag{4.22}$$

$$\frac{dA_{33}}{dh} = \rho_w L_l B_l \tag{4.23}$$

The nondimensional added mass term is thus derived in the following way:

$$A_{33} = C_a \rho_w V_l \tag{4.24}$$

$$\rho_w L_l B_l h = C_a \rho_w L_l B_l H_l \tag{4.25}$$

$$C_a = \frac{h}{H_l} = \tilde{h}, \tag{4.26}$$

i.e.

$$C_a = \begin{cases} \tilde{h}, & 0 \leq \tilde{h} < 1 \\ 1, & \tilde{h} \geq 1 \end{cases} \tag{4.27}$$

and the nondimensional slamming term is found in the same manner:

$$\frac{dA_{33}}{dh} = \frac{1}{2} C_s \rho_w H_l \tag{4.28}$$

$$\rho_w L_l B_l = \frac{1}{2} C_s \rho_w H_l \tag{4.29}$$

$$C_s = 2\frac{L_l B_l}{H_l}, \; 0 \leq \tilde{h} \leq 1 \tag{4.30}$$

i.e.

$$C_s = \begin{cases} 2\frac{L_l B_l}{H_l}, & 0 \leq \tilde{h} \leq 1 \\ 0, & \text{otherwise} \end{cases} \tag{4.31}$$

Only nonlinear viscous drag with the value

$$C_D = 1.2 \tag{4.32}$$

is used in [13], and this will thus be done here.

4.4.3 Hydrodynamic forces on the hoisting cable

The buoyancy due to the submerged cable is

$$F_{c_b} = \rho_w g A_c L_{c_s}, \tag{4.33}$$

where

$$L_{c_s} = \min(0, z_w - z_l) \tag{4.34}$$

is the submerged part of the cable. Since half the mass of the cable is assumed to be rigidly attached to the load, only half the length of the cable may contribute to the load's buoyancy such that the added buoyancy to the load due to the submerged cable is given by

$$F_{c_{b_{load}}} = \rho_w g A_c L_{c_{s_{load}}}, \tag{4.35}$$

where

$$L_{c_{s_{load}}} = \min\left(L_{c_s}, \frac{1}{2} L_c\right) \tag{4.36}$$

The remaining part of the cable buoyancy,

$$F_{c_{b_{boom}}} = \rho_w g A_c L_{c_{s_{boom}}}, \tag{4.37}$$

where

$$L_{c_{s_{boom}}} = L_{c_s} - L_{c_{s_{load}}} \tag{4.38}$$

will be accounted for in the expression for the boom tip force derived in Section 4.7.

For the cable parameters used in this thesis, the buoyancy reduces the weight of the submerged cable with approximately 11% compared to the weight of the cable in air.

Tangential drag on the hoisting cable due to its motion in water was considered in [28] to be insignificant. However, if the model was to account for horizontal effects such as currents, the drag forces would be significant.

4.5 Cable force

The cable effects considered are the spring force, internal damping, force of gravity and inertia. In addition, slack rope is modelled.

The force of gravity is given by

$$F_{c_g} = -\frac{1}{2} \rho_c g L_c, \tag{4.39}$$

where ρ_c is the cable mass per metre. This means that half the cable mass contributes to the force of gravity on the load and the static deflection of the cable. Using half the cable mass is justified in [28]. In a similar manner, the

half the mass is assumed to be rigidly attached to the load and contribute to the load's inertia according to

$$F_{c_i} = -\frac{1}{2}\rho_c L_c \ddot{z}_l \tag{4.40}$$

The spring force derived in [28] is

$$F_{c_s} = \frac{EA_c}{L_c}\Delta L_c, \tag{4.41}$$

where E is the modulus of elasticity/Young's modulus and A_c is the cable's cross sectional area. The internal damping is given by

$$F_{c_d} = d(\dot{z}_b - \dot{z}_l) \tag{4.42}$$

The expression for the damping term d is found as follows: The equation of motion for the lower end of the cable with no external forces is given by

$$F_{c_i} + F_{c_d} + F_{c_s} = 0, \tag{4.43}$$

Inserting the above expressions gives

$$-\frac{1}{2}\rho_c L_c \ddot{z}_l + d(\dot{z}_b - \dot{z}_l) + \frac{EA_c}{L_c}\Delta L_c = 0 \tag{4.44}$$

$$\ddot{z}_l + \frac{2d}{\rho_c L_c} + \frac{2EA_c}{\rho_c L_c^2} = \frac{2}{\rho_c L_c}\left(d\dot{z}_b + \frac{EA_c}{L_c}(z_b - L_c)\right) \tag{4.45}$$

which gives the natural frequency

$$\omega_0 = \frac{1}{L_c}\sqrt{\frac{2EA_c}{\rho_c}}, \tag{4.46}$$

and the damping

$$d = \zeta\rho_c L_c \omega_0 = \zeta\sqrt{2EA_c\rho_c}, \tag{4.47}$$

where $\zeta_c = 0.05$ is the cable's relative damping given in [28].

Slack rope is modelled by multiplying the spring and damper terms according to

$$F_{c_{s,d}} = (F_{c_s} + F_{c_d})g(\Delta L_c), \tag{4.48}$$

where

$$g(\Delta L_c) = \begin{cases} 0 & \Delta L_c \leq 0 \\ 1 & \Delta L_c > 0 \end{cases} \tag{4.49}$$

such that their contributions are zero when the cable elongation is negative.

The resultant force from the cable F_c in Equation (4.2) is now given by

$$F_c = F_{c_g} + F_{c_i} + F_{c_{s,d}} \tag{4.50}$$

4.6 Normal force

In [28] a model for the normal force when landing the payload on a surface was derived from a spring-damper concept. This model required spring and damper parameters to be tuned in order to achieve the desired response, and also the integration method and its step size had to be regarded in order to ensure numerical stability.

Since the magnitude of the normal force is not needed elsewhere in the model, only its effect, simulating load landing may be performed in a simpler manner. The presented model is developed based on ideas from Olve Mo at Marine Cybernetics.

The model works as follows: When $z_l - H_l - z_d < 0$, the load's position, velocity and acceleration is switched to

$$z_l = z_d + H_l \tag{4.51}$$

$$\dot{z}_l = \dot{z}_d \tag{4.52}$$

$$\ddot{z}_l = \ddot{z}_d \tag{4.53}$$

Once the computed load acceleration is greater than the acceleration of the deck, i.e. $\ddot{z}_l > \ddot{z}_d$, the payload integrators are reset with initial conditions in accordance with Equations (4.51) and (4.52), and the output load motion is switched back to the integrators. Figure C.5 shows the block diagram for the payload dynamics and the logic for the switching and resetting the integrators.

This solution requires no configuration, and will be numerically stable.

Since the geometry of e.g. the vessel deck is not included in the model, a logic variable N_{enable} is included in the model. As long as $N_{enable} = 1$, the above normal force concept applies. When $N_{enable} = 0$, on the other hand, the concept does not apply. For example, this may be used when simulating that the load is lifted from the deck into the air and eventually into the water. At the beginning of the simulation, $N_{enable} = 1$ and the load is supported by the deck. When the load is lifted from the deck and suspended by the hoisting cable, N_{enable} is set to zero, and the load may now be lowered into the water.

The model presented in [28], however, may be a good starting point for modeling landing on non-rigid surfaces such as the seabed.

4.7 The boom tip force

The payload and hoisting cable model influences the crane model in Chapter 2 and winch model in Chapter 5 through the boom tip force to be derived in the present section.

The force experienced by the hook is given by the cable spring and damper

terms derived in Section 4.5, i.e.

$$F_{hook} = (F_{c_s} + F_{c_d})g(\Delta L_c), \tag{4.54}$$

If the cable was mass less, the hook force and boom tip force would be equal. This is not the case, however. As stated in Section 4.5, half the mass of the cable is assumed to be rigidly attached to the payload. The remaining half is assumed to be placed at the boom tip. Then the boom tip force is given by the hook force F_{hook}, the buoyancy on the top end of the cable and the gravity and inertia acting on the top end cable mass according to

$$F_{boom} = \frac{1}{2}\rho_c L_c(g + \ddot{z}_b - \ddot{L}_c) - \rho_w A_c L_{c_{s_{boom}}} g + F_{hook}, \tag{4.55}$$

Now, if the cable length was constant, i.e. $\dot{L}_c = \ddot{L}_c = 0$, the mass of the top end of the cable would normally be assumed to be rigidly attached to the boom tip. And, conversely, if the boom tip was standing still, i.e. $\dot{z}_b = \ddot{z}_b = 0$, the mass of the top end of the cable would normally be assumed to be rigidly attached to the winch drum.

However, the force acting on the boom tip will depend on the acceleration of the cable, and, conversely, the force acting on the winch drum will depend on the acceleration of the boom tip. Hence, the top end cable mass cannot be rigidly attached to neither the boom tip nor the winch drum.

The direct implementation of Equation (4.55) as the boom tip force will result in an algebraic loop in the model. By using the boom tip and cable accelerations from the previous time step, the algebraic loop is avoided. Care must be taken when using this solution as it may have unexpected side effects and result in degenerated simulator performance.

The expression of F_{boom} represents the force with which the boom tip and winch drum act on the top end of the cable. Since the payload and hoisting cable model is derived in a reference frame with positive z-axis pointing upwards, the force $\mathbf{f}^n_{boom}$ provided to the crane dynamics model is given by

$$\mathbf{f}^n_{boom} = [0 \quad 0 \quad -F_{boom}]^T \tag{4.56}$$

4.8 Dynamic amplification factor

It is imperative that the forces on the load and cable are kept within limits during the lifting operation. In [29] limits are given in terms of the Dynamic Amplification Factor, referred to as DAF, which is defined as

$$\text{DAF} = \frac{\text{Dynamic load} + \text{static load}}{\text{Static load}} \tag{4.57}$$

$$\tag{4.58}$$

Table 4.1: DAF factors for offshore lifts for a given static hook load range. The numbers are taken from [29].

Static Hook Load	DAF Offshore
$50 - 100$ t	1.30
$100 - 1000$ t	1.20
$1000 - 2500$ t	1.15
> 2500 t	1.10

For offshore lifts the DAF should be below the limits listed in Table 4.1 for the respective hook loads, [29].

When planning operations with the use of simulators, the DAF is a useful parameter to observe as the DAF must be within its limits in order for the operation to be successful. Also, it is useful for verifying simulator correctness.

From the derivations in the previous sections of this chapter, the load's equation of motion is

$$(M_l + \frac{1}{2}\rho_c L_c + A_{33})\ddot{z}_l = \left(\rho_w \left(\Omega(h) + A_c L_{c_{s_{load}}}\right) - M_l - \frac{1}{2}\rho_c L_c\right) g + F_{hook} \tag{4.59}$$
$$+ \frac{dA_{33}}{dh} f_{slam}(w, \dot{z}_l) + A_{33}\dot{w} + \rho_w \Omega(h) f_{FK}(\dot{w}, \dot{z}_l) + F_{h_d}$$

In order to find the static hook force, velocities and accelerations are set to zero in Equation (4.59) yielding

$$0 = \left(\rho_w \left(\Omega(h) + A_c L_{c_{s_{load}}}\right) - M_l - \frac{1}{2}\rho_c L_c\right) g + F_{hook,static} \tag{4.60}$$

The static hook force is the found to be

$$F_{hook,static} = \left(M_l + \frac{1}{2}\rho_c L_c - \rho_w \left(\Omega(h) + A_c L_{c_{s_{load}}}\right)\right) g, \tag{4.61}$$

and the DAF at the hook is thus given by

$$\text{DAF}_{\text{hook}} = \frac{F_{hook}}{F_{hook,static}}, \tag{4.62}$$

$$\tag{4.63}$$

where F_{hook} is given by Equation (4.54).

The static boom tip force is given by the gravity and buoyancy on the top end of the cable in addition to the static hook force:

$$F_{boom,static} = F_{hook,static} + \left(\frac{1}{2}\rho_c L_c - \rho_w A_c L_{c_{s_{boom}}}\right) g \tag{4.64}$$
$$= \left(M_l + \rho_c L_c - \rho_w \left(\Omega(h) + A_c L_{c_s}\right)\right) g \tag{4.65}$$

Table 4.2: Cable parameters for the two cable sizes used in the simulations. MBL denotes the minimum braking load.

Parameter	Cable 1	Cable 2
D_c	0.022 m	0.042 m
A_c	$228 \cdot 10^{-6}$ m^2	$831 \cdot 10^{-6}$ m^2
ρ_c	2.11 kg/m	7.65 kg/m
E	74 GPa	74 GPa
MBL	186 kN	1.28 MN

$$\text{DAF}_{\text{boom}} = \frac{F_{boom}}{F_{boom,static}}, \tag{4.66}$$

where F_{boom} is given by Equation (4.55).

4.9 Model parameters

The required payload parameters are the mass M_l, height H_l, length L_l, and breadth B_l, and the hydrodynamic coefficients added mass A_{33}, slamming $\frac{dA_{33}}{dh}$, volume of the submerged load $\Omega(h)$ and the linear and quadratic damping coefficients, respectively. If the sphere geometry is used, the payload breadth and length need not be defined.

By stating the type of geometry, payload mass, and height, length and breadth, the hydrodynamic parameters will be defined as shown in Sections 4.4.1 and 4.4.2 for the respective geometry.

The required cable parameters are the cross sectional area A_c, the modulus of elasticity E, and the cable density ρ_c. Another useful parameter is the minimum braking load, which states the maximum tension level the cable is guaranteed to withstand without braking. Also, the cable diameter is required in the winch model, and will be stated here with all other cable parameters. Cable data is for two cable sizes of the ScanRope ScanLift Multistrand 35×7 non-rotating ropes given in [22] is used in the simulations. The data for the two cables is given in Table 4.2.

The load geometry and size, and which cable is used, will be stated for each simulation case in Chapter 7.

4.10 Initialisation

The cable and payload model requires initial values for the position and velocity of the load. When the load is initially suspended in the cable, the initial position

is determined from the equation of motion of the load

$$\begin{aligned}&(M_l + \frac{1}{2}\rho_c L_c + A_{33})\ddot{z}_l \\ &= \left(\rho_w \left(\Omega(h) + A_c L_{c_{s_{load}}}\right) - M_l - \frac{1}{2}\rho_c L_c\right) g + \frac{EA_c}{L_c}\Delta L_c + d(\dot{z}_b - \dot{z}_l) \\ &+ \frac{dA_{33}}{dh} f_{slam}(w, \dot{z}_l) + A_{33}\dot{w} + \rho_w \Omega(h) f_{FK}(\dot{w}, \dot{z}_l) + F_{h_d}\end{aligned} \tag{4.67}$$

Setting accelerations and velocities to zero reduces the equation to

$$0 = \left(\rho_w \left(\Omega(h) + A_c L_{c_{s_{load}}}\right) - M_l - \frac{1}{2}\rho_c L_c\right) g + \frac{EA_c}{L_c}\Delta L_c \tag{4.68}$$

By the use of the relation $\Delta L_c = z_b - z_l - L_c$ from Equation (4.3), the initial position is given by

$$z_{l_0} = \frac{L_c}{EA_c}\left(\rho_w \left(\Omega(h) + A_c L_{c_{s_{load}}}\right) - M_l - \frac{1}{2}\rho_c L_c\right) g + z_b - L_c \tag{4.69}$$

To simplify the above expression, it is tested whether $z_b - L_c - H_l > 0$ or not. If the expression is true, the payload is in the air, and the terms $\Omega(h)$ are $L_{c_{s_{load}}}$ zero. If the expression is false, on the other hand, it is assumed that the load is fully submerged, such that

$$\Omega(h) = V_l, \text{ and} \tag{4.70}$$

$$L_{c_{s_{load}}} = \frac{1}{2}L_c \tag{4.71}$$

Assuming that the cable has a zero initial velocity, i.e. $\dot{L}_{c_0} = 0$, setting

$$\dot{z}_{b_0} = \dot{z}_b \tag{4.72}$$

is a plausible choice for the initial velocity.

When the load is initially resting on a deck, on the other hand, the initial position and velocity is

$$z_{l_0} = z_d + H_l \tag{4.73}$$

$$\dot{z}_{l_0} = \dot{z}_d \tag{4.74}$$

Which set of initial values to be used is determined as follows: When the initial position based on the suspended load approach is determined, it is checked if $z_{l_0} - H_l - z_d < 0$ and if the normal force model is enabled, i.e. $N_{enable} = 1$. If both are true, the initial values of Equations (4.73) and (4.74) are used. If not, the initial values of Equations (4.69) and (4.72) are used.

Chapter 5

Winch and drive system

5.1 Introduction

A short review of crane drive systems is given in [14]. The listed drive systems are direct electric, electro-hydraulic, diesel, diesel-hydraulic, and hydraulic ring-line, where the most common drive system on medium and large installations is the electro-hydraulic. The electro-hydraulic drive system consists of electric motors driving one or more hydraulic power units which in turn power a hydraulic motor. One of the main advantages of hydraulic motors is, according to [18], the high torque-to-inertia ratio. Models for hydraulic winch systems for offshore cranes may be found in [31].

[14] also states that medium or high voltage direct electric drives may be considered for large cranes. The advantages of electric drives are, according to [14], high reliability and low maintenance and noise levels. Lifetime costs may be lower for direct electric drives compared to electro-hydraulic even though it has higher initial costs.

Due to its simplicity with regard to modelling and configuration, a direct electric drive system will be modelled in this thesis. The drive model may be replaced with e.g. an electro-hydraulic drive from [31] at a later stage.

The drive is assumed to consist of an AC motor powered by an inverter. The motor may be run in all four quadrants; when the output motor power is negative, it is assumed to be working as a generator/brake. It is assumed that there are no dynamics from the electric torque supplied from the rectifier to the mechanical torque output by the motor. The commanded torque from the rectifier is given by a PI speed controller with anti wind-up, and the commanded torque has dynamic limits. A disc brake model is also included.

The motor is assumed to be rigidly connected to the winch drum by a reduction gear, and the winch drum inertia varies with the amount of cable on the

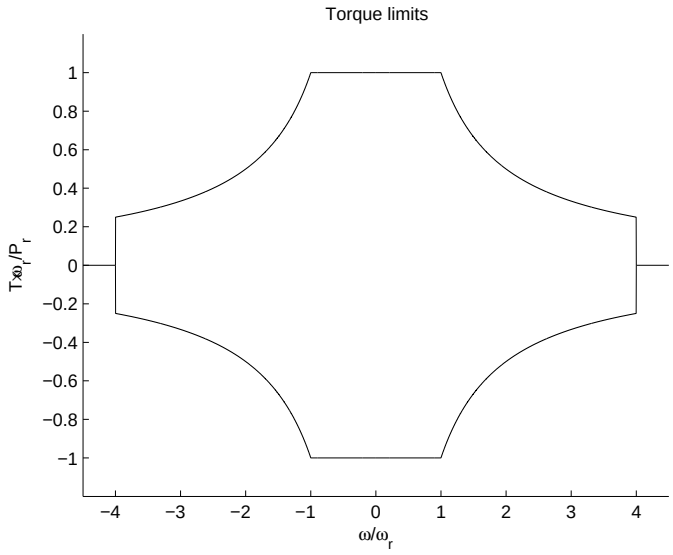

Figure 5.1: Illustration of torque limits.

drum.

[10] gives a comprehensive review of the modelling of electric motors and gears, and related material, and is to some extent used during this chapter.

5.2 Motor model with torque limits

According to [19], the equation of motion for an AC motor powered by an inverter is given by

$$J_m\dot{\omega}_m = -D_m\omega_m + T - T_L \tag{5.1}$$

$$\dot{\theta}_m = \omega_m \tag{5.2}$$

where T is the motor torque, T_L is the external torque from the load and D_m is a viscous friction coefficient for the motor and shaft. It is assumed that there are no dynamics from the commanded torque from the rectifier to the output torque T imposed on the motor. The output torque from the rectifier is limited in order to avoid overload on the AC motor. According to [19], the torque limits may be defined by the two quantities rated power P_r and rated speed ω_r. They denote the maximum power and speed that the motor can sustain indefinitely,

respectively, and the limits are given by

$$T_{lim} = \begin{cases} \min\left(\frac{P_r}{\omega_r}, \frac{P_r}{\omega_m}\right) & |\omega_m| \leq \omega_{r_m} \\ 0 & |\omega_m| > \omega_{r_m} \end{cases} \tag{5.3}$$

$$= \begin{cases} \frac{P_r}{\max(\omega_r, \omega_m)} & |\omega_m| \leq \omega_{r_m} \\ 0 & |\omega_m| > \omega_{r_m} \end{cases} \tag{5.4}$$

such that the torque T in Equation (5.1) will be limited by

$$-T_{lim} \leq T \leq T_{lim} \tag{5.5}$$

An illustration of the motor speed vs. torque function is provided in Figure 5.1.

5.3 Connecting a winch to the motor

The motor and winch are rigidly connected by a reduction gear such that the winch shaft speed ω_w and angle θ_w are given by

$$\omega_w = n\omega_m \tag{5.6}$$

$$\theta_w = n\theta_m \tag{5.7}$$

$$n \in (0, 1] \tag{5.8}$$

Given the winch inertia, J_w, the kinetic energy of the motor-winch system is given by

$$E_k = \frac{1}{2}(J_m\omega_m^2 + J_w\omega_w^2) \tag{5.9}$$

The total inertia referred to the motor side, J_{tot}, may be found by combining Equations (5.6) and (5.9)

$$E_k = \frac{1}{2}(J_m\omega_m^2 + J_w n^2\omega_m^2) = \frac{1}{2}(J_m + n^2 J_w)\omega_m^2 \tag{5.10}$$

i.e.

$$J_{tot} = J_m + n^2 J_w \tag{5.11}$$

The torque T_e acting on the winch seen from the motor shaft T_L may be found as follows:

$$T_L\omega_m = T_e\omega_w \tag{5.12}$$

$$T_L = \frac{\omega_w}{\omega_m}T_e = nT_e \tag{5.13}$$

By the same rationale, viscous friction on the winch seen from the motor side is

$$nD_w\omega_m \tag{5.14}$$

Seen from the motor the model is now represented by

$$J_{tot}\dot{\omega}_m = -D_{tot}\omega_m + T - nT_e, \tag{5.15}$$

where the total viscous friction coefficient is

$$D_{tot} = D_m + nD_w \tag{5.16}$$

5.4 Winch inertia

The winch drum inertia J_w is given by the inertia of the winch drum itself, J_d, and the inertia due to the cable wound onto it, J_c, according to

$$J_w = J_d + J_c \tag{5.17}$$

An estimate for the winch drum mass M_d and the drum inertia J_d may be found by the procedure in Appendix A.1 by assuming a mass density ρ, and that the mass is homogeneously distributed in a cylindrical annulus with inner radius R_{d_i}, outer radius R_d, and width W_d according to

$$M_d = \rho\pi\left(R_d^2 - R_{d_i}^2\right)W_d \tag{5.18}$$

and

$$J_d = \frac{1}{2}M_d\left(R_d^2 + R_{d_i}^2\right) \tag{5.19}$$

Accordingly, the winch inertia due to the cable on the drum J_c is given by the mass of the cable wound onto the winch drum, the winch drum radius, the distance from the drum centre to the outermost cable layer R_c and winch drum width according to

$$J_c = \frac{1}{2}M_{c_d}\left(R_c^2 + R_d^2\right) \tag{5.20}$$

The expression for R_c is given in Section 5.5, and the mass of the cable wound onto the winch drum is given by

$$M_{c_d} = \rho_c L(\theta_\omega), \tag{5.21}$$

where ρ_c is the cable mass per metre and $L(\theta_\omega)$ denotes the length of the cable on the drum, expressed in Section 5.5.

5.5 Length of cable on the winch drum

The length of the cable on the winch drum is given in [31] by

$$L(\theta_w) = 2\pi nN_F R_d n + n(n-1)N_F\pi d_c + (\theta_w - 2\pi nN_F)(R_d + nd_c), \tag{5.22}$$

where $N_F = \lfloor \frac{W_d}{d_c} \rfloor$ is the number of cable turns per layer, d_c is the hoisting cable diameter, R_d is the winch drum radius and $n = \left\lfloor \frac{\theta_w}{2\pi N_F} \right\rfloor$ is the number of fully wound layers of cable. If the total length of hoisting cable is L_{tot}, and the length of cable along the crane structure is L_{crane}, then the length of cable from the boom tip to the load L_c is given by

$$L_c = L_{tot} - L_{crane} - L(\theta_\omega) \tag{5.23}$$

The cable radius, i.e. the distance from the winch drum centre to the outermost cable layer is given by

$$R_c = R_d + d_c n \tag{5.24}$$

However, if the flooring function is removed from n, i.e. expressing R_c by

$$R_c = R_d + d_c \frac{\theta_w}{2\pi N_F}, \tag{5.25}$$

the moment of inertia from the cable on the winch drum will be continuous.

5.6 Boom tip force to torque

The external torque T_e may now be expressed in terms of the boom tip force F_{boom} and the cable radius according to

$$T_e = R_c F_{boom} \tag{5.26}$$

5.7 Disc brake

The disc brake is enabled by a flag. When it is enabled, the brake puts up a constant torque in the opposite direction to the motor speed direction. At the instant when the motor speed switches sign, the motor speed integrator is reset to zero, and the applied torque from the brake is equal to but with opposite sign to the sum of all other torque contributions (e.g. rectifier and load). This implies that the brake can hold an arbitrary load torque, which obviously is not realistic. However, it is assumed that the brake is made strong enough to hold any realistic load. The brake is applied until the flag no longer enables the brake. The disc brake block diagram is found in Figure C.7.

5.8 Speed controller

The commanded torque T_c from the PI controller with anti wind-up is given by

$$T_c = k_p(\omega_m - \omega_d) + \int \left(k_i(\omega_m - \omega_d) + k_{lim}(T_c - T)\right) d\tau \tag{5.27}$$

where

$$T = \begin{cases} \min(T_c, T_{lim}), & T_c > 0 \\ \max(T_c, -T_{lim}), & T_c < 0, \end{cases} \tag{5.28}$$

and $k_{lim}(T_c - T)$ is the anti wind-up term, and ω_d is the desired motor speed, and k_p and k_i are the proportional and integral gains, respectively, and k_{lim} is the anti wind-up feedback gain. The output torque from the rectifier is give by T. The block diagram representation is given in Figure C.8. The anti wind-up scheme is taken from [21].

The controller is enabled when the disc brake is disabled. When the controller is enabled, the integrator in the controller is supplied with the initial condition

$$T_{i0} = -T_L, \tag{5.29}$$

i.e. the motor is torqued up such that it can hold the load suspended in the cable.

5.8.1 Controller gains

Inserting the control law (5.27) into Equation (5.15), assuming that the anti-windup is inactive, yields

$$J_{tot}\dot{\omega}_m = -D_{tot}\omega_m - k_p(\omega_m - \omega_d) - k_i \int (\omega_m - \omega_d)d\tau - nT_e \tag{5.30}$$

By Laplace transformation the equation becomes

$$J_{tot}\omega_m s = -D_{tot}\omega_m - k_p(\omega_m - \omega_d) - k_i \frac{1}{s}(\omega_m - \omega_d) - nT_e, \tag{5.31}$$

which is rewritten to

$$(J_{tot}s^2 + (k_p + D_{tot})s + k_i)\omega_m = (k_p s + k_i)\omega_d - nT_e \tag{5.32}$$

The transfer function from desired motor speed to motor speed is then given by

$$\frac{\omega_m}{\omega_d}(s) = \frac{k_p s + k_i}{J_{tot}s^2 + (k_p + D_{tot})s + k_i} = \frac{\frac{k_p}{J_{tot}}s + \frac{k_i}{J_{tot}}}{s^2 + \frac{k_p + D_{tot}}{J_{tot}}s + \frac{k_i}{J_{tot}}} \tag{5.33}$$

Equation (5.33) may be written in standard form (i.e. in terms of the relative damping ζ and the undamped natural frequency ω_0) as

$$\frac{\omega_m}{\omega_d}(s) = \frac{\frac{k_p}{J_{tot}}s + \omega_0^2}{s^2 + 2\zeta\omega_0 s + \omega_0^2} \tag{5.34}$$

The controller should yield a critically damped response, i.e. $\zeta = 1$. Now, the integral gain k_i is found by

$$k_i = J_{tot}\omega_0^2 \tag{5.35}$$

and the proportional gain is

$$\frac{k_p + D_{tot}}{J_{tot}} = 2\omega_0 \Rightarrow k_p = 2J_{tot}\omega_0 - D_{tot} \tag{5.36}$$

By deciding on ω_0, the controller gains are determined.

The controller gains depend on variable parameters, e.g. the total moment of inertia J_{tot}. Using the exact values is done due to simplicity. Using approximate values, however, will still result in a stable controller.

5.9 Model parameters

The crane should be able to lift a mass of $M = 100$ t at a speed $v = 2.5$ m/s. This requires the power

$$P = Mgv \tag{5.37}$$

where g is the acceleration of gravity. Assuming a dimensioning factor of 1.5 the rated power is

$$P_r = 1.5P \approx 3.7 \text{ MW} \tag{5.38}$$

According to [19], the rated speed is given by the maximum voltage frequency delivered by the inverter divided by the number of pole pairs. Usually, the frequency is either 50 Hz or 60 Hz. Assuming that the maximum frequency is 50 Hz, and the motor has four pole pairs, the rated speed is

$$\omega_r = 2\pi\frac{50}{4} \text{ rad/s} = 25\pi \text{ rad/s} \tag{5.39}$$

By the relation between the rated speed and the rated hoisting speed v

$$\omega_r = \frac{vR_c}{n}, \tag{5.40}$$

the gear ratio is given by

$$n = \frac{vR_c}{\omega_r} \tag{5.41}$$

The cable radius R_c, however, will vary with the amount of cable wound onto the winch drum. Using the winch drum radius R_d instead of R_c, and assuming that the winch drum radius is

$$R_d = 0.6 \text{ m}, \tag{5.42}$$

gear ratio is

$$n = \frac{vR_d}{\omega_r} \approx 0.019 \tag{5.43}$$

The maximum motor speed is for simplicity set to $\omega_{r_m} = 1.5\omega_r$.

The motor inertia is found as follows: Accelerating the motor without load by the constant torque $T_r = P_r/\omega_r$ corresponds to the equation

$$J_m\dot{\omega}_m = T_r \tag{5.44}$$

According to Equation (5.3), as long as $\omega_m < \omega_r$, the rated torque T_r is constant. The solution of Equation (5.44) is

$$\omega_m(t) = \omega_m(0) + \frac{T_r}{J_m}t \tag{5.45}$$

Assuming that the motor is accelerated from zero speed to rated speed in t seconds, Equation (5.45) gives the expression

$$J_m = \frac{T_r}{\omega_r}t = \frac{P_r}{\omega_r^2}t \tag{5.46}$$

According to [19], this acceleration usually takes between one and two seconds. Assuming $t = 1.5$ s gives the motor inertia

$$J_m \approx 895 \text{ kg m}^2 \tag{5.47}$$

Friction in the motor is assumed to be viscous, and is found by assuming that the power loss at rated speed is 10 % of rated power, i.e.

$$D_m\omega_r^2 = 0.1P_r \tag{5.48}$$

which gives the damping coefficient

$$D_m = \frac{0.1P_r}{\omega_r^2} \approx 60 \text{ kgm/srad}, \tag{5.49}$$

For simplicity, friction in the winch drum is disregarded, and, hence, the total viscous damping coefficient is

$$D_{tot} = D_m \tag{5.50}$$

The mass of the winch drum is found by assuming that the drum may be represented by a cylindrical annulus which is 0.06 m thick and $W_d = 1.8$ m wide with the mass density $\rho = 7800 \text{ kg/m}^3$ of steel. By Equation (5.18) the mass M_d of the drum is then

$$M_d \approx 3.0 \text{ t}, \tag{5.51}$$

and by Equation (5.19) the drum inertia is

$$J_d \approx 983 \text{ kg m}^2 \tag{5.52}$$

Assuming that the winch is positioned on top of the crane in accordance with Figure 2.1, the amount of cable along the crane structure, is approximated by the sum of the length of the knuckle and knuckle jib booms, i.e.

$$L_{crane} = a_2 + a_3 = 33.8 \text{ m} \tag{5.53}$$

The total length of hoisting cable is set to

$$L_{tot} = 1500 \text{ m}, \tag{5.54}$$

By simulations the speed controller parameter

$$\omega_0 = 12.5 \text{ rad/s} \tag{5.55}$$

is chosen.

The disc brake torque 200 kN m is chosen.

5.10 Initialisation

The winch and drive system model requires initial values for the winch motor angle and winch motor speed. Since the cable length on the winch drum is given directly by the angle, the winch angle must reflect this.

Given the initial length of cable wound onto the winch drum, L_{init}, Equation (5.22) may be used to find the initial winch drum angle by the built-in Matlab function `fzero`, where the function required by `fzero` is

$$2\pi n N_F R_d n + n(n-1)N_F \pi d_c + (\theta_w - 2\pi n N_F)(R_d + n d_c) - L_{init} = 0, \tag{5.56}$$

where

$$n = \left\lfloor \frac{\theta_w}{2\pi N_F} \right\rfloor \tag{5.57}$$

Given the initial winch drum angle $\omega_{w_{init}}$, the initial motor angle is

$$\omega_{m_{init}} = \frac{1}{n}\omega_{w_{init}}, \tag{5.58}$$

where n denotes the gear ratio.

The initial motor speed is set to zero.

Chapter 6

Speed controller references

6.1 Introduction

The reference to the speed controller is given by the direct speed command, and the HC and CT modes, and are superposed such that the desired speed is given by

$$\omega_d = Speed_d + HC_d + CT_d, \tag{6.1}$$

where $Speed_d$ may be viewed as the speed commanded from the crane operator's controls, and HC_d and CT_d are the speed commands provided by the automatic HC and CT systems, respectively. For example, while operating in HC mode, the contribution from HC_d attenuates the vessel motion otherwise induced on the load, whereas a non-zero speed reference from $Speed_d$ hoists of lowers the payload. Another example is when using CT mode, and there is a relative motion between the boom tip and the payload. Then HC_d will keep the cable slack constant, while CT_d provides the offset speed to pull in the slack and tighten the cable. Using the CT mode with a command from $Speed_d$ does not make sense. Therefore, logic is included to avoid that it happens.

The HC and CT modes are bumplessly enabled and disabled by a smoothed step. Also, the desired speed $Speed_d$ is a smooth reference signal.

6.2 Heave compensation control

A review of different heave compensation and various heave compensation concepts may be found in [27] and [20]. The concept chosen here is the so-called direct winch drive.

The purpose of the heave compensation mode is to remove the influence of the boom tip motion on the payload. The immediate suggestion to achieve this

is by running the winch motor in counter phase with the boom tip velocity, such that

$$\dot{L}_c = \dot{z}_b \tag{6.2}$$

Note that when the cable is payed out $\dot{L}_c > 0$ and $\omega_w < 0$. The rate with which the cable is payed out with is given by the winch speed as

$$\dot{L}_c = -R_c\omega_w \tag{6.3}$$

By the gear ratio n, $\dot{L}_c$ is given by the motor speed ω_m as

$$\dot{L}_c = -R_c n\omega_m \tag{6.4}$$

By substituting Equation (6.2) into Equation (6.4), the required motor speed is given by

$$\omega_m = -\frac{\dot{z}_b}{R_c n}, \tag{6.5}$$

Assuming that the boom tip motion is measured, the commanded speed from the HC mode is

$$HC_d = -\frac{\dot{z}_b}{R_c n} \tag{6.6}$$

6.3 Constant tension control

The purpose of the constant tension is to keep the tension in the cable at a desired level. This mode is usually used to pull in slack in the cable when the load is resting on a surface, such as the vessel deck or the seabed, and may be active until the load is lifted from the surface.

Because of the integral action in the speed controller, a proportional controller from the desired boom force to the commanded speed is considered to be sufficient, such that the command from the CT mode may be expressed by

$$CT_d = K_{CT}(F_d - F_{boom}), \tag{6.7}$$

where F_d is the desired cable tension, and the controller gain K_{CT} is to be determined.

For convenience, the winch and motor model with controller is restated from Equation (5.30) as

$$J_{tot}\dot{\omega}_m = -D_{tot}\omega_m - k_p(\omega_m - \omega_d) - k_i\int(\omega_m - \omega_d)d\tau - nT_e \tag{6.8}$$

where the external torque from Equation (5.26) is

$$T_e = R_c F_{boom}, \tag{6.9}$$

The transfer function from F_{boom} to ω_d is found by reduction of block diagrams to be

$$H(s) = \frac{F_{boom}}{\omega_d}(s) = \frac{K_g K_s \left(\left(2\omega_0 - \frac{D_{tot}}{J_{tot}}\right) s + \omega_0^2\right)}{s\left(s^2 + 2\omega_0 s + \frac{K_g^2 K_s}{J_{tot}} + \omega_0^2\right)}, \tag{6.10}$$

where

$$K_g = nR_c, \text{ and} \tag{6.11}$$

$$K_s = \frac{EA_c}{L_c} \tag{6.12}$$

The deviation between the desired and actual cable tension force may be defined as

$$e = F_d - F_{boom} \tag{6.13}$$

Assuming that the desired motor speed is given by the command from the constant tension mode, i.e. $\omega_d = CT_d$, ω_d is given by substituting the expression in Equation (6.13) into Equation (6.7) as

$$\omega_d = K_{CT} e \tag{6.14}$$

By substituting Equation (6.14) into Equation (6.10), the open loop transfer function for the system is given by

$$\frac{F_{boom}}{e} = K_{CT} H(s) = K_{CT} \frac{K_g K_s \left(\left(2\omega_0 - \frac{D_{tot}}{J_{tot}}\right) s + \omega_0^2\right)}{s\left(s^2 + 2\omega_0 s + \frac{K_g^2 K_s}{J_{tot}} + \omega_0^2\right)} \tag{6.15}$$

By defining

$$K_{CT} = \frac{k_{CT}}{K_g K_s}, \tag{6.16}$$

the open loop gain may be set by choosing a suitable value for k_{CT}. By simulations the value

$$k_{CT} = 30 \tag{6.17}$$

is chosen.

A similar concept is found in [26], where parallel force/position control is tested during water entry.

Chapter 7

Simulator evaluation

7.1 Introduction

The simulator is implemented in the Matlab/Simulink environment, and is evaluated by testing each of the modules separately, and successively joining two or more modules in order to test module interactions before joining all modules into the complete simulator. Finally, the simulator is connected to a vessel model, and the vessel-crane interface is tested.

The payload and hoisting cable model is extensively tested in [28], and the present implementation of this model is an improvement and extension of the implemented software used there. Hence, this model will not be thoroughly tested here. In [28], the simulations crashed when the load was lowered into the water. The presented simulations in this thesis shows that this problem is solved. Also, since a new model is implemented for landing a load onto and lifting it from a deck, this feature will be validated through the simulations.

The chapter ends with stating some properties for the crane simulator.

7.2 Crane structure

The crane dynamics model is tested by running the model with various initial values and verifying the model response. The presence of gravity and joint friction shall make the model converge to a stated equilibrium point.

Two different sets of initial values are used. In both simulations a constant load force of 1 MN acts on the boom tip, and the force is aligned with the acceleration of gravity. The simulations will also indicate whether the implementation of the end-effector force is correct or not.

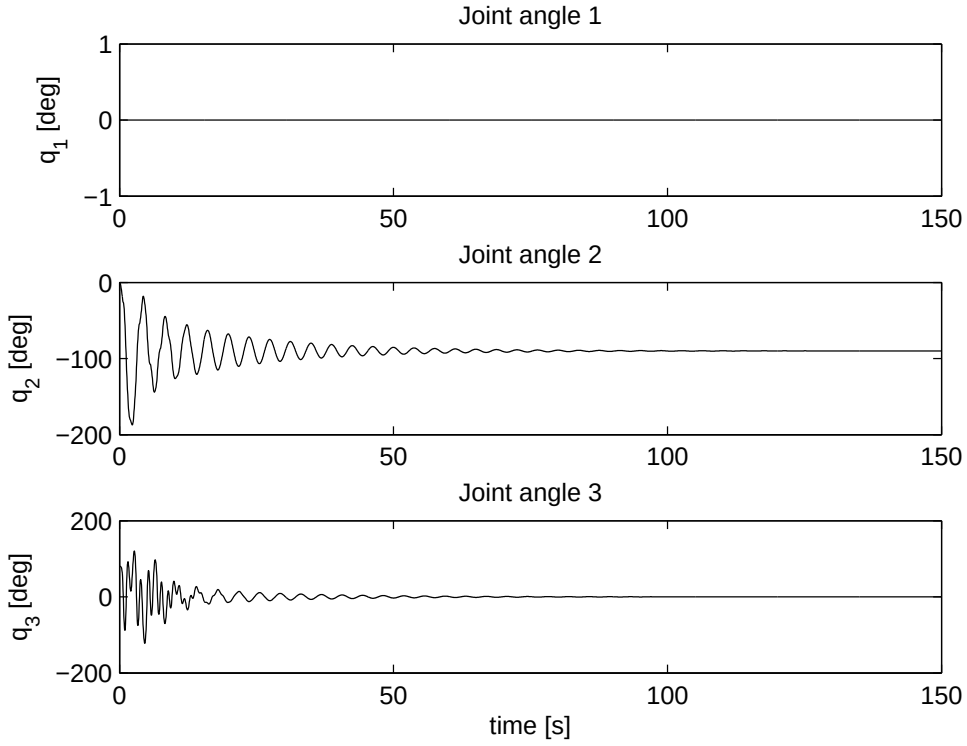

Figure 7.1: Crane structure test, Case 1: Course of the joint angles.

Case 1:
Initial values: $\mathbf{q}(0) = [0° \quad 0° \quad 80°]^T$.
Expected results: Convergence to $\mathbf{q} = [0° \quad -90° \quad 0°]^T$.

Case 2:
Initial values: $\mathbf{q}(0) = [0° \quad -80° \quad 10°]^T$ and roll angle ϕ =45°.
Expected results: Convergence to $\mathbf{q} = [-90° \quad -45° \quad 0°]^T$.

7.2.1 Case 1

The course of the three crane joint angles of Case 1 are shown in Figure 7.1. All joints converge to the expected values, and Joint 1 is unaffected by the motion of the two other links. Figure 7.2 shows the first ten seconds of the simulation. The bottom plot shows the angle between Link 3 and the horizontal, which should converge to $-90°$. Due to the viscous joint friction, the mechanical energy in the system should be monotonically decreasing. Comparing the top and bottom

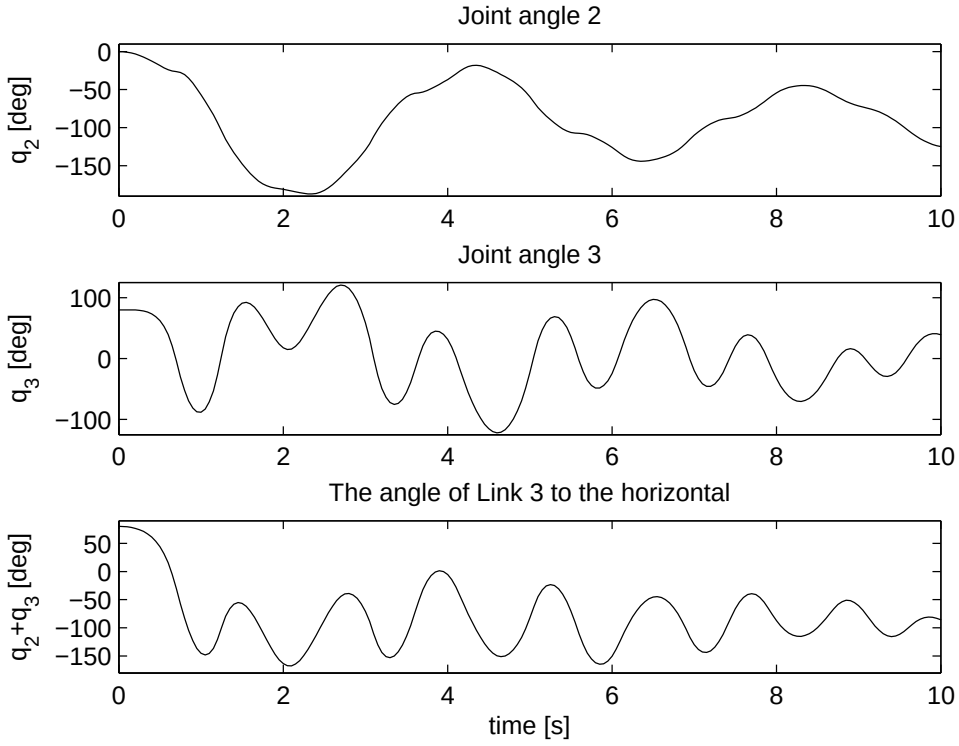

Figure 7.2: Crane structure test, Case 1: Initial course of the joint angles.

plots in Figure 7.2, indicates that this is the case.

7.2.2 Case 2

The course of the three crane joint angles of Case 2 are shown in Figure 7.3, and the figure shows that the angles converge as expected. The convergence of q_1 is slow compared to the other two joint angles. The reason for this is that the mass swinging with q_1 is given by the masses of all the crane links, and is thus considerably larger relative to the friction coefficient of Joint 1 than e.g. the swinging mass of Joint 3 relative to its friction coefficient.

7.3 Crane with hydraulics

In this section the crane model and the hydraulics model are joined in order to test the hydraulics model. Since the hydraulics model does not contain any equation of motion, there is little point in testing it separately.

The model is validated by five test cases. The two first cases validate that the limited piston travel functionality is correctly implemented for both cylinders. The boom tip force is zero during these tests. The two next cases test how heavy

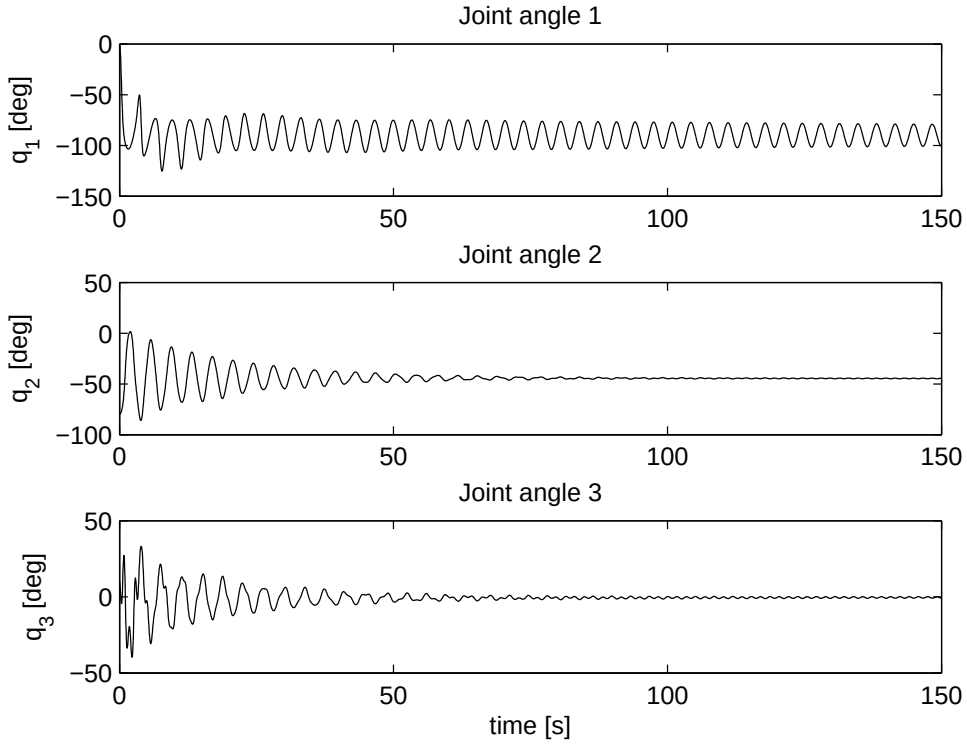

Figure 7.3: Crane structure test, Case 2: Course of the joint angles.

the crane can be loaded. The simulations of the first four test cases are performed with no leakage in the cylinder. The last test case repeats the first case but with leakage in both cylinders.

Case 1:
Why/How: Validate the limited piston travel functionality for the cylinder of Joint 2 by running the cylinder with fully open valve both ways until the piston limit is reached.
Expected results: The piston motion stops at the limits, and the logic related to stopping the piston motion allows for commanding the piston in the opposite direction.

Case 2:
Why/How: Validate the limited piston travel functionality for the cylinder of Joint 3 by running the cylinder with fully open valve to both limits.
Expected results: The piston motion stops at the limits, and the logic related to stopping the piston motion allows for commanding the piston in the opposite direction.

Case 3:
Why/How: Determine how much the crane can be loaded when the joint angles are around $\mathbf{q} = [0 \quad 50 \quad -140]^{T\circ}$ by increasing the boom tip force at a rate of 5 t/s until one of the cylinder pressures reaches the supply pressure level.
Expected results: The pressure of Volume 1 of the cylinder of Joint 2 reaches the pressure limit when the load is substantially larger than safe working load.

Case 4:
Why/How: Determine how much the crane can be loaded when the joint angles are around $\mathbf{q} = [0 \quad 10 \quad -25]^{T\circ}$ by increasing the boom tip force at a rate of 5 t/s until one of the cylinder pressures reaches the supply pressure level.
Expected results: One of the cylinders will reach the supply pressure level at a lower load force level than in Case 3.
Case 5:
Why/How: Repeat Case 1 with a 25 t payload and leakage in the cylinder to verify that the model works with leakage.
Expected results: The payload will creep, and the pressure will stabilise faster than in simulations without leakage.

7.3.1 Case 1

Plots from the simulation of Case 1 are shown in Figures 7.4 and 7.5. At around 5 s the valve is opened with maximum positive spool position, and the piston moves outwards lifting the boom. Nearly twelve seconds into the simulation, the piston reaches the upper limit, and the valve position is automatically decreased to zero which stops the piston motion.

At around 20 s, the valve spool is commanded to a maximum negative position, and the piston moves inwards lowering the boom. This shows that it is possible to command the spool in the opposite direction when the piston is on the upper limit.

After nearly 47 s, the piston reaches the lower limit, and the valve position is automatically increased to zero stopping the piston motion.

At around 58 s, the valve spool is commanded to a positive position, and the piston again moves outwards and lifting the boom. This shows that it is possible to command the spool in the opposite direction when the piston is on the lower limit.

The bottom plot in Figure 7.4 shows that the piston of Joint 3 is slightly affected by the motion of Joint 2. The motion is in the order of a few millimetres, which seems plausible.

The cylinder pressures are shown for both cylinders in Figure 7.5. The figure shows that when the piston reaches the upper limit large variations in the pressure

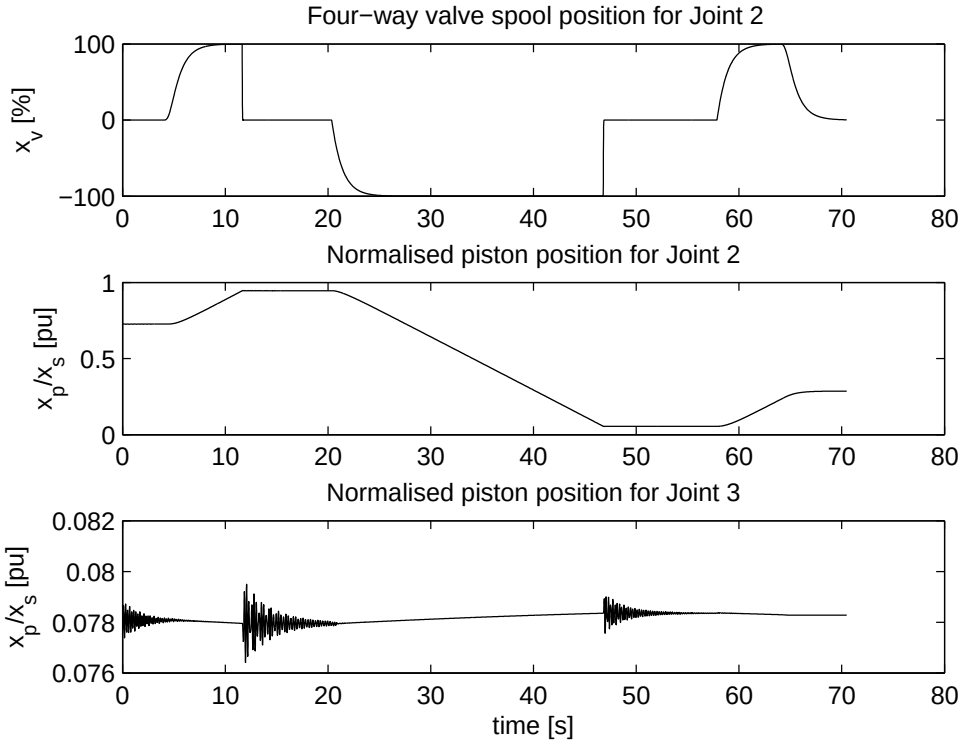

Figure 7.4: Crane and hydraulics test, Case 1: Cylinder piston motions during testing the limited piston travel functionality of Joint 2.

of Volume 2 of the cylinder of Joint 2 arise, and at the lower limit large variations in the pressure of Volume 1 of the cylinder of Joint 2 arise. These cylinder volumes must provide a sufficient pressure level in order to stop the piston and boom in the respective directions. Whit the only damping in the model being the viscous friction of the cylinder piston, and no leakage, these results would be expected.

7.3.2 Case 2

Plots from the simulation of Case 2 are shown in Figures 7.6 and 7.7. The results are analogous to the results of Case 1.

7.3.3 Case 3

Plots from the simulation of Case 3 are shown in Figures 7.8 and 7.9. Figure 7.8 shows that the pressure of Volume 1 of the cylinder of Joint 2 reaches the supply pressure after approximately 35 s, at which the load force is about 1.6 MN. This corresponds to a load in the field of gravity with a mass of 163 t, which is significantly more than the stated safe working load of 100 t. Figure 7.9 shows

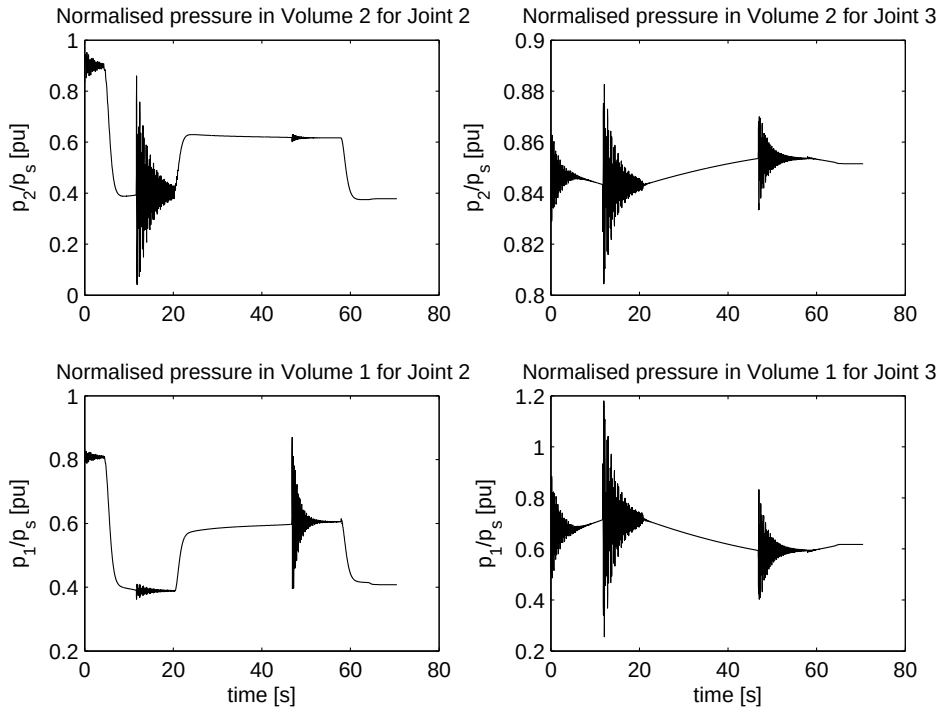

Figure 7.5: Crane and hydraulics test, Case 1: Progress of cylinder pressures during the testing of the limited piston travel functionality of Joint 2.

that the joint angles q_2 and q_3 are nearly constant during the simulation. The deflection is due to the compressibility in the hydraulic fluid.

7.3.4 Case 4

Plots from the simulation of Case 4 are shown in Figure 7.10. The figure shows that the pressure of Volume 1 of the cylinder of Joint 2 reaches the supply pressure after approximately 9 s, at which the load force is about 289 kN. This corresponds to a load in the field of gravity with a mass of 29.5 t. The result corresponds to the expected result.

7.3.5 Case 5

The leakage used in the simulation is given by the scaling factor $\alpha = 0.99$ for both cylinders. The scaling factor was defined in Section 3.4. Plots from the simulation of Case are shown in Figures 7.11 and 7.12. The two top plots in Figure 7.11 show that the piston of Joint 2 creeps when the valve is closed, and that the piston extracts to reach the upper piston limit. At around 25 s into the simulation the valve position must be set positive in order to avoid that the

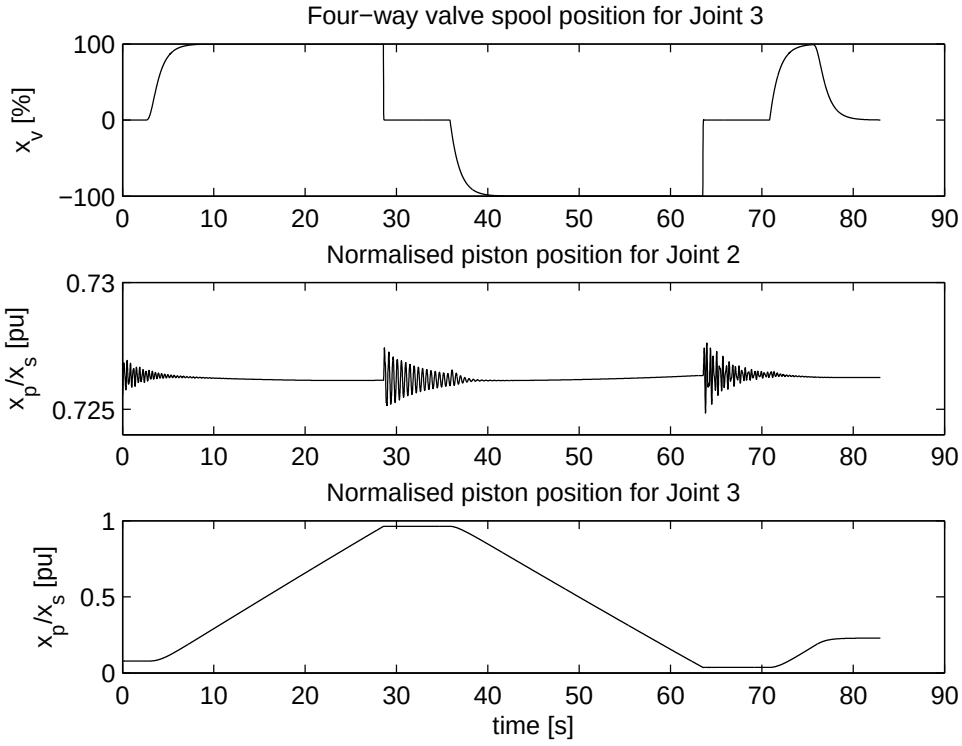

Figure 7.6: Crane and hydraulics test, Case 2: Cylinder piston motions during the testing of the limited piston travel functionality of Joint 3.

piston of Joint 2 moves outside its valid range. The motion of the piston of Joint 3 is because of the leakage the knuckle jib tends to hang vertically from the end of the knuckle boom. Comparing the progress of the pressures for Case 1 and 5, found in Figure 7.5 and 7.12, respectively, shows that the large oscillations in the pressure are avoided when leakage is introduced.

7.4 Winch and drive system

Validating the winch model is performed by three tests cases. In all cases the initial length of cable on the drum is 1200 m.

Case 1:
Why/How: Evaluate the motor and speed controller by running the motor at rated speed both ways with a 100 t static load, and verify that the motor follows the reference.
Expected results: The controller tracks the reference with limited deviation.

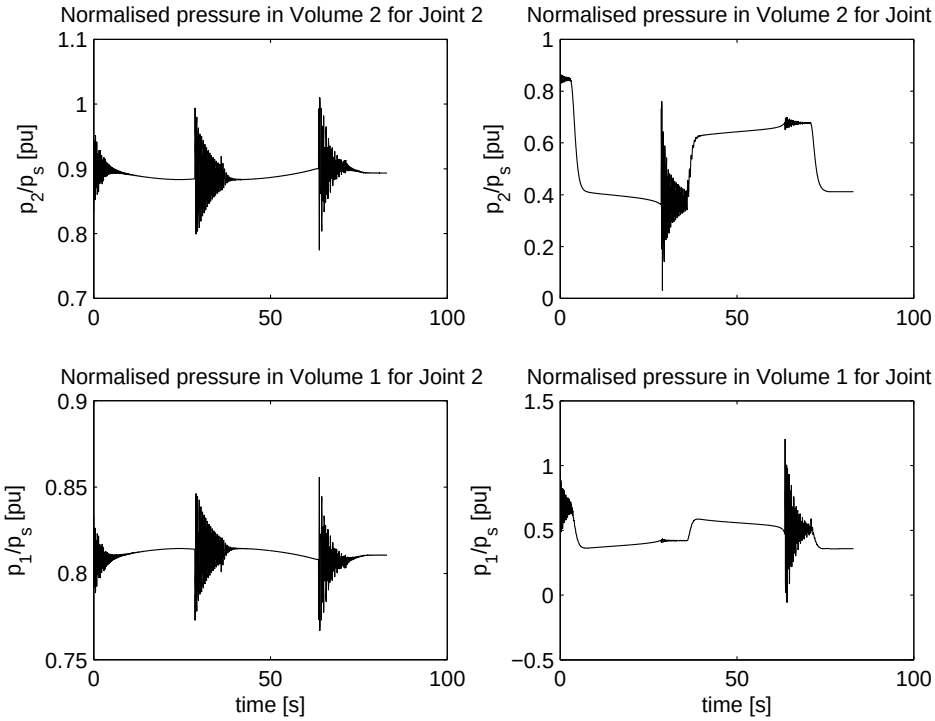

Figure 7.7: Crane and hydraulics test, Case 2: Progress of cylinder pressures during testing the limited piston travel functionality of Joint 3.

Case 2:
Why/How: Evaluate the motor and speed controller with a 200 t static load.
Expected results: The motor will not be able to follow the commanded speed as well as in Case 1. This will be especially prominent if the motor torque saturates.

Case 3:
Why/How: Evaluate the disc brake by paying out cable at rated motor speed and then enabling the disc brake. The static load is 100 t.
Expected results: The motor shall be quickly brought to a full stop.

7.4.1 Case 1

Plots from the simulation of Case 1 are shown in Figure 7.13. The top plot shows the normalised motor speed, and the second plot shows the deviation between the reference and the motor speed. It is seen that the motor follows the commanded speed well. Also, it is seen that the motor is able to both hold the load at zero speed and work as a brake. The bottom plot shows that the motor has torque in excess.

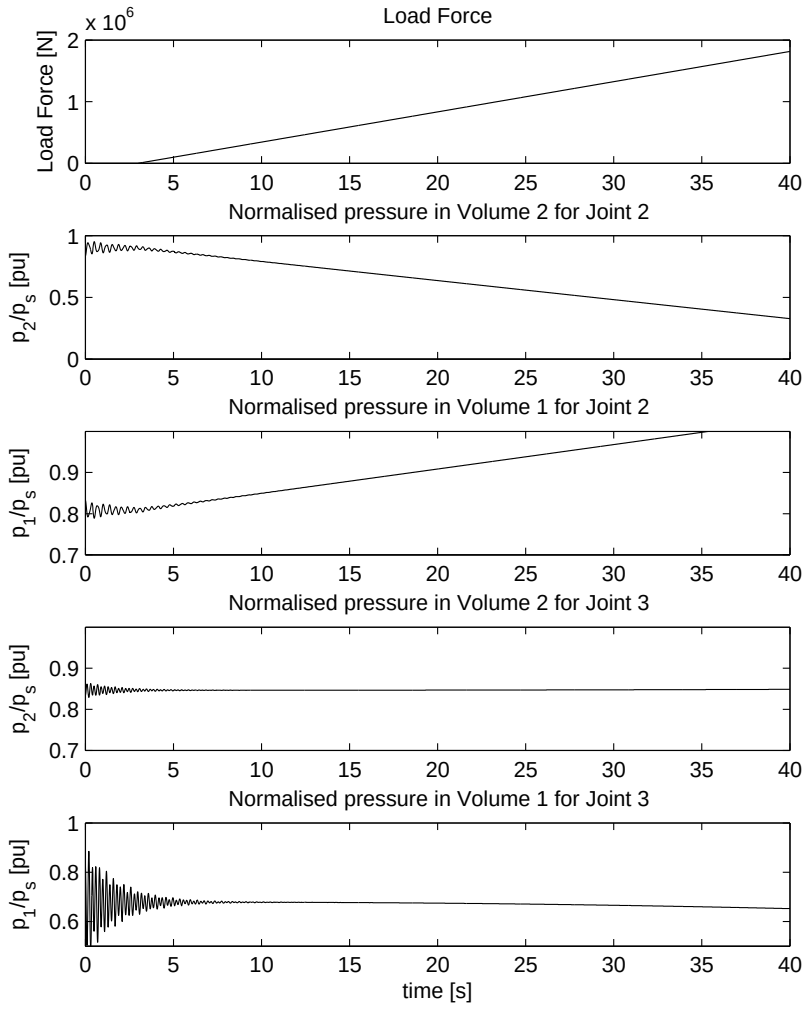

Figure 7.8: Crane and hydraulics test, Case 3: Load force and cylinder pressures.

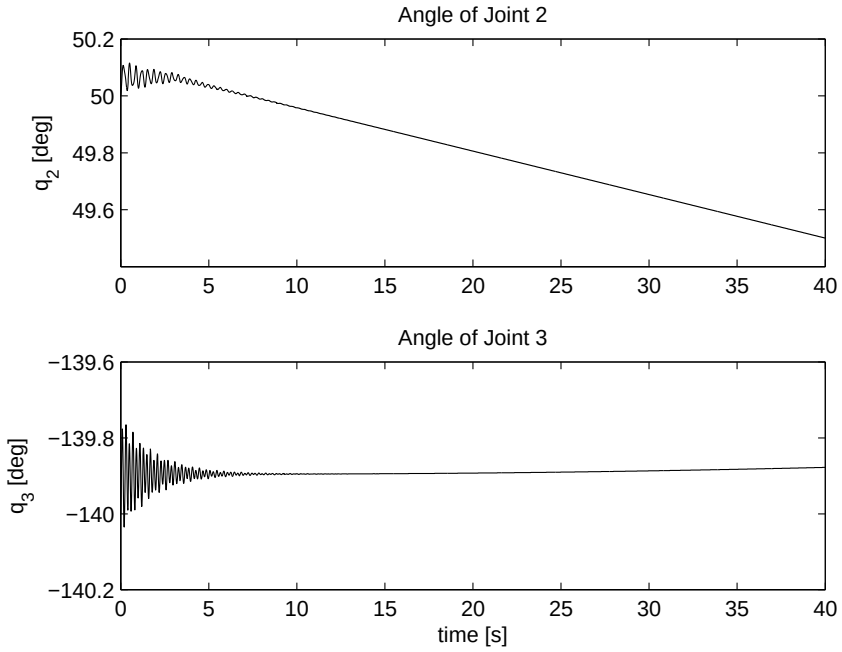

Figure 7.9: Crane and hydraulics test, Case 3: Angle deflections.

7.4.2 Case 2

Plots from the simulation of Case 2 are shown in Figure 7.14. The plots show that the motor is able to follow the reference when cable is payed out, but the motor torque saturates for a short moment during the braking of the load. During the upwards acceleration of the load, the motor torque again saturates resulting in a large motor speed deviation. Eventually, however, the motor is able to reach rated speed. The results are as expected.

7.4.3 Case 3

Plots from the simulation of Case 3 are shown in Figure 7.15. The bottom plot shows that the disc brake is disabled after 2 s, and the motor starts paying out cable after approximately 5 s. After 15 s the motor has attained rated speed, and the disc brake is enabled, effectively stopping the motor.

7.5 Payload and winch and drive system

In this section the winch and drive model is joined with the payload and hoisting cable model. The presented simulations will validate the interconnection of the two models, the constant tension mode, heave compensation mode, lift-off and

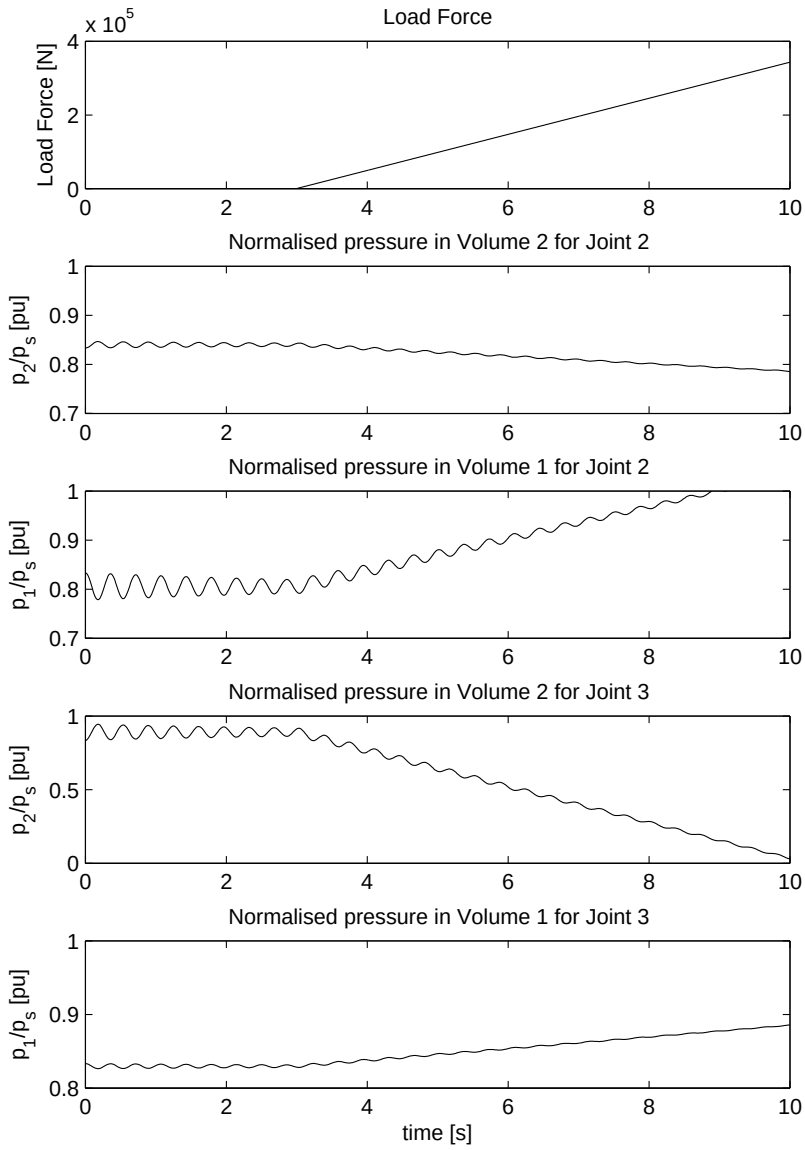

Figure 7.10: Crane and hydraulics test, Case 4: Load force and cylinder pressures.

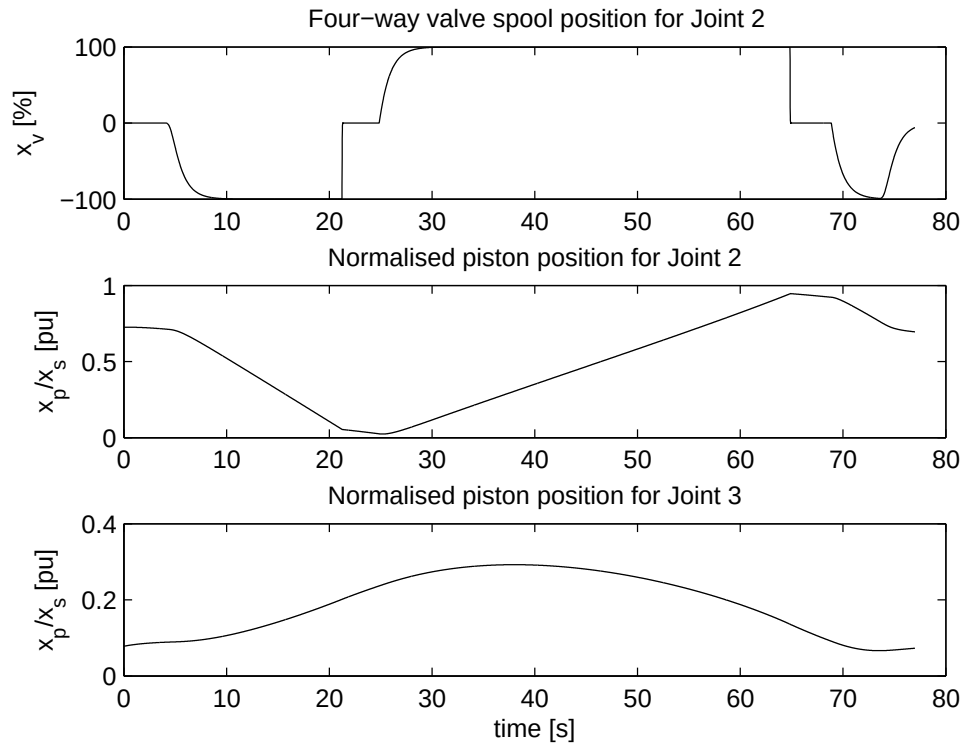

Figure 7.11: Crane and hydraulics test, Case 5: Cylinder piston motions during testing the limited piston travel functionality of Joint 2 with leakage.

landing the payload, lifting the payload through the wave zone, and the initial transients when the payload is initially in the air and suspended in the cable.

In all test cases the parameters of Cable 2 from Section 4.9 are used. Since the hydrodynamic model is thoroughly tested in [28], the sphere geometry is used in all simulations, and with a mass of $M_l = 100$ t. In the simulations where waves are present, regular waves with frequency 0.5 rad/s and amplitude 0.7 m is used.

Case 1:
Why/How: Evaluate the Constant Tension mode by starting the simulation with an initially slack hoisting cable, and pre-tensioning the cable by the CT mode before lifting the load from a steady deck. By successively landing the load onto the deck, both the lift-off and landing functionality of the normal force model is tested. The test case will also verify that the initial position of the load – for the case when the load is resting on a surface – is correct.
Expected results: The load shall initially be at a height H_l above the deck. Turning on the CT mode, the cable length should decrease, and as the cable elongation increases to a level above zero, the DAF will converge to the predefined tension.

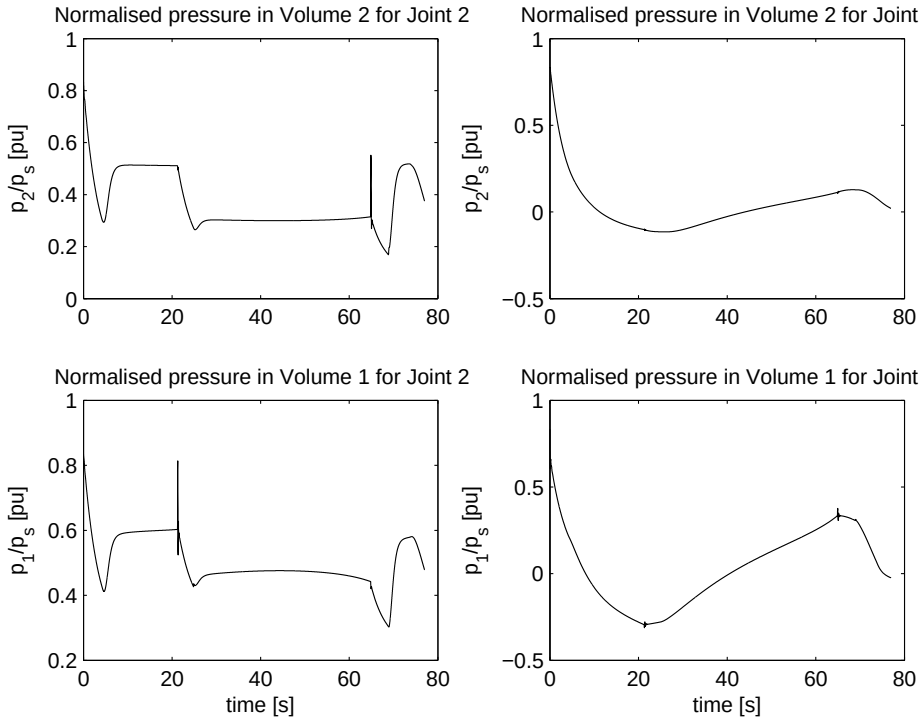

Figure 7.12: Crane and hydraulics test, Case 5: Progress of cylinder pressures during the testing of the limited piston travel functionality of Joint 2 with leakage.

When commanding a hoisting speed to the motor, the command from the CT mode shall decrease to zero, and the DAF shall increase. When the DAF is above one, the load shall lift off, and the DAF will oscillate around zero. When lowering the load, the DAF shall continue to oscillate until the load touches the deck after which the DAF shall decrease and become zero when ΔL_c becomes negative.

Case 2:
Why/How: Evaluate the interactions and transitions in the models. Simulating a vessel in waves by imposing the same sine motion on both the boom tip position and the deck, and sinusoidal waves, pre-tension the cable with CT, then lift the load into the air. Disabling the normal force model, the load is lowered into the water, and when the load is below the wave zone, turn on HC mode.
Expected results: Except from a sinusoidal payload motion, the initial progress of the simulation should be as in Case 1 until the load is lifted from the deck. Lowering the load into the water, the hydrodynamic force shall arise, and the DAF is expected to have its largest oscillations during this phase. Turning on the HC mode, the load shall be lowered at a nearly constant speed, and the amplitude of the oscillations of the DAF shall decrease. Setting the speed command to zero,

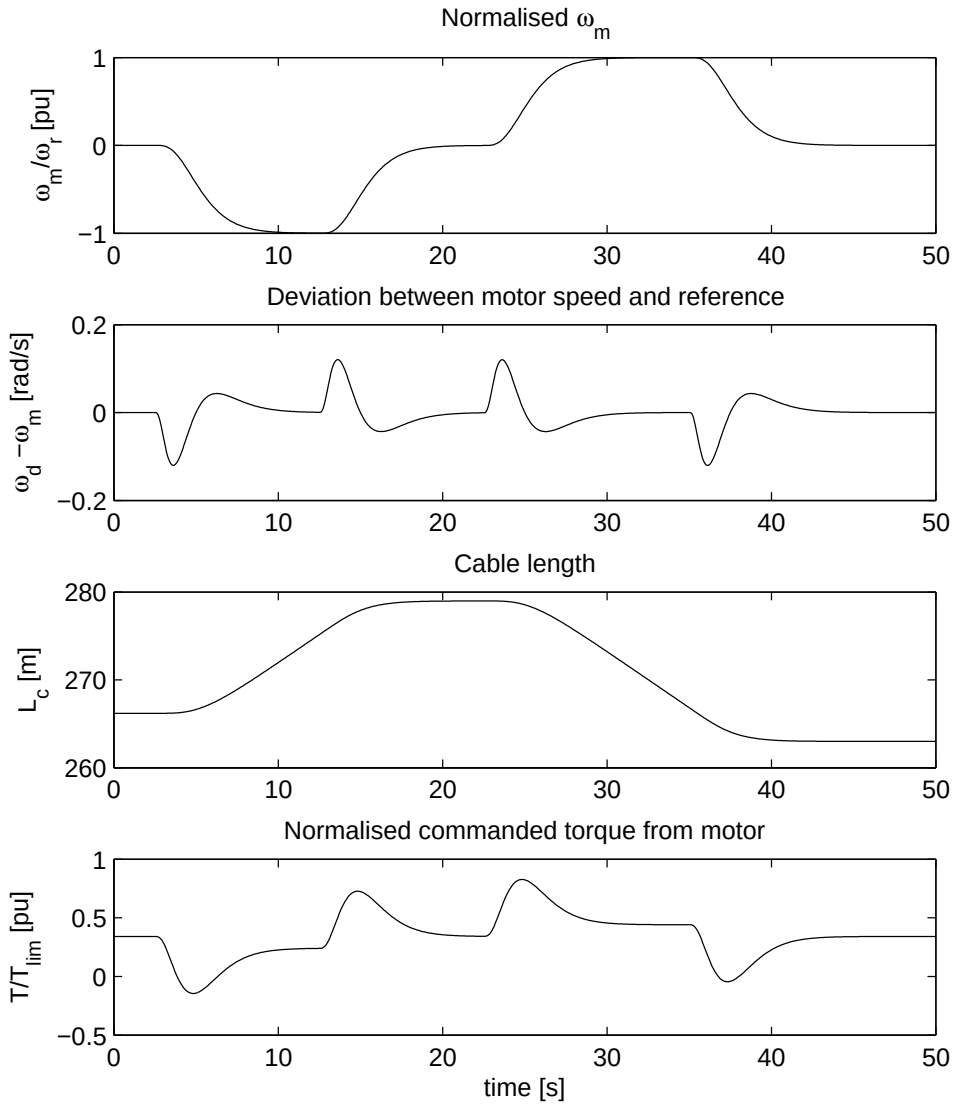

Figure 7.13: Winch test, Case 1: Testing speed controller under normal loading conditions.

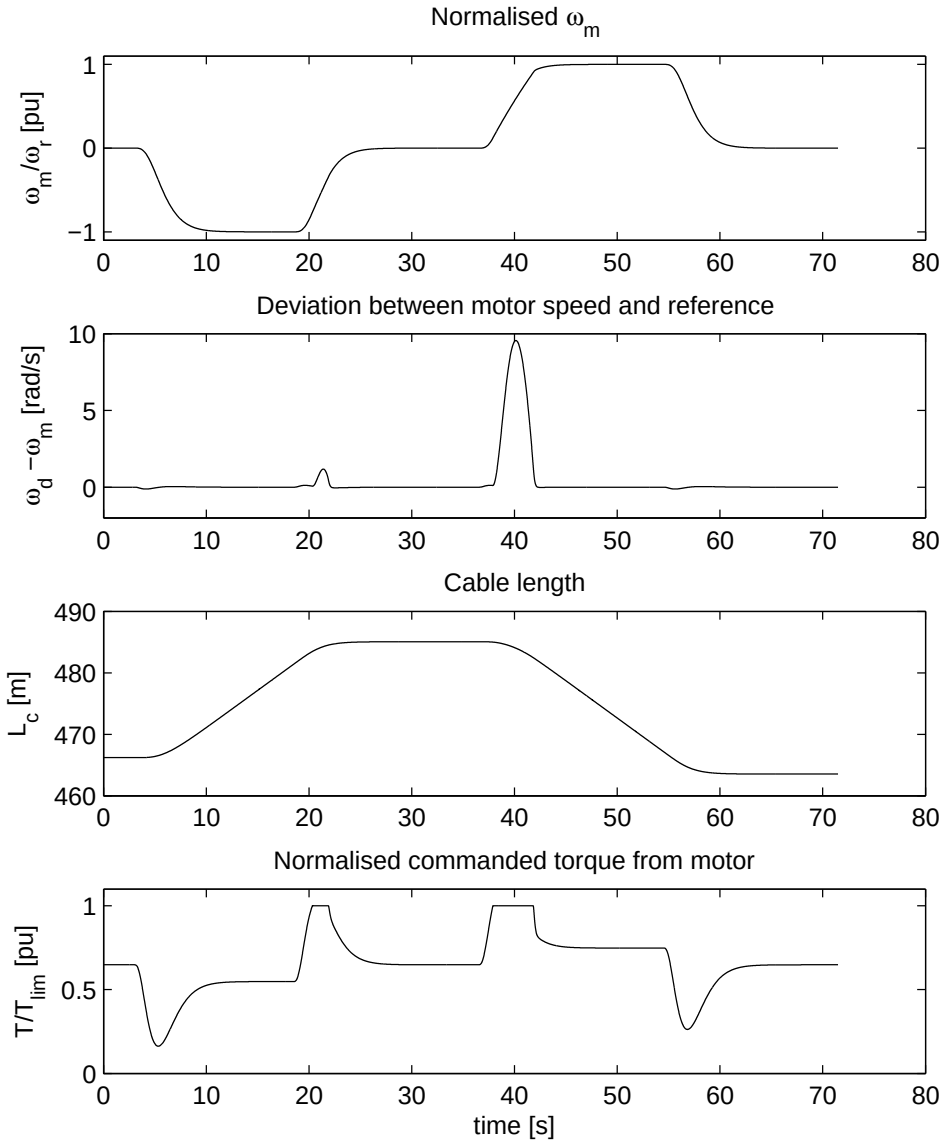

Figure 7.14: Winch test, Case 2: Testing speed controller under excessive loading conditions.

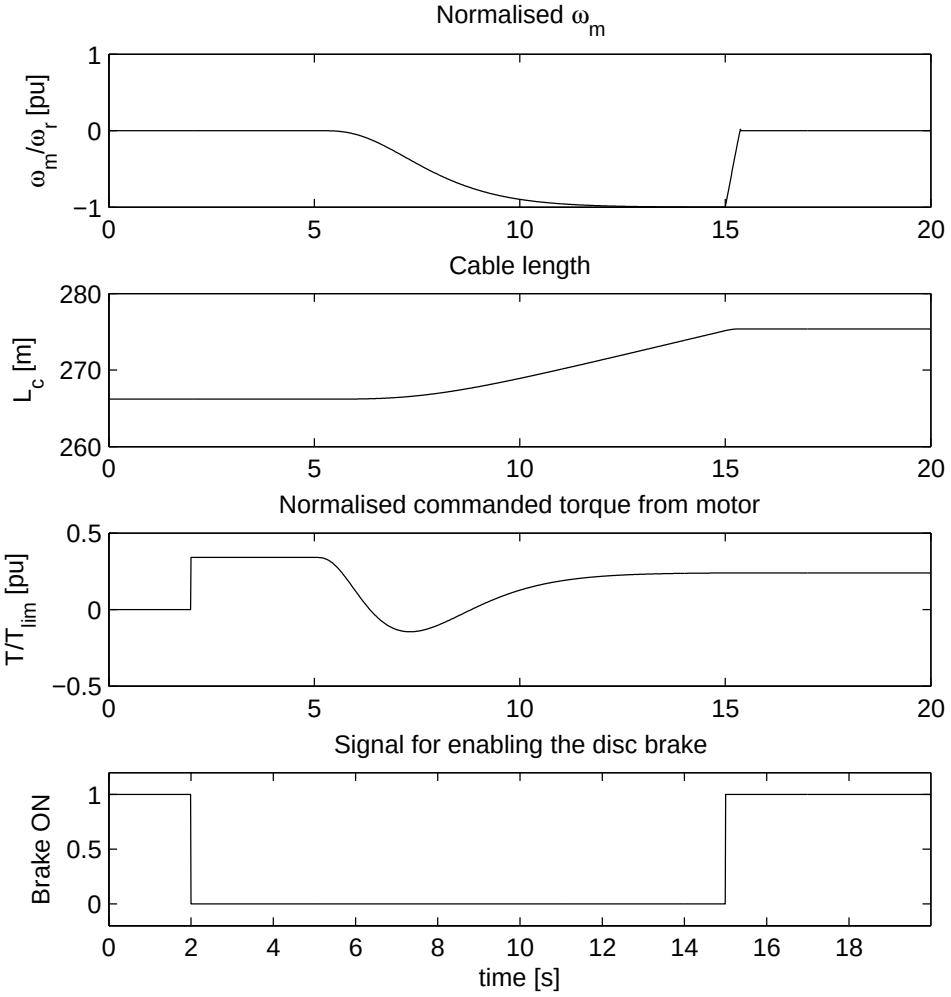

Figure 7.15: Winch test, Case 3: Testing the disc brake.

the load shall be held at a nearly constant position.

Case 3:
Why/How: Evaluate the heave compensation performance. Run the first 20 s of the simulation with the HC mode off. Then turn it on and evaluate the transition. Run the simulation until maximum attenuation is obtained. Also, the test case will verify the initialisation of the payload position when the load is suspended in the cable and in water.
Expected results: The transition when the HC mode is enabled should be smooth. No prediction of the expected ratio of the attenuation of the motion of the payload due to the boom tip motion is present, but the ratio of attenuation should be significant.

Case 5:
Why/How: Evaluate the initialisation procedure for the hoisting cable and payload model when the payload is suspended in the cable, and is in the air.
Expected results: The initial position shall be practically exact the position of equilibrium, and no oscillations in the payload position should occur.

7.5.1 Case 1

In this simulation, the boom position is $z_b = 15$ m, the deck position is $z_d = 3$ m, and the height of the payload is $H_l = 2$ m. The desired cable tension F_d is 40 % of the dry weight of the payload, and the initial length of cable on the winch drum is 1455 m.

Plots from the simulation of Case 1 are shown in Figure 7.16. The plots show that the simulation evolves as expected. The CT mode is turned on after about 2.5 s, and the slack in the cable is pulled in (ΔL_c increasing). When the cable elongation becomes positive, the DAF increases to the desired tension level of the constant mode. After about 20 s, a positive speed is commanded, and at the same time the CT mode is turned smoothly off. When the load is in the air, the speed reference is set to zero, and the load oscillates around a fixed position. After nearly 37 s, a negative motor speed is commanded, and the load is lowered onto the deck. When the load hits the deck, the DAF and cable elongation decrease, and the DAF becomes zero at the moment when the cable elongation becomes negative.

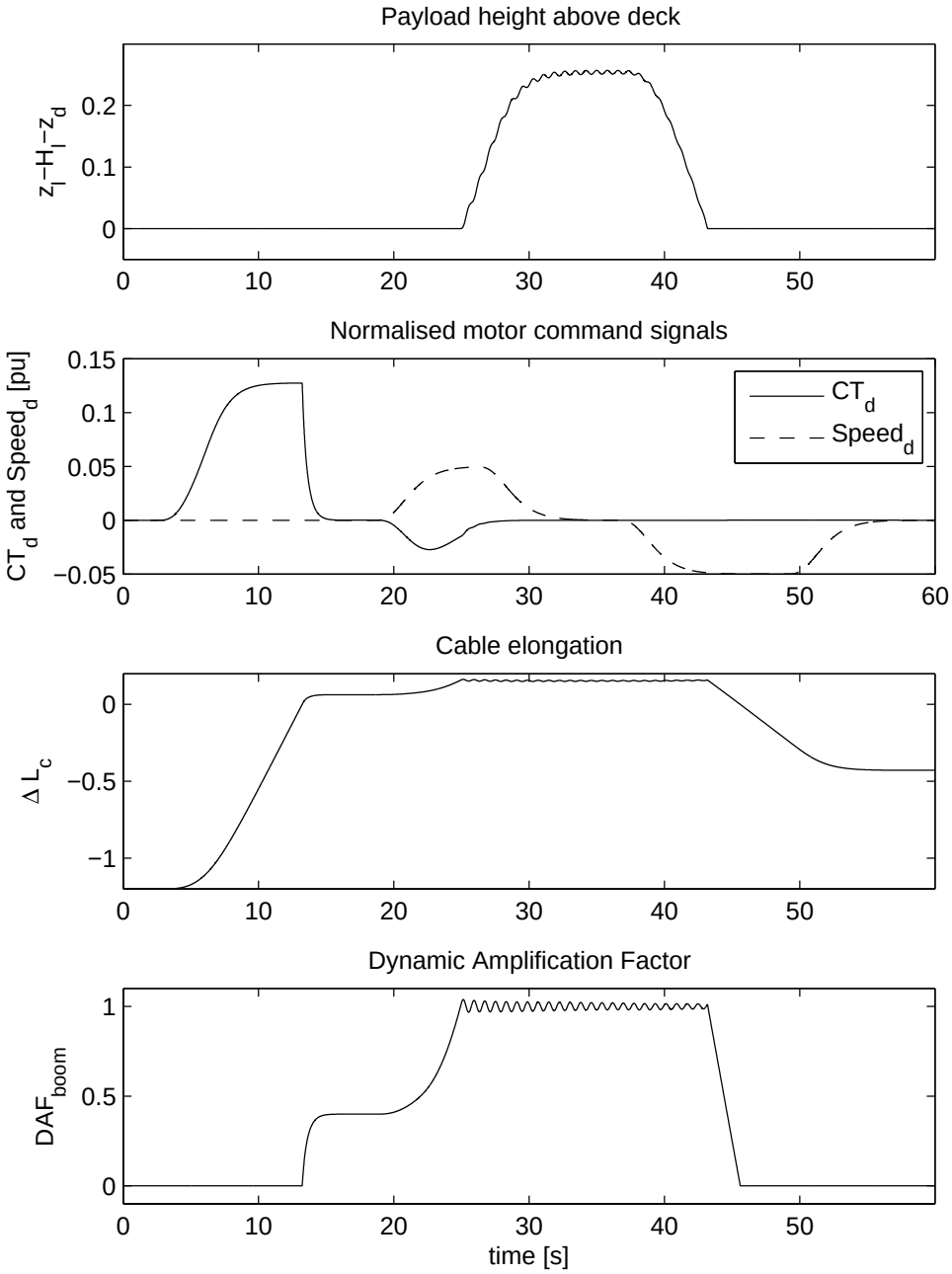

Figure 7.16: Payload and winch testing, Case 1: Testing the constant tension mode.

7.5.2 Case 2

In this simulation, the boom position oscillates with an amplitude of 0.6 m and frequency of 0.6 rad/s around the offset of 15 m. The deck position oscillates with the same frequency and amplitude around 3 m. The height of the payload is $H_l = 5$ m which corresponds to a payload with mass density 1.5 times greater than seawater. The initial length of cable on the winch drum is 1458 m and the desired cable tension F_d is the same as in Case 1.

Plots from the first 70 s of the simulation of Case 2 are shown in Figures 7.17 and 7.18, and in Figures 7.19 and 7.20 from the remaining 90 s. As expected, the second and third plots of Figure 7.17 shows the same progress as in Case 1. When the load lifts off from the deck, the DAF oscillates around one as in Case 1, however, now the low frequent motion of the boom influences the DAF. After about 45 s, the normal force is disabled and the load is lowered towards the water surface.

After approximately 75 s, the payload touches the water, and the hydrodynamic force arises as shown in the bottom plot of Figure 7.19. The third plot in Figure 7.19 shows that the largest variations in the DAF are during the water entry phase. The largest DAF value is 1.13. As shown in Figure 7.20, 135 s into the simulation the HC mode is turned on, and the DAF decreases significantly. Then, after about 150 s, the lowering speed of the payload is set to zero, and from the top plot in Figure 7.19, it is seen that the payload motion stops.

7.5.3 Case 3

The same boom tip and deck motion as in Case 2 is used in the simulation of Case 3, and the initial cable length is 1000 m.

Plots from the simulation of Case 3 are shown in Figures 7.21, 7.22 and 7.23. The plots in Figure 7.21 show that the motion of the payload is significantly reduced shortly after the HC mode is enabled, and that the HC mode effectively attenuates the motion influence on the load from the vessel. The plots in Figure 7.22 show the last ten seconds of the simulation. The plots show that the DAF varies with an amplitude of $1.46 \cdot 10^{-3}$, and the load position with an amplitude of 11.8 mm. This corresponds to a damping ratio of 98 %. The plots in Figure 7.23 show the first 40 seconds of the simulation. After 20 s the HC mode is enabled, and the plots show that the transition if bumpless.

7.5.4 Case 4

The same boom tip motion as in Case 2 and 3 is used in the simulation of Case 3, and the initial cable length is 1000 m. The seabed is at a position of $z_d = -455$ m, and the desired cable tension is 20 % of the dry weight of the payload.

Plots from the simulation of Case 4 are shown in Figures 7.24 and 7.25.

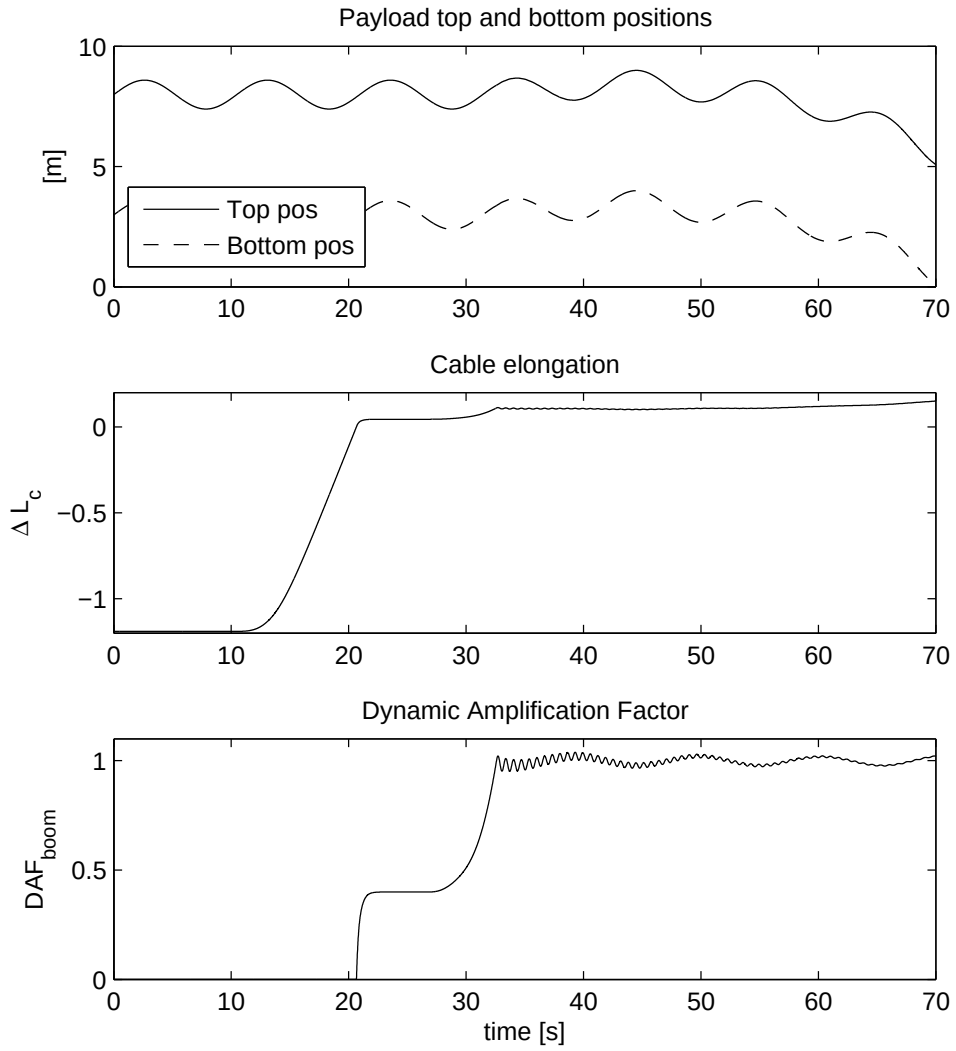

Figure 7.17: Payload and winch testing, Case 2: Lifting the load into the air from the vessel deck. First 70 s.

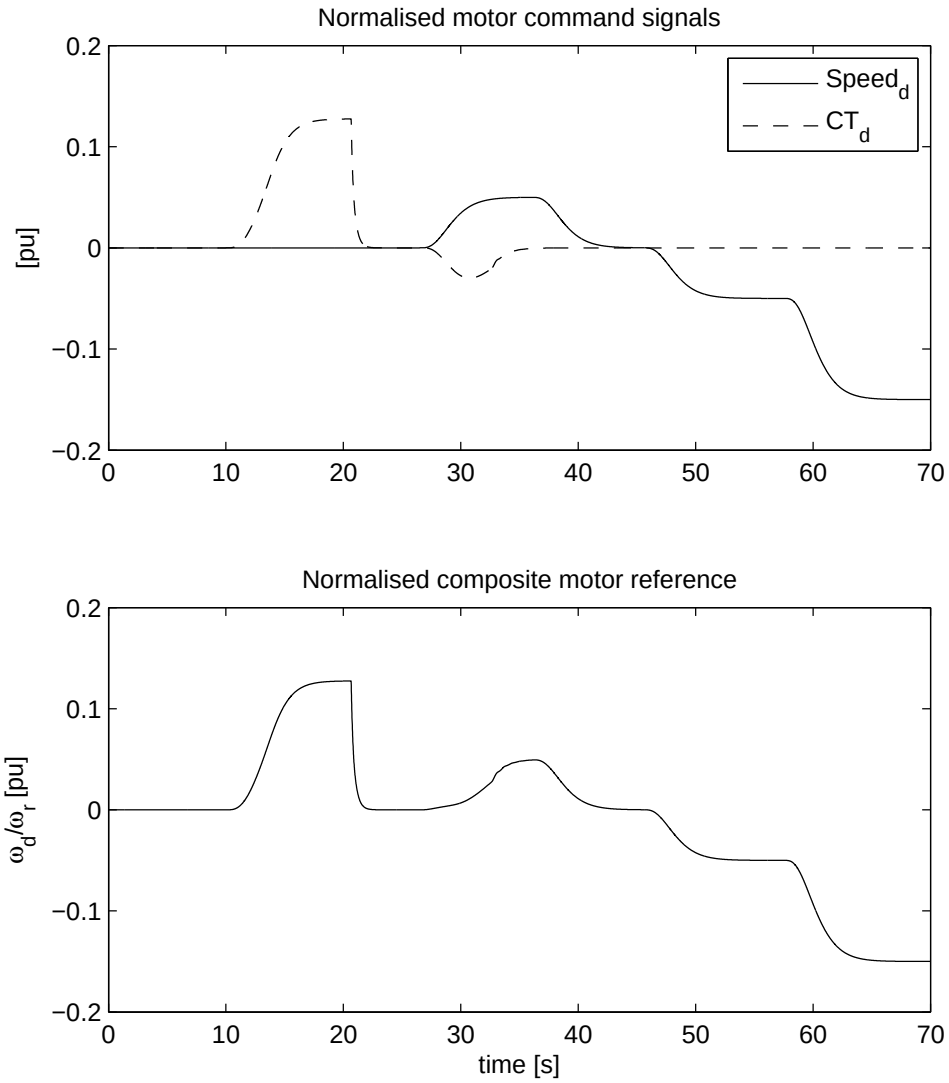

Figure 7.18: Payload and winch testing, Case 2: Lifting the load into the air from the vessel deck. Motor reference. First 70 s.

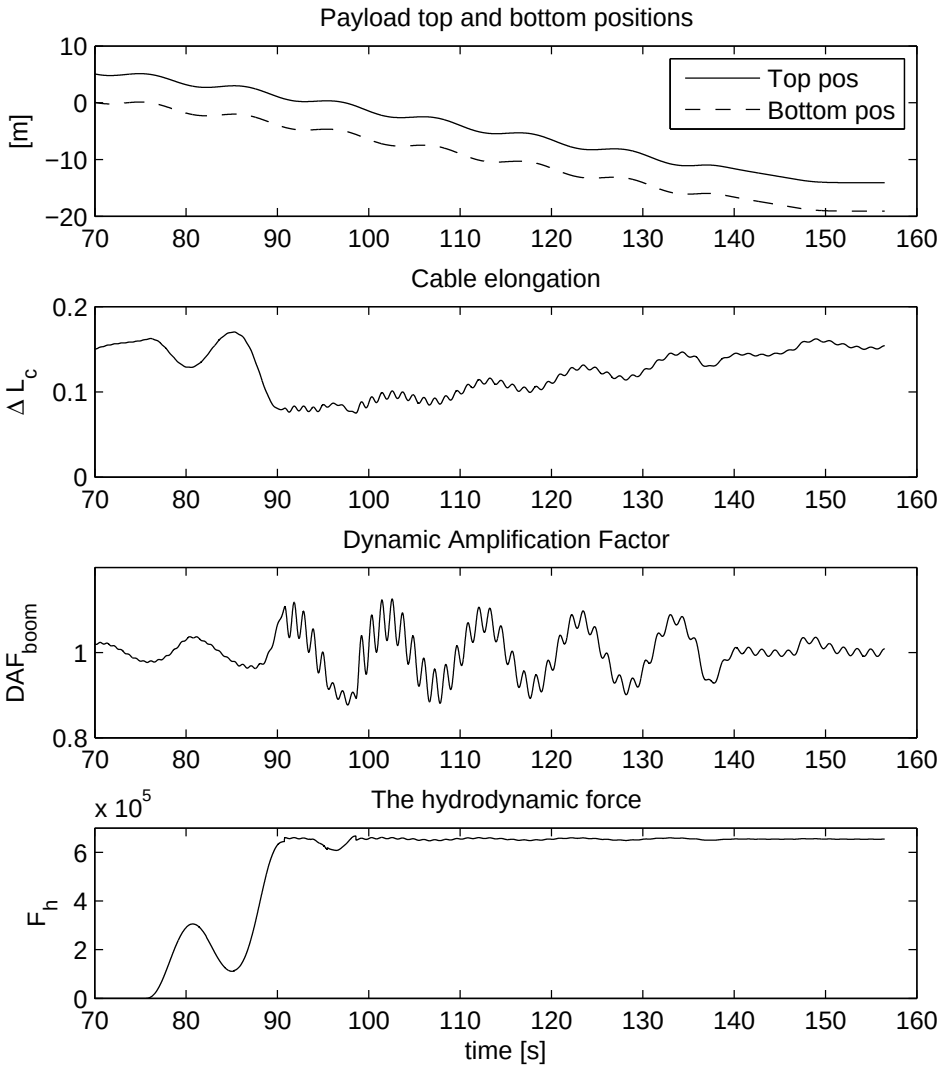

Figure 7.19: Payload and winch testing, Case 2: Lifting the load into the air from the vessel deck. Last 90 s.

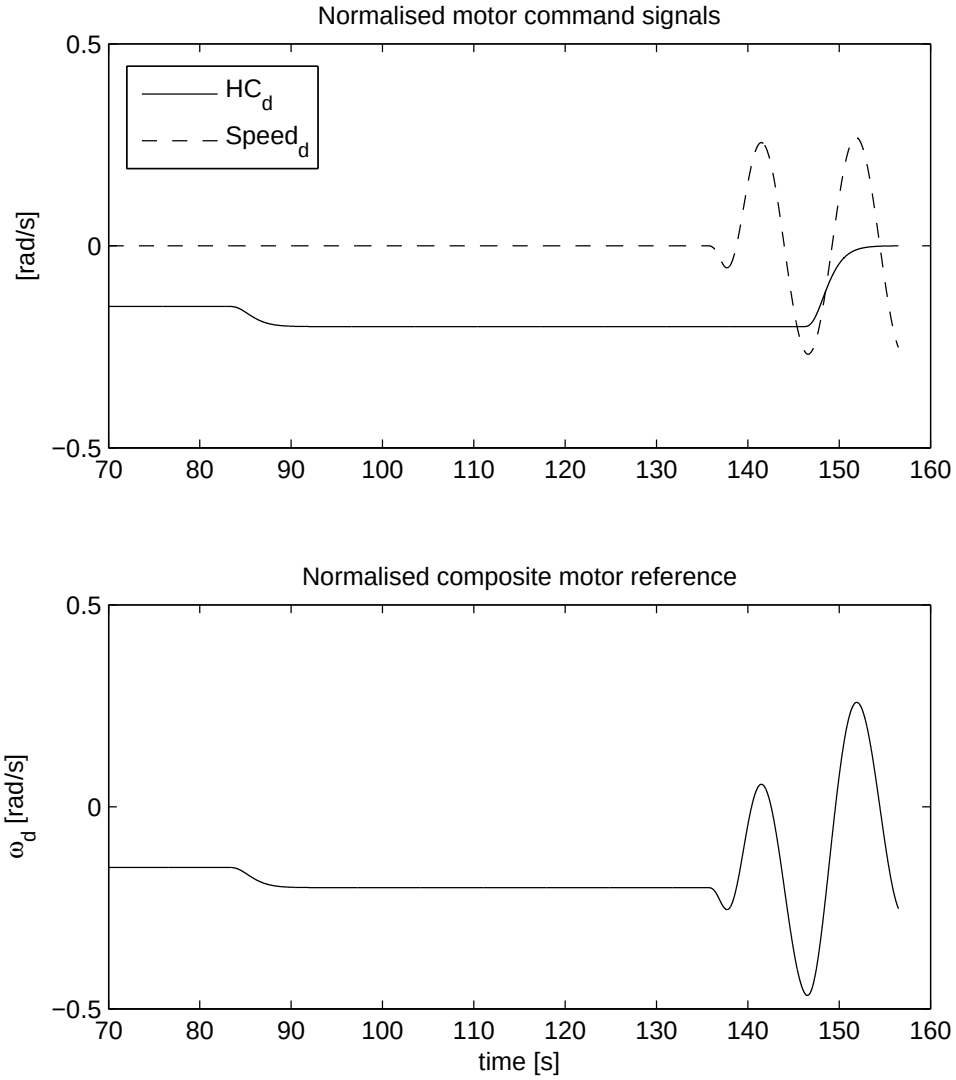

Figure 7.20: Payload and winch testing, Case 2: Lifting the load into the air from the vessel deck. Motor reference. Last 90 s.

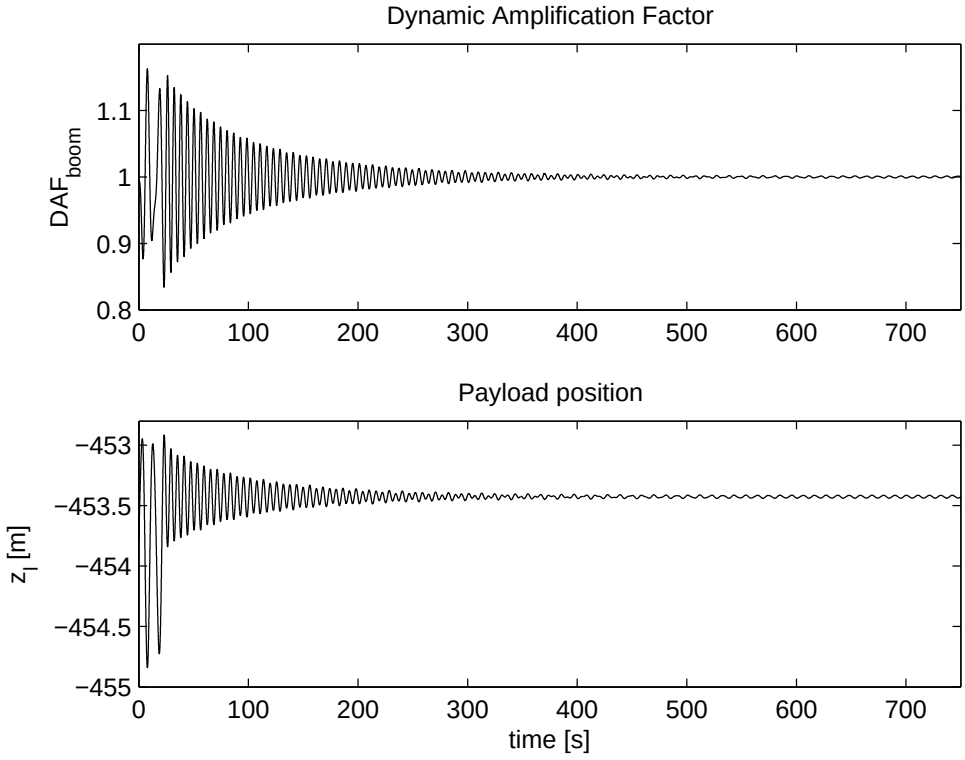

Figure 7.21: Payload and winch testing, Case 3: Testing HC. Long simulation.

The second and fourth plots in Figure 7.24 show that the HC and CT modes are enabled after about 6 s, and the slack in the cable is being pulled in. After 44 s the cable elongation becomes positive, and the DAF increases from zero. After about 100 s ω_d is given an offset by $Speed_d$, which effectively lifts the load from the seabed.

This test case shows that the interplay of the HC and CT modes works well.

7.5.5 Case 5

Plots from the simulation of Case 5 are shown in Figure 7.26, and show that the computation of the initial position of the payload is perfect.

7.6 The complete simulator

The next step is to join all parts of the simulator and verify the performance. Due to the limited lifting capacity at a large radius, the mass of the payload used in the remaining simulations is $M_l = 25$ t, and the parameters of Cable 1 from Section 4.9 are used. The height of the payload is $H_l = 3.14$ m, which corresponds

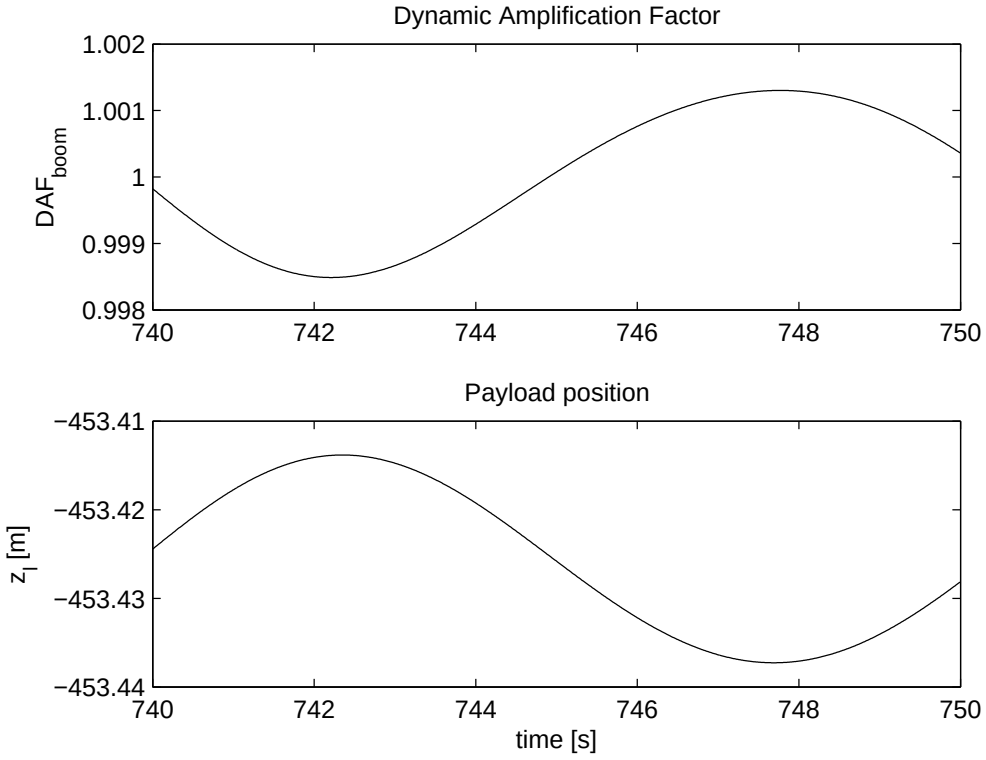

Figure 7.22: Payload and winch testing, Case 3: Testing HC. End of simulation.

to a payload with mass density 1.5 times greater than the mass density of seawater. In all test cases the initial crane joint angles are $\mathbf{q}(0) = [0^\circ \quad 40^\circ \quad -130^\circ]^T$.

Case 1:
Why/How: Verify that it is possible to lift and land the payload by luffing the knuckle boom. Before luffing, the cable shall be pre-tensioned by use of the CT mode.
Expected results: It is possible to simulate this scenario. Transients may be expected in the cylinder pressures.

Case 2:
Why/How: Evaluate initial transients when the load is initially suspended in the hoisting cable.
Expected results: Depending on how accurate the procedure for determining the initial pressures in the cylinders are, the initial transients the cylinder pressures and cable load may or may not be within safe limits for the crane.

Case 3:

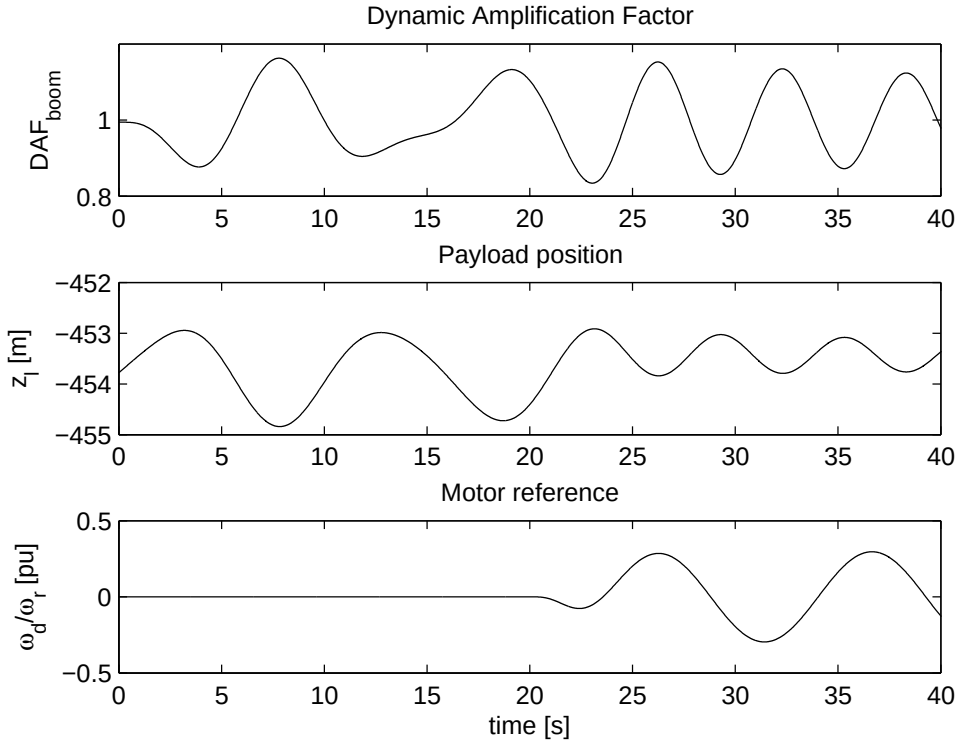

Figure 7.23: Payload and winch testing, Case 3: Testing HC. Start of simulation.

Why/How: Evaluate initial transients when the load is initially submerged and suspended in the hoisting cable.
Expected results: The transients are expected to be smaller in amplitude than in Case 2.

7.6.1 Case 1

In the present simulation the initial length of cable on the winch drum is 1455 m, the deck position is z_d3 m, and the desired cable tension F_d is 80 % of the dry weight of the payload.

Plots from the simulation of Case 1 are shown in Figures 7.27 and 7.28. The second plot in Figure 7.27 shows that the cable is tensioned by the CT mode to the preset tension level, and after almost 40 s the piston is moved outwards, shown by the bottom plot. This increases the tension in the cable, and at 40 s into the simulation the payload is lifted off the deck. After about 55 s the piston is moved inwards again, and the payload is eventually landed on the deck.

The plots of Figure 7.28 show the pressures in the cylinder volumes. The plots show that there are practically no transients in the pressures during the simulation.

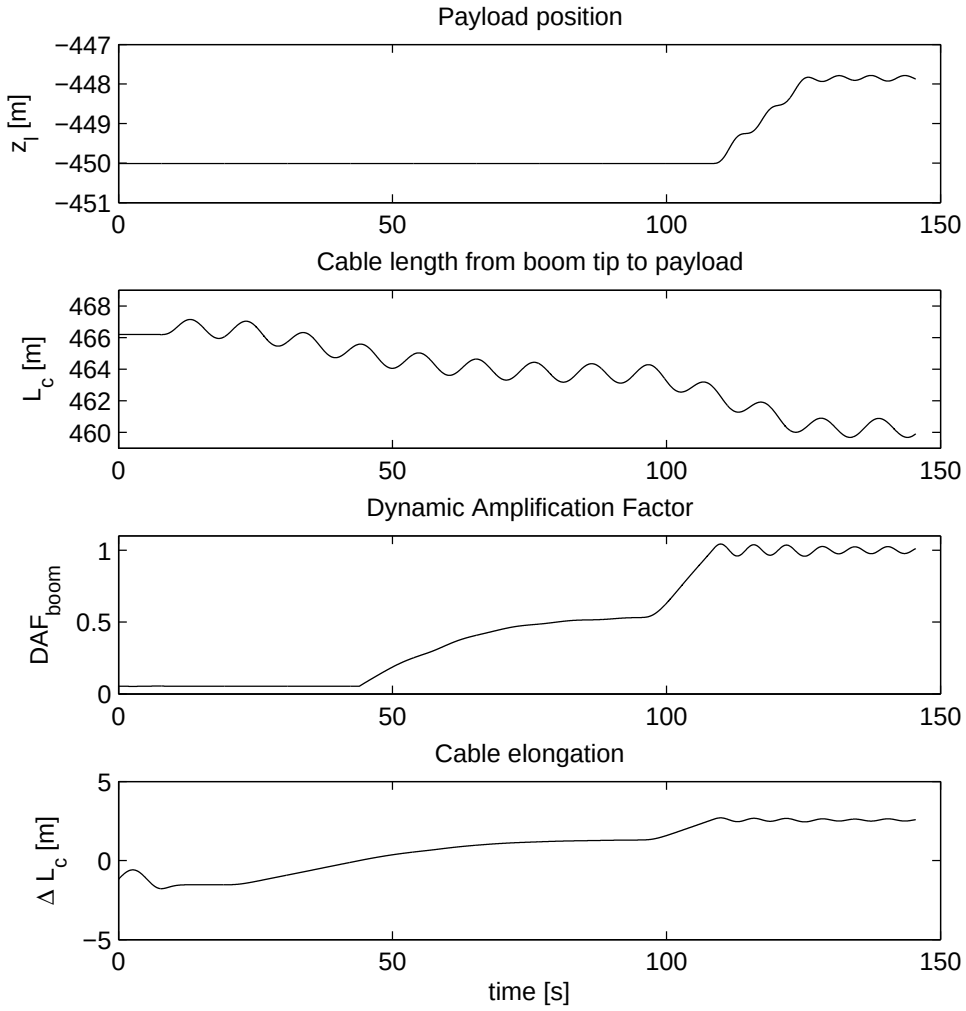

Figure 7.24: Payload and winch testing, Case 4: Lifting load from seabed with HC.

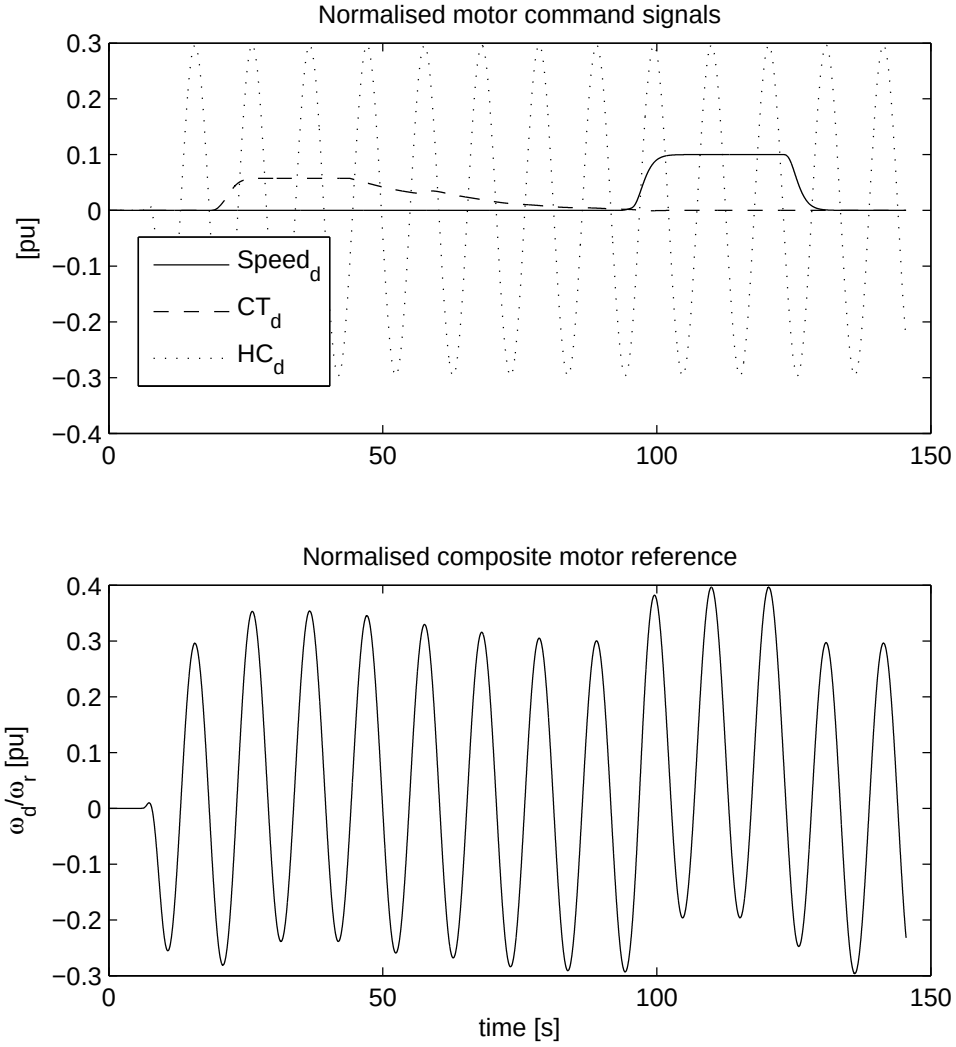

Figure 7.25: Payload and winch testing, Case 4: Lifting load from seabed with HC.

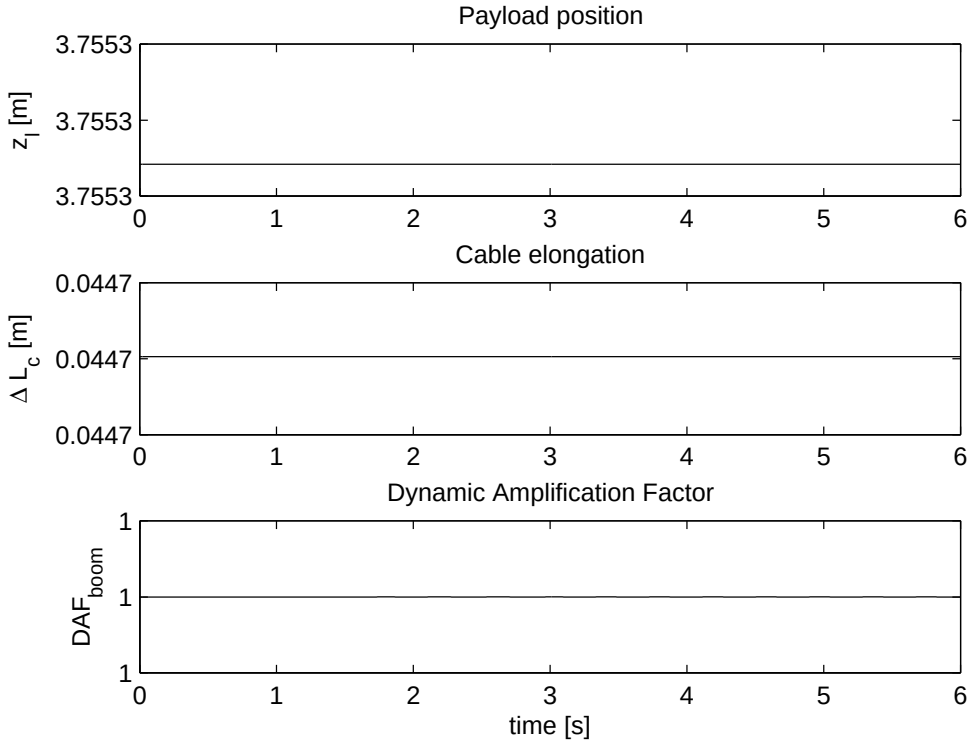

Figure 7.26: Payload and winch testing, Case 5: Model initialisation with the load in the air and suspended in the cable.

7.6.2 Case 2

In the present simulation the initial length of cable on the winch drum is 1455 m. Plots from the simulation are shown in Figures 7.29, 7.30, and 7.31. The top plot in Figure 7.29 shows that the payload oscillates with an amplitude of about 10 cm, and the bottom plot shows that the DAF is above acceptable limits. The third plot shows that a significant part of the payload motion is attributed to the variation in the cable elongation, and the second plot shows the motion of the boom tip which is given by the motion of the cylinder pistons, shown in Figure 7.30.

The plots in Figure 7.31 show that there are initial transients in the pressures of the cylinder volumes, but that the pressure levels are acceptable.

7.6.3 Case 3

In the present simulation the initial length of cable on the winch drum is 1455 m. Plots from the simulation are shown in Figures 7.32 and 7.33. The top plot in Figure 7.32 shows that the amplitude of oscillation for the payload motion

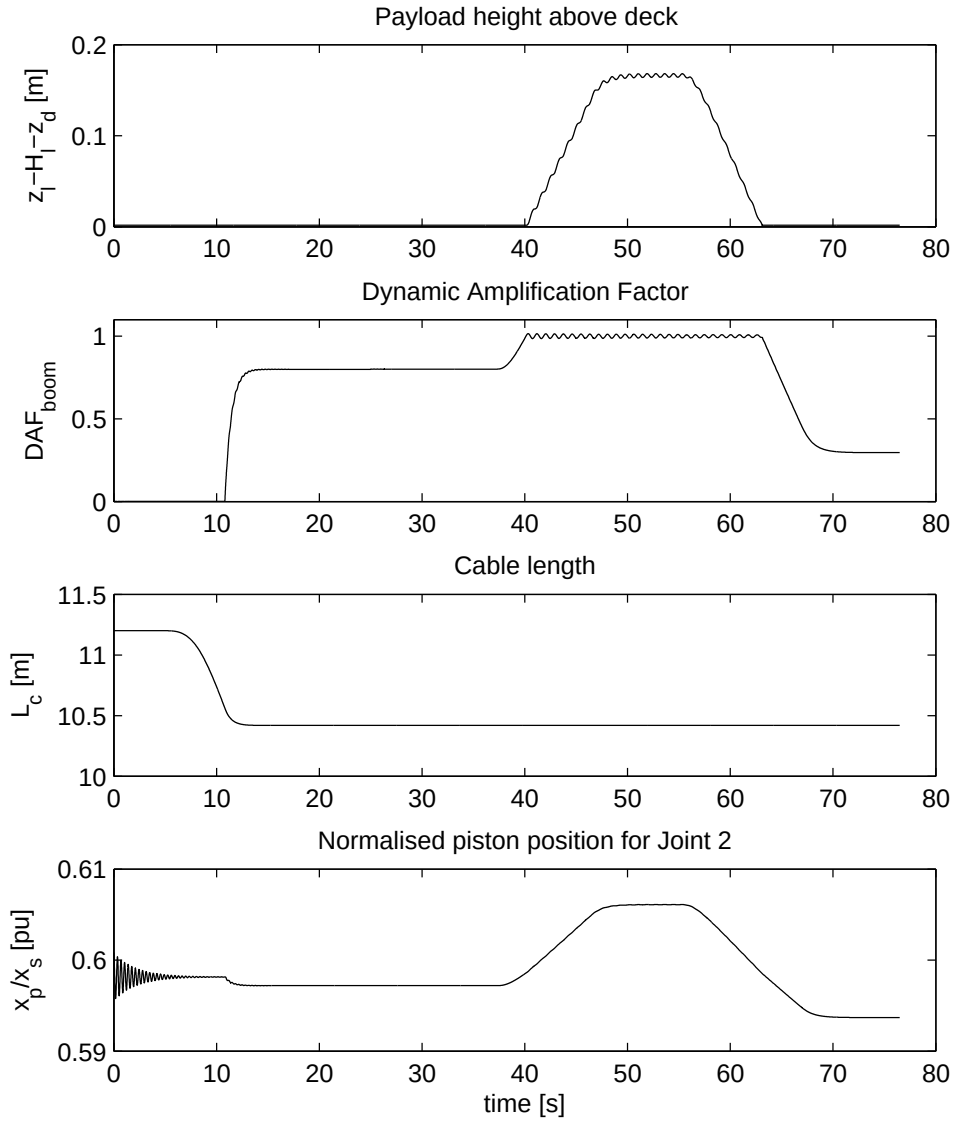

Figure 7.27: Complete crane simulator testing, Case 1: Lifting load from the deck by luffing the knuckle boom.

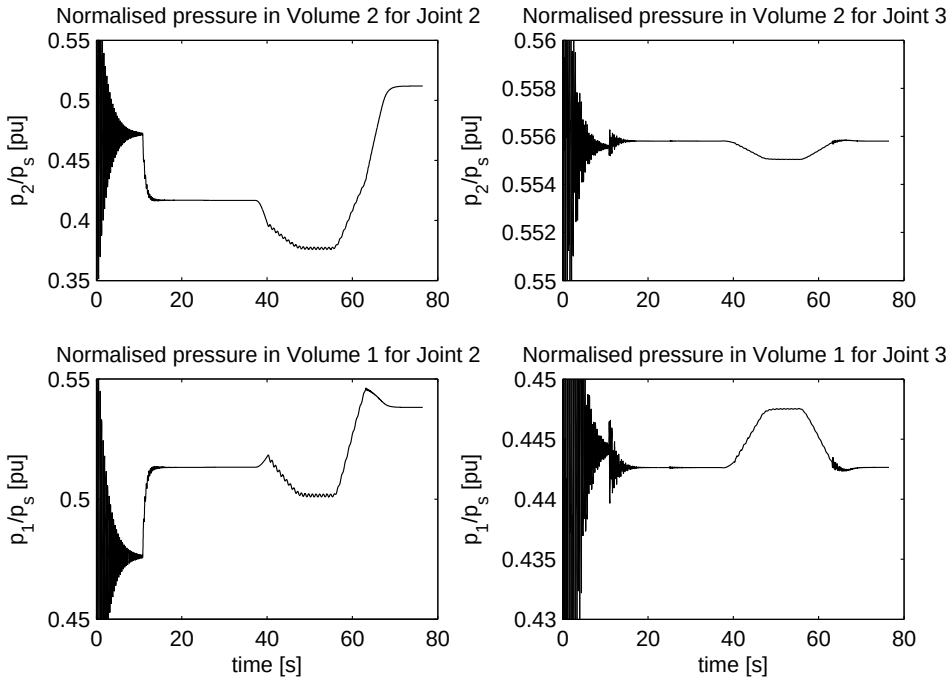

Figure 7.28: Complete crane simulator testing, Case 1: Lifting load from the deck by luffing the knuckle boom.

is to some degree smaller than in Case 2, and the frequency of oscillation is considerably lower. This would be expected due to the longer length of payed out hoisting cable. The bottom plot shows that the DAF is within acceptable limits. Comparing the first and third plot shows that the payload motion is due to the variation in the cable elongation.

Comparing the plots in Figures 7.33 and 7.31 show that the cylinder pressures are quite similar, but that the low frequent variation in the boom tip force (seen by the DAF plot in Figure 7.32) results in a more sinusoidal progress in the pressures of the volumes of the cylinder of Joint 2 compared to the simulation in Case 2.

7.7 Vessel and simulator

In order to verify the interface between the crane simulator and a vessel simulator, a vessel model is incorporated into the crane simulator model. The vessel motion is given by motion RAOs for a supply vessel, and waves are generated by a time realisation of the JONSWAP spectrum with peak frequency $\omega_p = 0.6$ rad/s and significant wave height $H_s = 2$ m. For a review of these concepts refer to ..... The

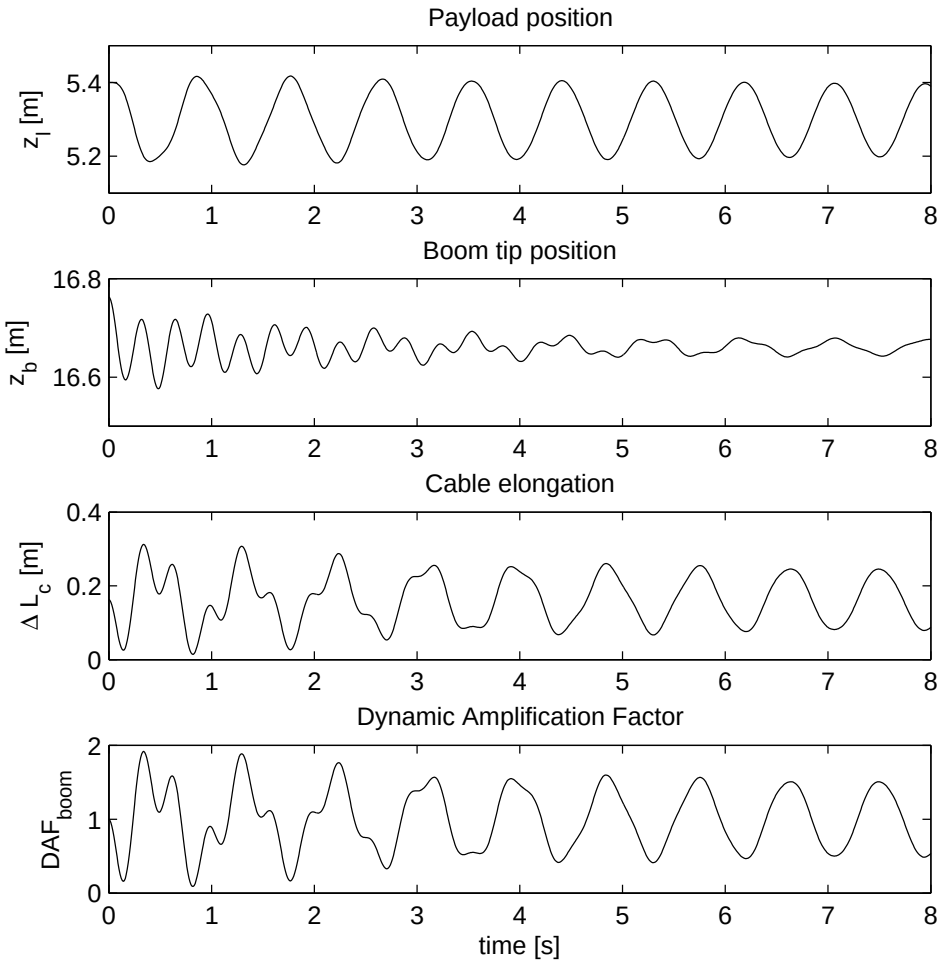

Figure 7.29: Complete crane simulator testing, Case 2: Initialisation with load in the air.

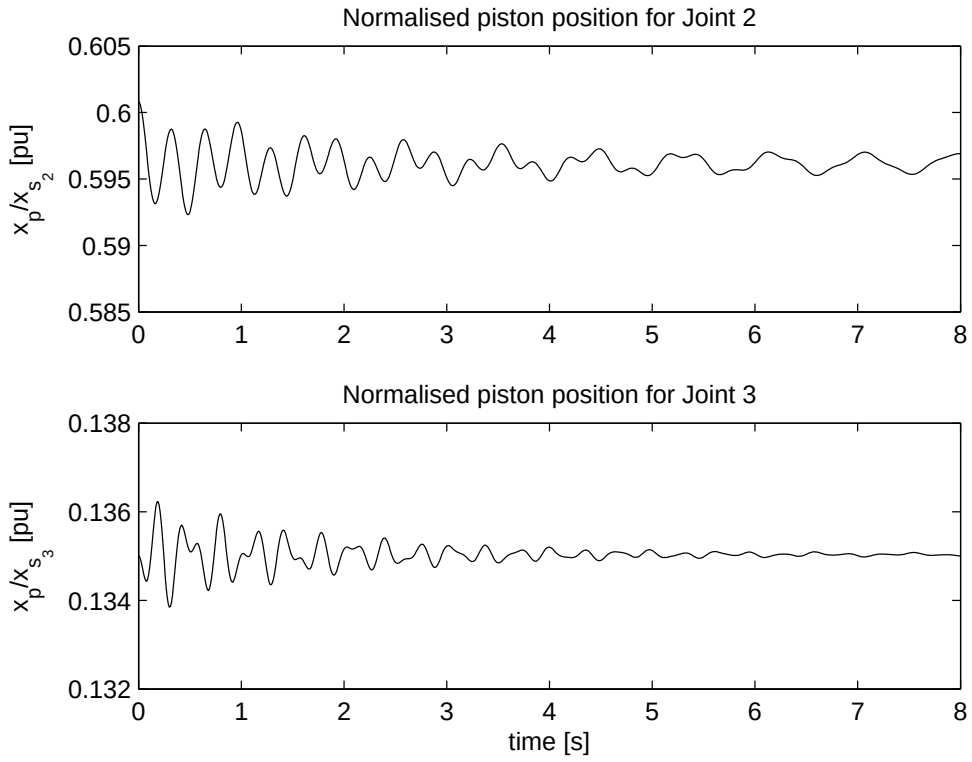

Figure 7.30: Complete crane simulator testing, Case 2: Initialisation with load in the air.

vessel which the RAOs are computed for has the following properties:

$$\text{LOA} \approx 93.90 \text{ m} \tag{7.1}$$

$$\text{LPP} \approx 80.80 \text{ m} \tag{7.2}$$

$$\text{Breadth} \approx 21 \text{ m} \tag{7.3}$$

$$\text{Design Draught} \approx 6.20 \text{ m, and} \tag{7.4}$$

$$\text{Displacement} \approx 7969 \text{ t} \tag{7.5}$$

A further detailed description of the vessel model is beyond the scope of this thesis.

One test case is presented:

Case 1:
Why/How: Verify the interconnection of the vessel and crane simulators, and validate the CT and HC modes in irregular waves.
Expected results: The load is held at a constant position during HC.

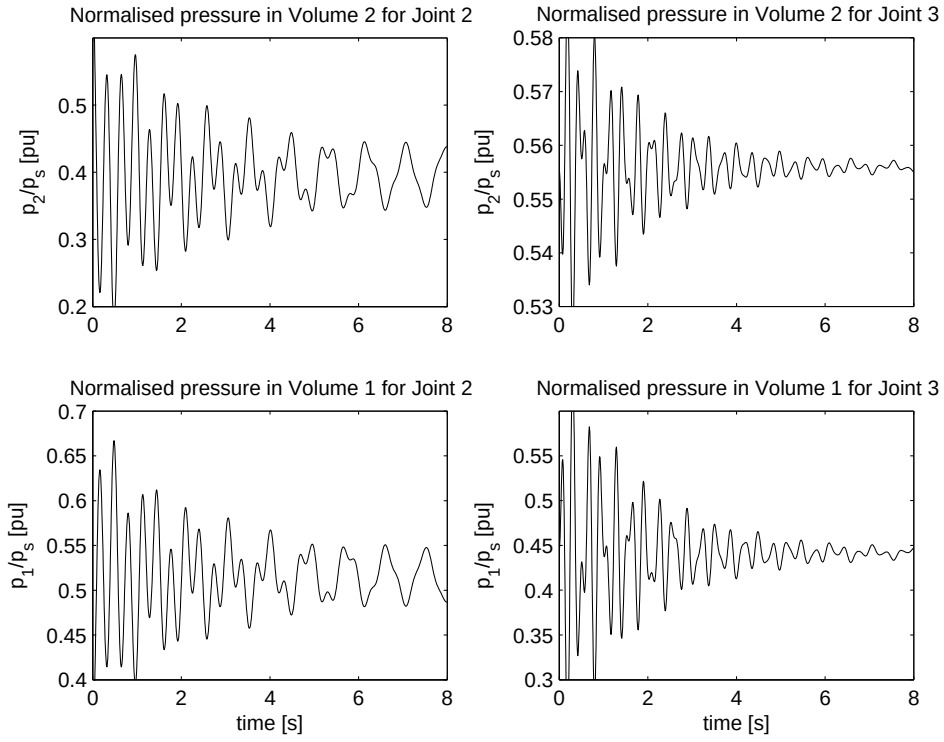

Figure 7.31: Complete crane simulator testing, Case 2: Initialisation with load in the air.

7.7.1 Case 1

Plots from the simulation of Case 3 are shown in Figures 7.34 The plots show that the CT and HC modes jointly tension the cable to a DAF level of approximately 0.6 before the CT mode is switched off and the load is lifted from the seabed. The DAF is $\in [0.97, 1.03]$ when the initial transients after lift-off have decayed.

The second plot shows that the payload creeps during the HC mode operation. The most likely explanation is that the motor speed controller only ensures convergence of the speed and not the position. Small errors in the integral effect will make the payload position drift. By introducing position feedback in the controller, the creeping presumably will be avoided.

7.8 Simulator properties

In order to get an impression of the crane simulation speed of the simulator, a benchmark test has been defined. The scenario employed is the same as in Case 1 of Section 7.6.1, but the times at which the simulator inputs are changed will be stated.

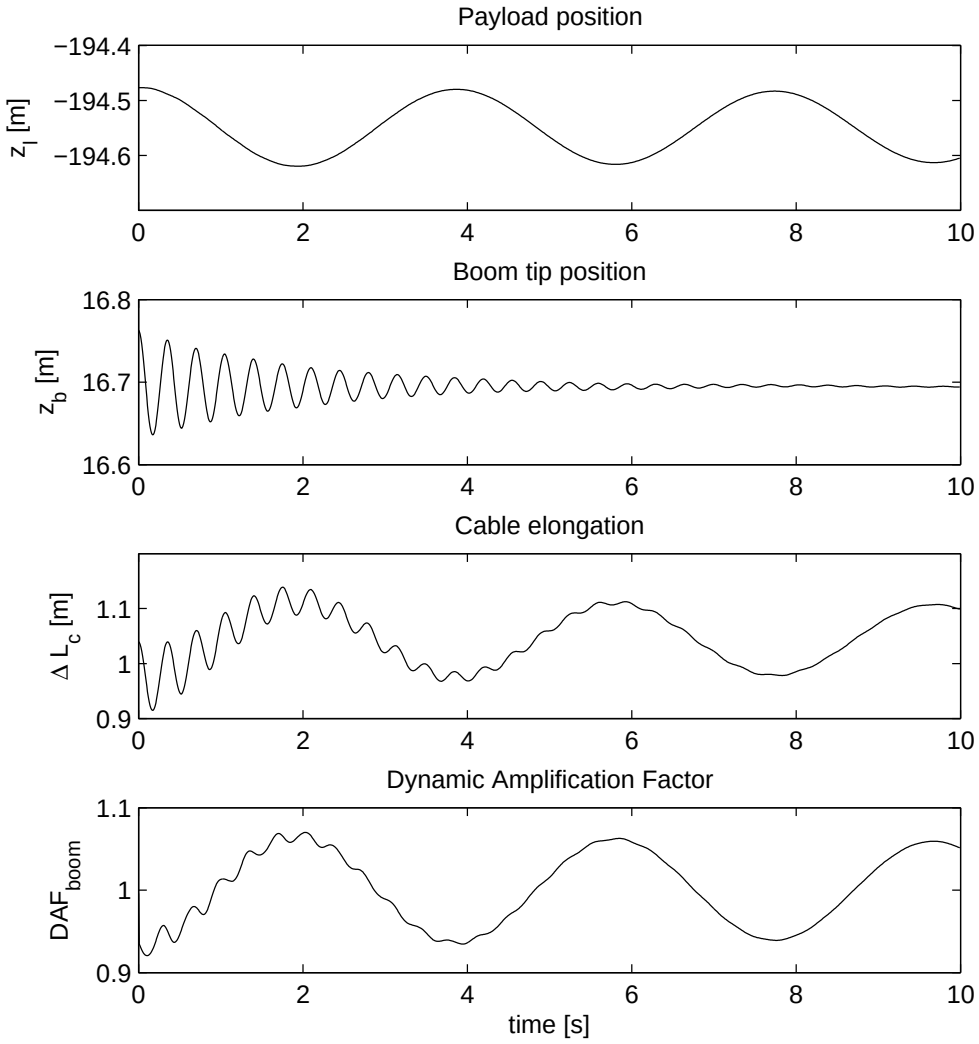

Figure 7.32: Complete crane simulator testing, Case 3: Initialisation with load in the water.

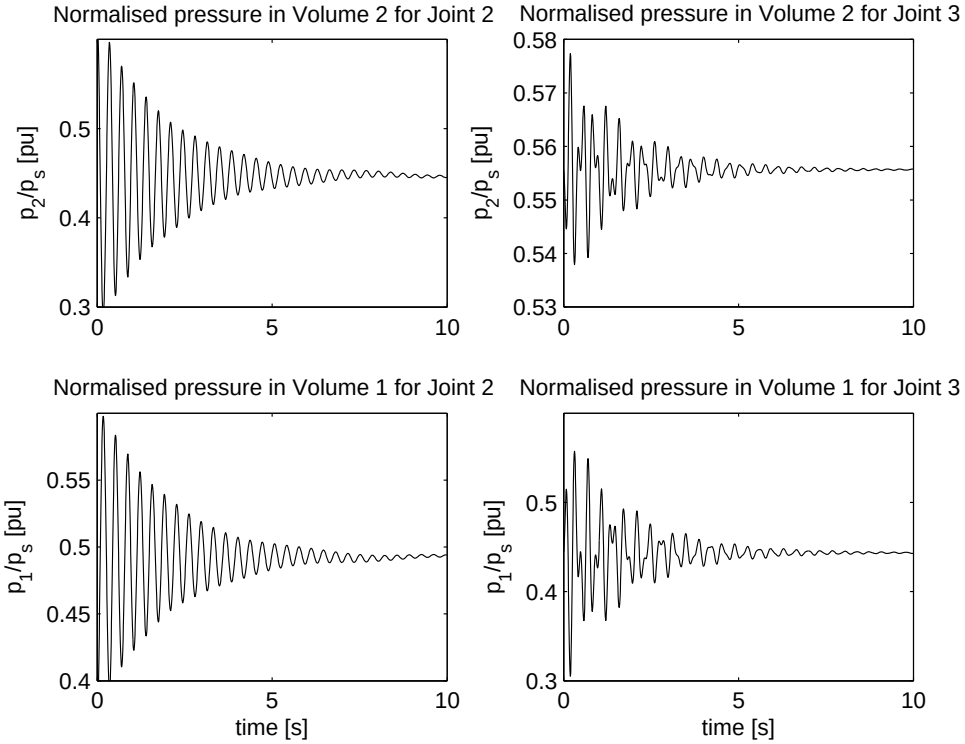

Figure 7.33: Complete crane simulator testing, Case 3: Initialisation with load in the water.

Initially, the cable is slack. After three seconds the CT mode is enabled, with $F_d = 0.2$. After 20 s the disc brake is enabled, and the four-way valve of Joint 2 is opened 50 %. This will lift the payload. After 35 s the valve is closed, then after 45 s it is opened to -50 %, and finally closed after 55 s. Now, the payload is once again resting on the deck. The simulation is stopped after 60 s.

The benchmark test is performed on a computer with an AMD Athlon 64 X2 Dual Core Processor 3800+ processor with a clock frequency of 2 GHz and 1 GB of RAM, running Microsoft Windows XP with Service Pack 3.

The benchmark test is performed with the Bogacki-Shampine integration routine, and with a step size of 10 ms, it takes 30.15 s to run the test. Removing all scopes results in a simulation time of 27.54 s. With a step size of 20 ms, it takes 14.62 s with scopes and 14.31 s without. With a step size of 30 ms, the simulation brakes down.

Optimisation of the simulation speed has not been focused on during the implementation of the simulator. Hence, it is to be expected that the simulation speed may be increased by optimising the model. Also, compiling the simulator with Real-Time Workshop [7] will presumably increase the simulation speed.

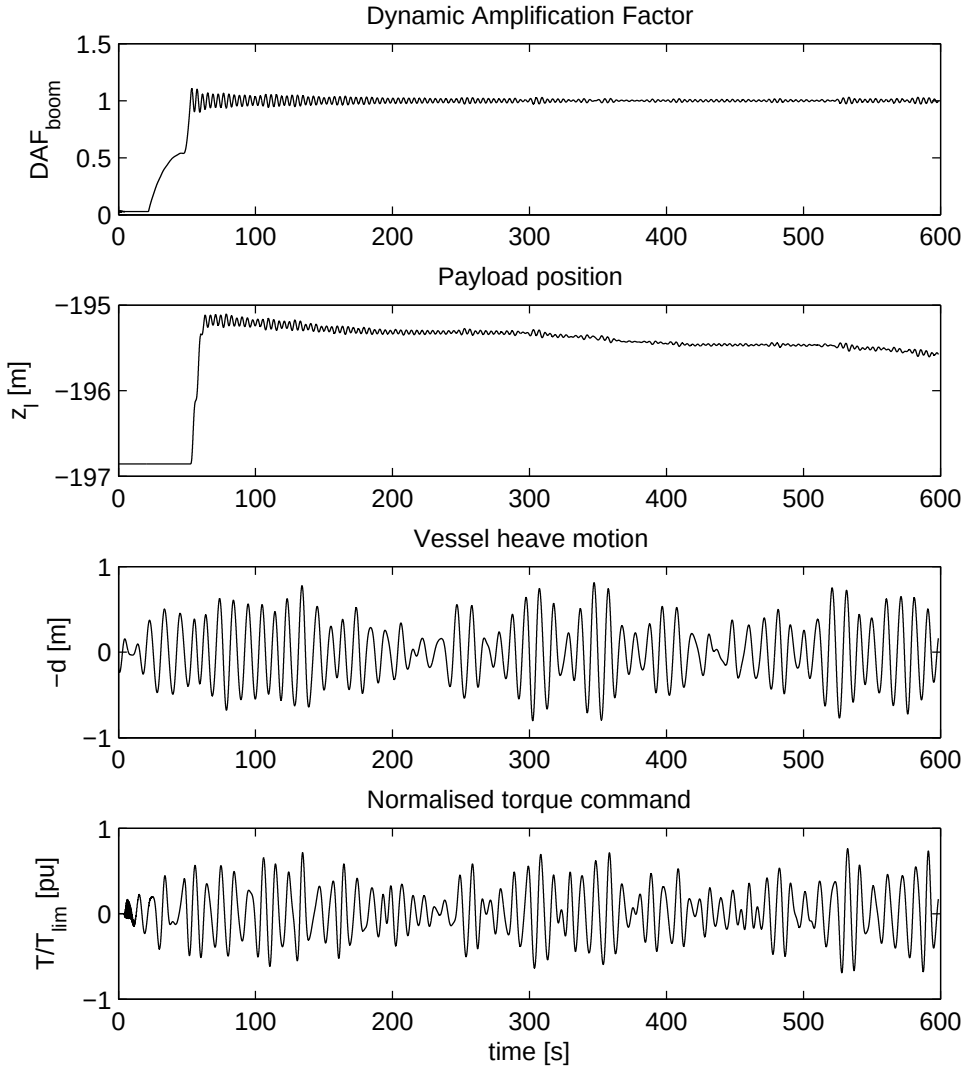

Figure 7.34: Crane simulator connected to vessel model, Case 1: Lifting the load from the seabed and into HC mode.

The simulator requires a total of 103 parameters. By making additional assumptions, some parameters may be defined by others. For example, in Section 2.6 it is assumed that the boom links are symmetric with homogenous mass distributions, which allowed for the definition of the vectors in Equations (2.82), (2.83) and 2.84 by the DH parameters. Disregarding insignificant effects, for example Coulomb friction, also reduces the number of parameters. By making such assumptions, the author reduced the minimum number of required parameters to 57.

This thesis has only regarded knuckle boom cranes. The derivation of the crane structure dynamics in Chapter 2, however, may be extended and generalised such that it can represent any crane structure with any number of revolute and telescopic joints by providing it with different configuration parameters; e.g. through the DH table the links will be defined as either revolute or prismatic. No changes need to be made to the payload and hoisting cable, and the winch and drive model if a different crane type is to be used in the simulator. The only change required is to insert correct number, and, potentially, the type of actuators for the crane joints.

The hydrodynamic parameters slamming, added mass, and volume of the submerged load are all implemented as so-called look-up tables by the respective non-dimensional terms. Hence, adding new payload geometries to the simulator, is straightforward when these parameters – and the linear and quadratic damping terms – are provided.

Chapter 8

Conclusions and further work

A crane simulator for real-time simulation of offshore crane operations by heave compensated knuckle boom cranes has been developed. The simulator is made up of a model for the crane structure dynamics; a model of hydraulics for luffing the knuckle boom and knuckle jib; a model of the payload and hoisting cable – including, among other, hydrodynamics; and a model for the winch and drive system.

The simulator modules have been validated qualitatively by simulation. Successively, modules have been joined, and the interconnection and interplay of the modules have also been verified in the same manner. Finally, the complete simulator was validated. The crane simulator's interface to a vessel simulator was verified by incorporating a vessel model into the crane simulator and running a simulation test.

The model validation showed that the simulator exhibits good performance, and, with the exception of realistic seabed interaction, is able to simulate a complete lifting operation. The simulator's interface to the vessel simulator was also shown to be correct.

The speed controller deployed on the winch drive, resulted in load creep during heave compensation in irregular waves. Introducing position feedback is presumed to avoid the creep.

Even though the simulator is made to simulate knuckle boom cranes, the simulator may be extended to simulate other crane types as well.

Interesting extensions to the simulator is to provide the wave elevation and the deck height at the payload's position, and seabed interaction effects.

Other interesting extensions include a three-dimensional payload and hoisting cable model, with the inclusion horizontal of effects such as currents and payload pendulation in air. Then a motor model for rotating the crane king should also be included.

Bibliography

[1] First interactive as web page. http://www.first-interactive.com, accessed 27 November 2008. [cited at p. 2]

[2] Globalsim web page. http://www.globalsim.com, accessed 27 November 2008. [cited at p. 2]

[3] Hydrolaunch web page. http://www.itk.ntnu.no/research/HydroLab, accessed 27 November 2008. [cited at p. 3]

[4] Kongsberg sim web page. http://www.km.kongsberg.com/sim, accessed 27 November 2008. [cited at p. 2]

[5] Mpri ship analytics web page. http://www.shipanalytics.com, accessed 27 November 2008. [cited at p. 2]

[6] Offshore simulator centre as web page. http://www.offshoresimcentre.no, accessed 27 November 2008. [cited at p. 2]

[7] Real-time workshop. http://www.mathworks.com/products/rtw/. [cited at p. 102]

[8] Ship manoeuvring simulator centre as web page. http://www.smsc.no, accessed 27 November 2008. [cited at p. 2]

[9] K. Brautaset. *Innføring i Oljehydraulikk*. Universitetsforlaget, 1982. [cited at p. 23]

[10] O. Egeland and J. T. Gravdahl. *Modeling and Simulation for Automatic Control*. Marine Cybernetics AS, 2002. [cited at p. 5, 12, 13, 25, 26, 27, 28, 51]

[11] O. M. Faltinsen. *Sea loads on ships and soffshore structures*. Cambridge University Press, 1990. [cited at p. 37]

[12] T. I. Fossen. *Marine Control Systems*. Marine Cybernetics AS, 2002. [cited at p. 13, 15, 16]

[13] A. Hammen Hægeland and S. Hana. Modeling and control of rov deployment system. Technical report, NTNU, December 2007. Project work. [cited at p. 41, 42]

[14] IMCA. *Crane Specification Document*, jul 2003. [cited at p. 51]

[15] Tor Arne Johansen. Personal communication. Dec 2008. [cited at p. 1, 2]

[16] V. Johansen. *Modelling of Flexible Slender Systems for Real-Time Simulation and Control Applications*. PhD thesis, NTNU, December 2007. [cited at p. 3]

[17] A. Kjølle. *Oljehydraulikk*. Tapir, 2 edition, 1995. [cited at p. 23, 24, 31]

[18] N. D. Manring. *Hydraulic Control Systems*. Wiley, 2005. [cited at p. 23, 24, 25, 51]

[19] Olve Mo. Personal communication. Nov 2008. [cited at p. 52, 57, 58]

[20] F. G. Nielsen. *Lecture notes in Marine Operations*. Department of Marine Hydrodynamics, NTNU, January 2007. [cited at p. 1, 61]

[21] Egeland O. *Servoteknikk*. Tapir, 1993. [cited at p. 56]

[22] Scanrope. Wire ropes. Technical report, Scanrope, n. d. [cited at p. 48]

[23] L. Sciavicco and B. Siciliano. *Modelling and Control of Robot Manipulators*. Springer, 2000. [cited at p. 5, 6, 8, 9, 10, 11]

[24] Mv siem tbn 323 & 326. http://www.siemoffshore.com. Accessed 16 December 2008. Specification sheet for the MV Siem TBN 323 & 326 vessels. [cited at p. 6, 18]

[25] B. Skaare. *Control of Loads Through the Wave Zone in Marine Operations*. PhD thesis, Department of Engineering Cybernetics, NTNU, September 2004. [cited at p. 3, 40, 41]

[26] Egeland O. Skaare B. Parallel force/position crane control in marine operations. *IEEE Journal of Oceanic Engineering*, 2006. [cited at p. 63]

[27] J. Sverdrup-Thygeson. Modeling and simulation of an active hydraulic heave compensation system for offshore cranes. Master's thesis, NTNU, June 2007. [cited at p. 1, 3, 61]

[28] G. Tomasgard. Modelling and simulation of offshore lifting operations. Technical report, NTNU, May 2008. Project work. [cited at p. 3, 37, 38, 39, 40, 43, 44, 45, 65, 75]

[29] Det Norske Veritas. Rules for planning and execution of marine operations. Technical report, Det Norske Veritas, 1996. [cited at p. 46]

[30] J.-E. Wagnild. Modeling and simulation of offshore cranes. Technical report, NTNU, December 2007. Project work. [cited at p. 2, 5, 23, 25, 26, 27, 28, 29, 32, 115]

[31] J.-E. Wagnild. Modeling and simulation of hydraulic winch systems for offshore cranes. Master's thesis, NTNU, June 2008. [cited at p. 2, 23, 51, 54]

Appendices

Appendix A

Estimate link mass and inertia

A.1 Mass and inertia of cylindrical structure elements

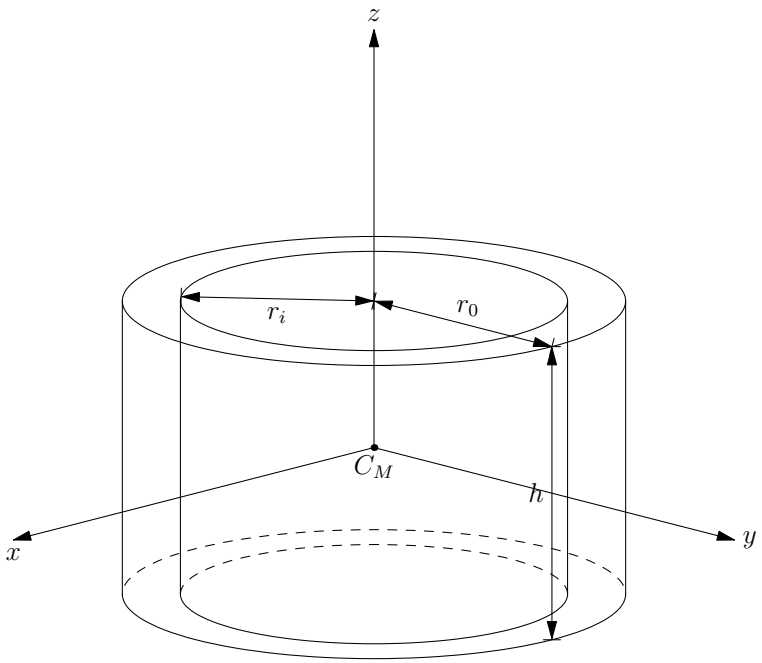

Figure A.1: Cylindrical annulus.

The mass of the cylindrical king is determined from its material volume and the material density ρ by

$$m = \rho\pi(r_o^2 - r_i^2)h, \tag{A.1}$$

where $\rho = 7800\ \mathrm{kg/m^3}$ is the density of the material, i.e. the density of steel, r_o and r_i are outer and inner king radius, respectively, and h is cylinder height.

By linearity, the inertia is found by calculating the difference of the inertia for two solid cylinders of radius r_o and r_i with masses

$$m_0 = \rho\pi r_o^2 h, \text{ and} \tag{A.2}$$
$$m_i = \rho\pi r_i^2 h \tag{A.3}$$

respectively. The inertia for a solid cylinder about the z-axis is given by

$$I_z = \frac{1}{2}mr^2 \tag{A.4}$$

Hence, the inertia for a cylindrical annulus about the z-axis is

$$I_z = \frac{1}{2}m_0 r_0^2 - \frac{1}{2}m_i r_i^2 \tag{A.5}$$
$$= \frac{1}{2}(m_0 r_0^2 - m_i r_i^2) \tag{A.6}$$
$$= \frac{1}{2}(\rho\pi r_o^4 h - \rho\pi r_i^4 h) \tag{A.7}$$
$$= \frac{\rho\pi h}{2}(r_o^4 - r_i^4) \tag{A.8}$$

The moment of inertia may be expressed by the mass from Equation (A.1) as

$$I_z = \frac{1}{2}m(r_o^2 + r_i^2), \tag{A.9}$$

where the relation

$$(r_o^4 - r_i^4) = (r_o^2 - r_i^2)(r_o^2 + r_i^2) \tag{A.10}$$

is used.

The moment of inertia about the x and y axes are found accordingly by the formula

$$I_x = I_y = \frac{1}{12}m(3r^2 + h^2), \tag{A.11}$$

i.e.

$$I_x = I_y = \frac{1}{12}m_o(3r_o^2 + h^2) - \frac{1}{12}m_i(3r_i^2 + h^2) \tag{A.12}$$
$$= \frac{1}{4}(m_o r_o^2 - m_i r_o^2) + \frac{1}{12}(m_o - m_i)h^2 \tag{A.13}$$
$$= \frac{1}{4}m(r_o^2 + r_i^2) + \frac{1}{12}mh^2 \tag{A.14}$$

where m is given by Equation (A.1). The resulting inertia tensor is

$$\mathbf{I} = \begin{bmatrix} I_x & 0 & 0 \\ 0 & I_y & 0 \\ 0 & 0 & I_z \end{bmatrix} \tag{A.15}$$

where the offdiagonal elements are zero due to symmetry.

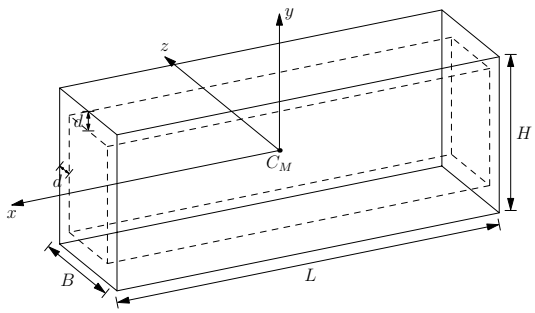

Figure A.2: Box inertia.

A.2 Mass and inertia of box shaped structure elements

The mass and inertia of box boom links are estimated by assuming homogenous hollow box booms with length L, breadth B, height H, the steel plate thickness d as shown in Figure A.1 and steel density ρ as in Section A.1. Then the mass is given by

$$m = \rho(BH - (B-2d)(H-2d))L = 2\rho(B+H-2d)dL \tag{A.16}$$

By linearity, the moment of inertia for a hollow box is found by calculating the moment of inertia for a solid box and subtracting the moment of inertia for the hollow part. From Figure A.2 we see that the outer solid box has mass

$$m_o = \rho BHL, \tag{A.17}$$

and the inner solid box has the mass

$$m_i = \rho L(B-2d)(H-2d) \tag{A.18}$$

Note that $m = m_o - m_i$.

The moment of inertia for a solid box about the z-axis is given by

$$I_z = \frac{1}{12}m(L^2+H^2) \tag{A.19}$$

The moment of inertia about the z-axis for a hollow box is thus given by

$$\begin{aligned} I_z &= \frac{1}{12}m_o(L^2+H^2) - \frac{1}{12}m_i(L^2+(H-2d)^2) && \text{(A.20)}\\ &= \frac{1}{12}(L^2(m_o-m_i) + (m_oH^2 - m_i(H-2d)^2)) && \text{(A.21)}\\ &= \frac{1}{12}(L^2+H^2)(m_o-m_i) + \frac{1}{3}m_id(H-d) && \text{(A.22)}\\ &= \frac{1}{12}(L^2+H^2)m + \frac{1}{3}m_id(H-d) && \text{(A.23)} \end{aligned}$$

Accordingly, the moment of inertia for the hollow box about the x-axis is

$$\begin{aligned} I_x &= \frac{1}{12}m_o(B^2+H^2) - \frac{1}{12}m_i((B-2d)^2+(H-2d)^2) && \text{(A.24)}\\ &= \frac{1}{12}(B^2+H^2)(m_o-m_i) + \frac{1}{3}m_id(B+H-2d) && \text{(A.25)}\\ &= \frac{1}{12}(B^2+H^2)m + \frac{1}{3}m_id(B+H-2d), && \text{(A.26)} \end{aligned}$$

and about the y-axis it is

$$I_y = \frac{1}{12} m_o (B^2 + L^2) - \frac{1}{12} m_i ((B - 2d)^2 + L^2) \tag{A.27}$$

$$= \frac{1}{12} (B^2 + L^2) m + \frac{1}{3} m_i d (B - d) \tag{A.28}$$

The resulting inertia tensor is

$$\mathbf{I} = \begin{bmatrix} I_x & 0 & 0 \\ 0 & I_y & 0 \\ 0 & 0 & I_z \end{bmatrix} \tag{A.29}$$

where the offdiagonal elements are zero due to symmetry.

Appendix B

Viscous damping and leakage coefficients for hydraulic cylinders

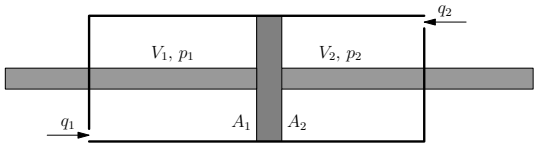

Figure B.1: Symmetric hydraulic cylinder.

The coefficient for viscous friction B_p is found in [30] by assuming that the cylinder is symmetric; see Figure B.1. The model for the symmetric hydraulic cylinder is

$$\frac{V_t}{4\beta}\dot{p}_L = q_L - C_{tm}p_L - A\dot{x}_p \tag{B.1}$$

$$m_t\ddot{x}_p = -B_p\dot{x}_p + Ap_L - F_L, \tag{B.2}$$

where $A = A_2$, $p_L = p_1 - p_2$, $q_L = \frac{1}{2}(q_1 + q_2)$, $C_{tm} = (C_{im} + \frac{1}{2}C_{em})$ and $V_t = Ax_s$ is the total cylinder volume. This model is linear and may be Laplace transformed into

$$s\left[s^2 + \left(\frac{4\beta C_{tm}}{V_t} + \frac{B_p}{m_t}\right)s + \frac{4\beta(B_pC_{tm} + A^2)}{V_tm_t}\right]x_p = \frac{4\beta}{V_tm_t}\left[Aq_L - \left(\frac{V_t}{4\beta}s + C_{tm}\right)F_L\right] \tag{B.3}$$

By setting the leakage $C_{tm} = 0$, the system's natural frequency is given by

$$\omega_n^2 = \frac{4\beta A^2}{V_tm} \quad \Rightarrow \quad \omega_n = 2A\sqrt{\frac{\beta}{m_tV_t}}, \tag{B.4}$$

and the damping is thus given by

$$B_p = 2\zeta m_t\omega_n = 4\zeta A_2\sqrt{\frac{\beta m_t}{A_2x_s}} = 4\zeta\sqrt{\frac{A_2\beta m_t}{x_s}}, \tag{B.5}$$

where $\zeta \in (0.1, 0.5)$ is the relative damping.

The leakage coefficients are found by assuming that the system damping should be fixed when introducing leakage. In order to achieve this the viscous damping factor B_p must be reduced. By introducing a scaling factor $\alpha \in [0, 1]$ in the equation

$$\frac{4\beta C_{tm}}{V_t} + \frac{B_p}{m_t} = 2\zeta\omega_n \tag{B.6}$$

such that

$$\frac{4\beta C_{tm}}{V_t} + \alpha\frac{B_p}{m_t} = \frac{B_p}{m_t}, \tag{B.7}$$

the total leakage coefficient is given by

$$C_{tm} = B_p(1-\alpha)\frac{V_t}{4\beta m_t} \tag{B.8}$$

The internal and external leakage coefficients are now given by

$$C_{tm} = C_{im} + \frac{1}{2}C_{em} \tag{B.9}$$

and

$$C_{em} = 0.1C_{im} \tag{B.10}$$

Appendix C

Simulink diagrams

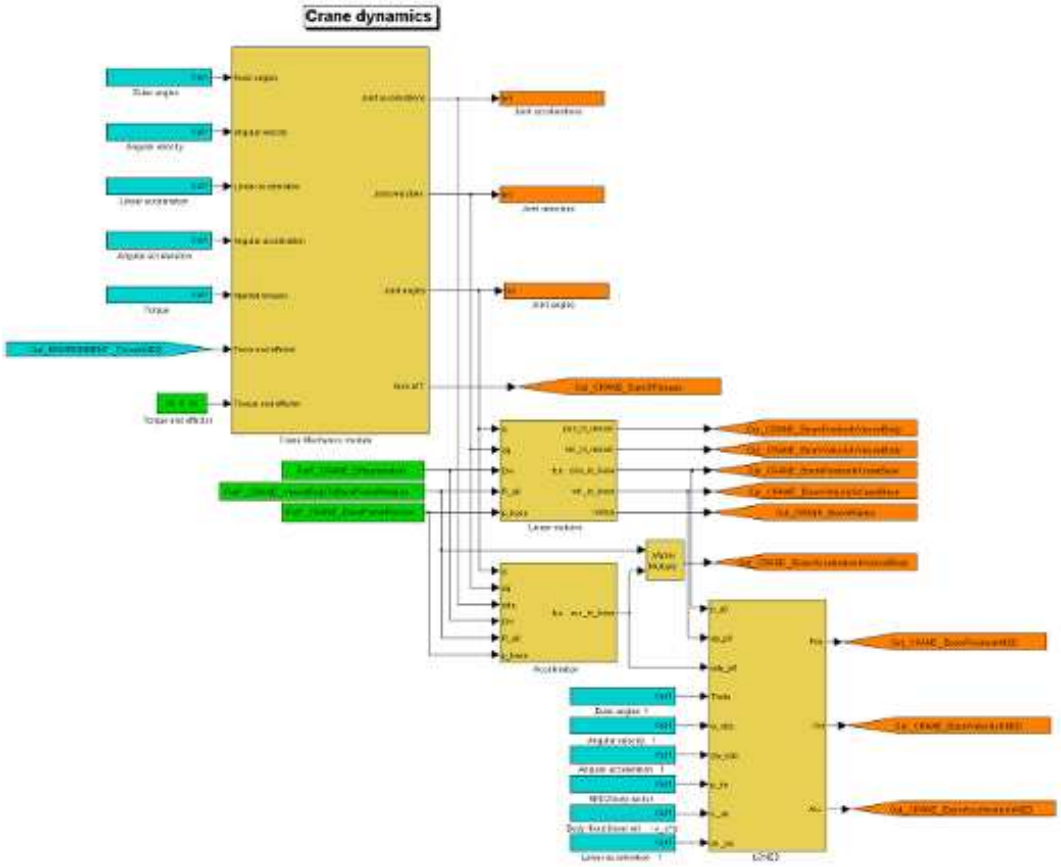

Figure C.1: The crane dynamics model.

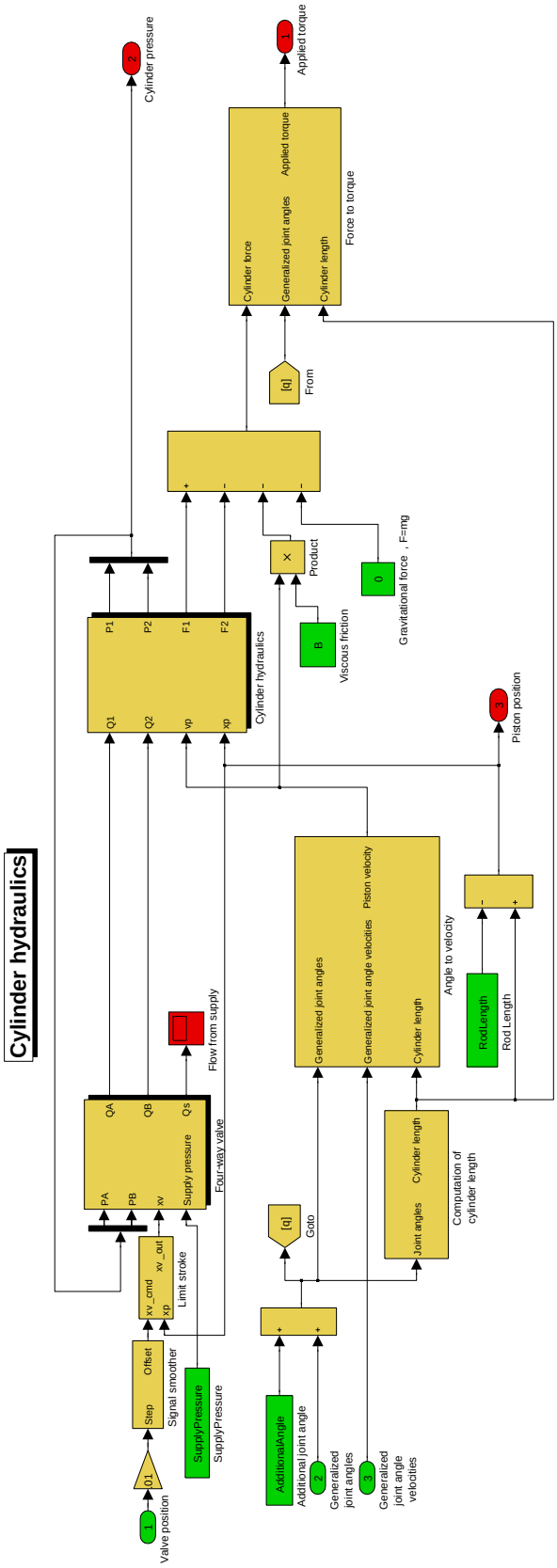

Figure C.2: The hydraulics model.

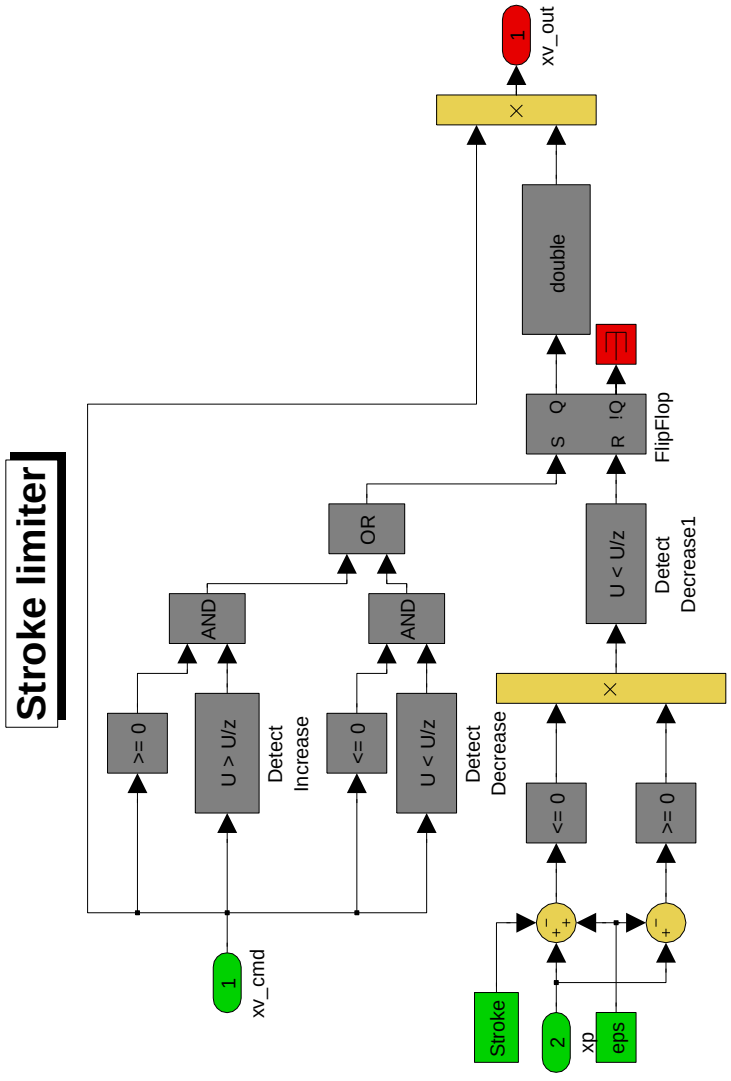

Figure C.3: Logic to limit the piston travel.

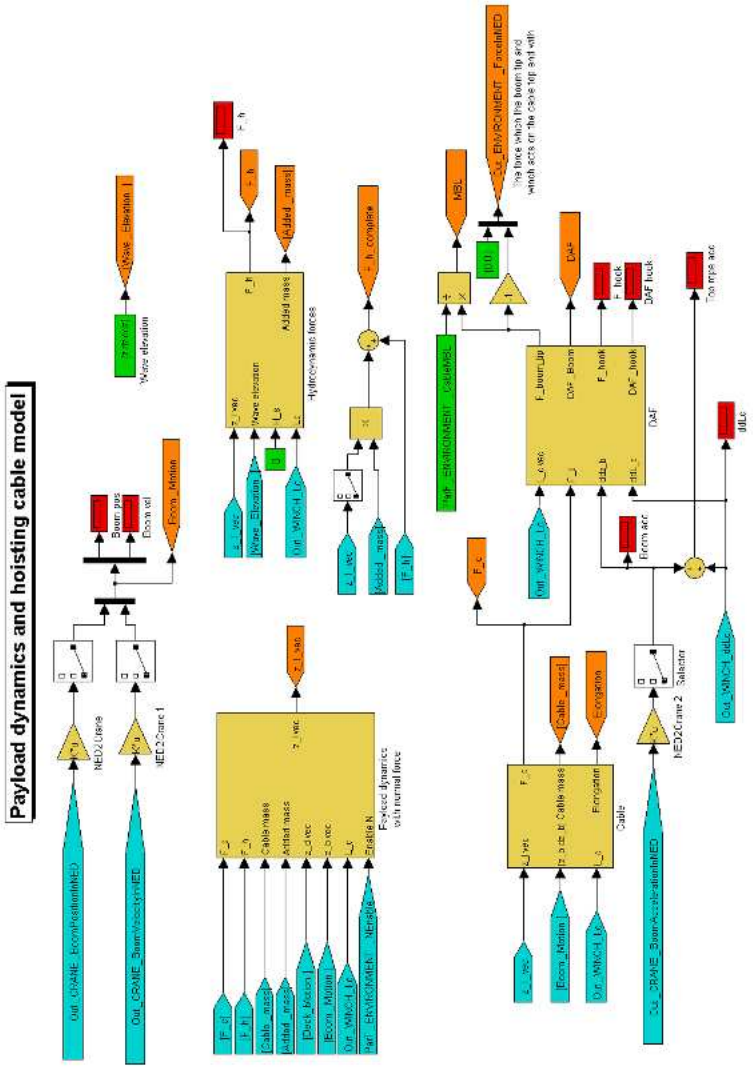

Figure C.4: The payload and hoisting cable model.

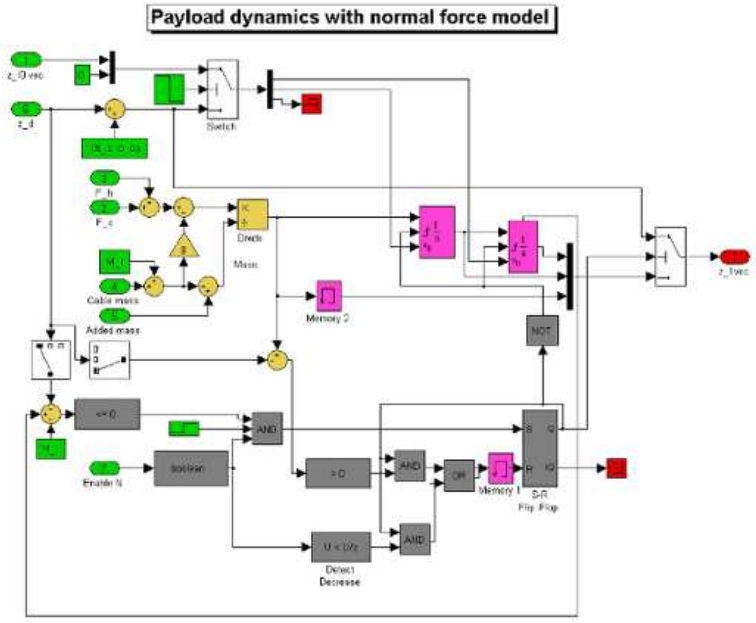

Figure C.5: Payload dynamics model and logic for the normal force model.

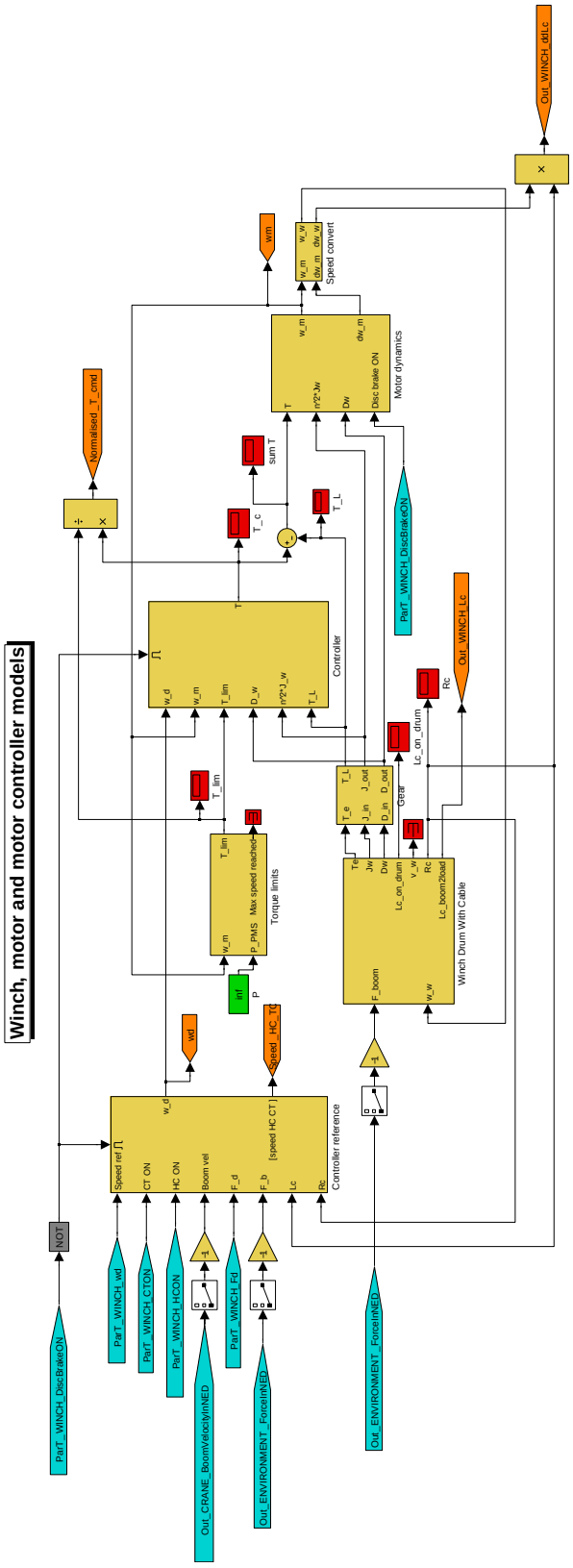

Figure C.6: The winch and drive system with controller.

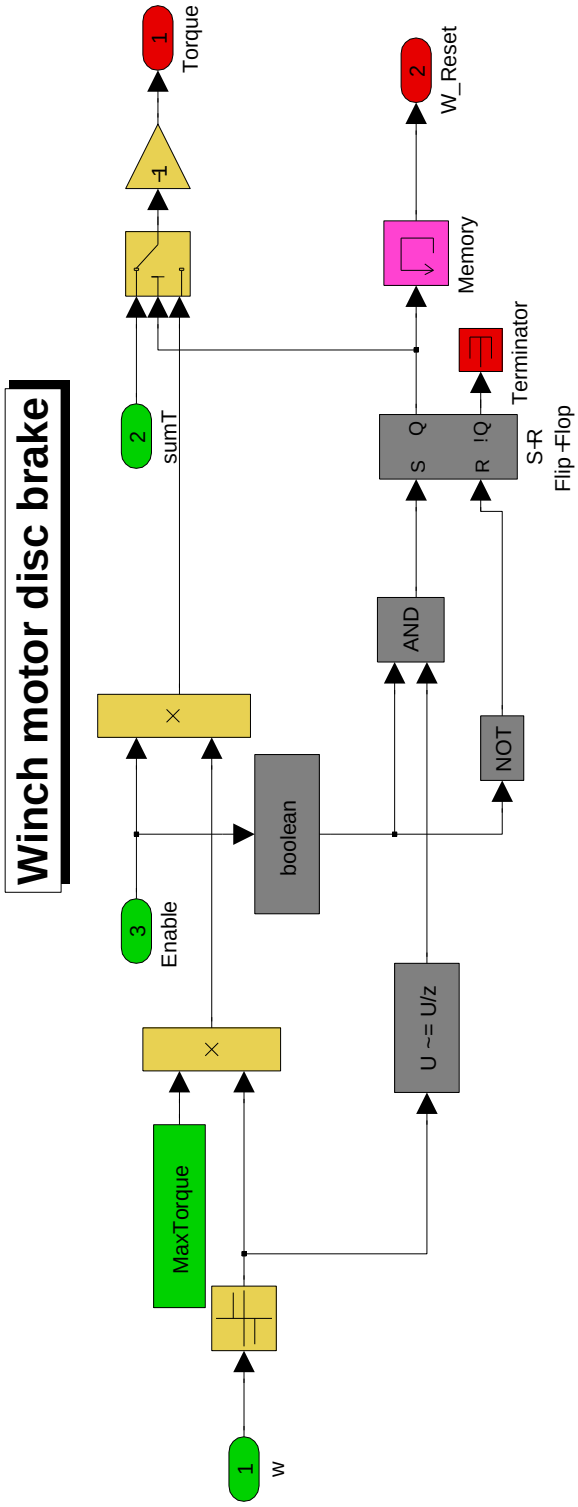

Figure C.7: Disc brake model.

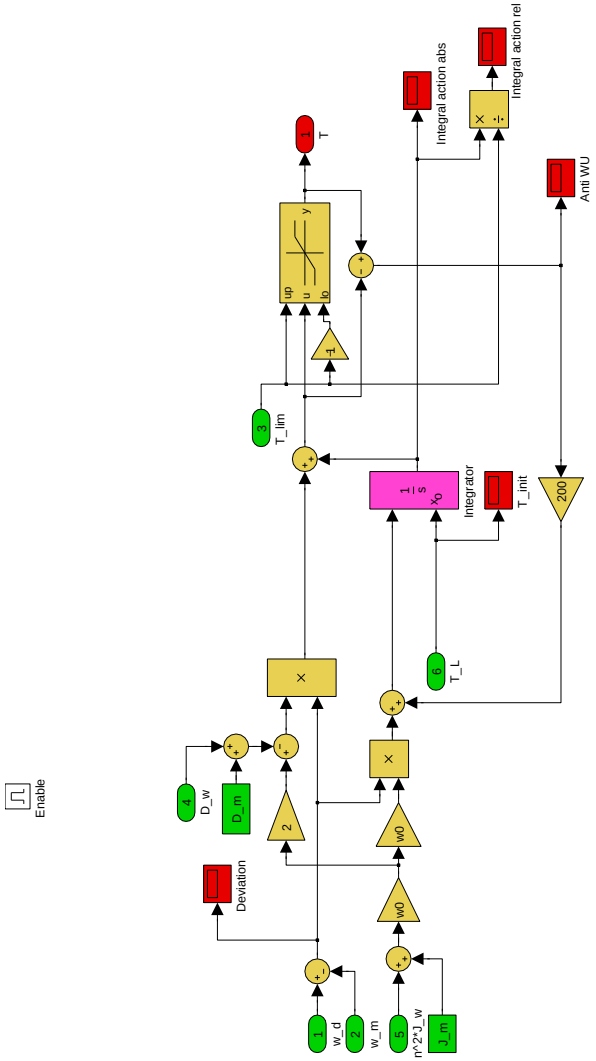

Figure C.8: Disc brake model.